New Jersey Institute of Technology
Digital Commons @ NJIT

Dissertations | Electronic Theses and Dissertations

Spring 5-31-2018

Silicon based uncooled microbolometer

Asahel Banobre
New Jersey Institute of Technology

Follow this and additional works at: https://digitalcommons.njit.edu/dissertations

Part of the Materials Science and Engineering Commons

Recommended Citation
Banobre, Asahel, "Silicon based uncooled microbolometer" (2018). *Dissertations*. 1363.
https://digitalcommons.njit.edu/dissertations/1363

This Dissertation is brought to you for free and open access by the Electronic Theses and Dissertations at Digital Commons @ NJIT. It has been accepted for inclusion in Dissertations by an authorized administrator of Digital Commons @ NJIT. For more information, please contact digitalcommons@njit.edu.

Copyright Warning & Restrictions

The copyright law of the United States (Title 17, United States Code) governs the making of photocopies or other reproductions of copyrighted material.

Under certain conditions specified in the law, libraries and archives are authorized to furnish a photocopy or other reproduction. One of these specified conditions is that the photocopy or reproduction is not to be "used for any purpose other than private study, scholarship, or research." If a, user makes a request for, or later uses, a photocopy or reproduction for purposes in excess of "fair use" that user may be liable for copyright infringement,

This institution reserves the right to refuse to accept a copying order if, in its judgment, fulfillment of the order would involve violation of copyright law.

Please Note: The author retains the copyright while the New Jersey Institute of Technology reserves the right to distribute this thesis or dissertation

Printing note: If you do not wish to print this page, then select "Pages from: first page # to: last page #" on the print dialog screen

NJIT
New Jersey's Science &
Technology University

The Van Houten library has removed some of the personal information and all signatures from the approval page and biographical sketches of theses and dissertations in order to protect the identity of NJIT graduates and faculty.

ABSTRACT

SILICON BASED UNCOOLED MICROBOLOMETER

by
Asahel Bañobre

During the last decade, uncooled microbolometer infrared detectors have attracted the attention of military and civilian infrared detection and imaging industry due to their significant advantages. In actuality, infrared imaging systems play a critical role in sectors such as thermography (predictive maintenance and building inspection), commercial and civilian applications (vision automotive, surveillance, navigation and fire-fighting), and defense industry (thermal weapon sight, soldier vision and vehicle vision enhancer). Compared with the cryogenically cooled infrared photon detectors, uncooled infrared imaging technology offers advantages such as operation at room temperature, light weight and size, reduced power consumption, easy integration with read-out electronics and broadband response capability.

The motivation for this study is the consideration of silicon as an alternative candidate to replace the standard infrared detector thermosensing materials, as a result of its low cost and easy integration with the actual silicon planar lithography microfabrication techniques. No prior attempts are known in the literature on the use of low doped p-type silicon (p-Si) as a thermosensing material in thermal infrared detectors.

The main aim of this research work is the design, modeling and simulation of low doped p-Si based uncooled microbolometer infrared detector. The theoretical optical modeling, and electronic performance are analyzed and

explained. Radiative properties, as function of thin film thickness, of some commonly used thin films of dielectric materials, aluminum oxide (Al_2O_3), silicon dioxide (SiO_2), aluminum nitride (AlN) and silicon nitride (Si_3N_4) are investigated within the infrared spectral range of 1.5-14.2 μm.

A novel thermally isolated, suspended square-shaped multilayer structure microbolometer is proposed. Its radiative properties are simulated and optimized in the long wavelength spectral range of 8-14 μm (transmission window at room temperature). The performance of the proposed microbolometer structure is numerically calculated by the figures of merit that characterize the thermal detector response. The dimensions of the microbolometer structure are optimized in order to achieve the maximum responsivity and low thermal time response required by the imaging systems, while securing the stability and support of the structure.

SILICON BASED UNCOOLED MICROBOLOMETER

by
Asahel Bañobre

A Dissertation
Submitted to the Faculty of
New Jersey Institute of Technology
in Partial Fulfillment of the Requirements for the Degree of
Doctor of Philosophy in Materials Science and Engineering

Interdisciplinary Program in Materials Science and Engineering

May 2018

Copyright © 2018 by Asahel Bañobre

ALL RIGHTS RESERVED

APPROVAL PAGE

SILICON BASED UNCOOLED MICROBOLOMETER

Asahel Bañobre

Dr. N. M. Ravindra, Dissertation Advisor — Date
Professor of Physics, NJIT

Dr. Sagnik Basuray, Committee Member — Date
Assistant Professor of Chemical and Materials Engineering, NJIT

Dr. Eon Soo Lee, Committee Member — Date
Assistant Professor of Mechanical and Industrial Engineering, NJIT

Dr. Michael Jaffe, Committee Member — Date
Research Professor of Biomedical Engineering, NJIT

Dr. Anthony Fiory, Committee Member — Date
AT&T Bell Labs (Retired), NJIT

Dr. Jacob Trevino — Date
Principal Scientist, DrinkSavvy Inc.

BIOGRAPHICAL SKETCH

Author: Asahel Bañobre

Degree: Doctor of Philosophy

Date: May 2018

Undergraduate and Graduate Education:

- Doctor of Philosophy in Materials Science and Engineering, New Jersey Institute of Technology, Newark, NJ, 2018

- Master of Science in Applied Physics, New Jersey Institute of Technology, Newark, NJ, 2006

- Bachelor of Science in Applied Physics, New Jersey Institute of Technology, Newark, NJ, 2002

Major: Materials Science and Engineering

Presentations, Publications and Patents:

A. Bañobre, et al., (2018). Radiative Properties of Thin Films of Common Dielectric Materials in IR Spectral Range of 1.5-14.2 μm - Application to Infrared Imaging, *JOM – The Journal of the Minerals, Metals & Materials Society (TMS)*, Advanced Real Time Optical Imaging, doi.org/10.1007/s11837-018-2883-3.

A. Bañobre, et al., (2018). Thermal Detector and Associated Fabrication Processes, Provisional Patent Application, USPTO, U.S. Application No. 62/649,872.

A. Bañobre, et al., (2018). 3-D Printed Magnetic Polymers, Recent Developments in Biological, Structural and Functional Thin Films & Coatings – Biomedical & Polymeric Applications, The Minerals, Metals & Materials Society (TMS) Annual Meeting & Exhibition, Phoenix, Arizona, March 11-15.

A. Bañobre, et al., (2018). Formation & Characterization of Black Silicon by Reactive Ion Etching, Recent Developments in Biological, Structural and Functional Thin Films & Coatings – Functional Coatings for Green Technology and Sustainability, The Minerals, Metals & Materials Society (TMS) Annual Meeting & Exhibition, Phoenix, Arizona, March 11-15.

A. Bañobre, et al., (2017). P-silicon Based Microbolometer, Mid-Atlantic Section - American Physical Society (MAS-APS), Newark, New Jersey, November 2.

S. R. Marthi, et al., (2017). Influence of Passivation Layers on Black Silicon, Mid-Atlantic Section - American Physical Society (MAS-APS), Newark, New Jersey, November 2.

N. M. Ravindra, et al., Radiative Properties of Semiconductors, San Rafael, California: Morgan & Claypool Publishers (IOP Publishing), ISBN: 978-1-6817-4048-5 (2017).

A. Bañobre, et al., (2017). P-Si Based Microbolometer - Optical Properties, Emerging Multifunctional Materials for Bio, EO, RF and Radiation Sensors III, Materials Science & Technology (MS&T) Annual Meeting & Exhibition, Pittsburgh, Pennsylvania, October 8-12.

S. R. Marthi, et al., (2017). Black Silicon Microbolometer, Emerging Multifunctional Materials for Bio, EO, RF and Radiation Sensors I, Materials Science & Technology (MS&T) Annual Meeting & Exhibition, Pittsburgh, Pennsylvania, October 8-12.

S. R. Marthi, et al., (2017). Black Silicon Based Microbolometer, Recent Developments in Biological, Structural and Functional Thin Films and Coatings - Multiscale Modeling of Thin Films, The Minerals, Metals & Materials Society (TMS) Annual Meeting & Exhibition, San Diego, California, February 26-March 2.

A. Banobre, et al., (2016). p-Silicon Based Microbolometer, Materials Property Understanding through Characterization-Advanced Materials I, Conference Proceedings Materials Science & Technology (MS&T) Annual Meeting & Exhibition, Salt Lake City, Utah, October 23-27.

A. Banobre, et al., (2012). Metal Diaphragm Based Magnetic Field Sensor, Symposium on Recent Developments in Biological, Electronic, Functional and Structural Thin Films and Coatings, The Minerals, Metals & Materials Society (TMS) Annual Meeting & Exhibition, Orlando, Florida, March 11-15.

A. Banobre, et al., (2005). Preliminary Measurements on Human Eyes Using a Non-Invasive Self-Tonometer, Proceedings of the IEEE 31st Annual Northeast Bioengineering Conference, Hoboken, New Jersey, April 2-3.

A. Banobre, et al., (2005). Measurement of Intraocular Pressure in Pig's Eyes Using a New Tonometer Prototype, Proceedings of the IEEE 31st Annual Northeast Bioengineering Conference, Hoboken, New Jersey, April 2-3, 2005.

ACKNOWLEDGEMENTS

I would like to express my sincere gratitude to Dr. N. M. Ravindra for his constant guidance, encouragement and support in my research. I am very grateful for the experience of working with such a great advisor that inspired me with his dedication and work ethics.

I would like to thank my thesis advisory committee: Dr. Jacob Trevino, Dr. Anthony Fiory, Dr. Michael Jaffe, Dr. Sagnik Basuray and Dr. Eon Soo Lee, for accepting to serve as members on my PhD Dissertation committee.

I am very thankful to Ms. Clarisa Gonzalez, Associate Director of Graduate Studies and Dr. Sotirios Ziavras, Vice Provost for Graduate Studies and Dean of the Graduate Faculty in formatting and improving the presentation of this doctoral dissertation thesis.

I would also want to thank to NSF I-Corps, Dr. Michael Ehrlich and Ms. Judith Sheft for their help in providing partial funding for the research.

I would like to express my appreciation to Dr. Jacob Trevino and Dr. Vishal Narang of CUNY Advanced Science Research Center (ASRC) for their time and technical advice. It was a privilege to work with them.

I am especially thankful to my teammates and colleagues, Dr. Sita Rajyalaxmi Marthi and Yan Liu, for their constant support and for their encouragement. Especially, I am grateful to Dr. Sita Rajyalaxmi Marthi, great friend, with whom I had critical discussions about the topic.

I want to thank my grandparents, Ramon and Corealina, and my aunt, Nevia for their love and support during the first years of my life. I would also want to thank my brother, Lenny for encouraging me during the process of completing this work.

Finally, I am grateful to my wife, Noelia, for her patience and support throughout the process of this doctoral dissertation thesis. Thanks to my children: Asael and Ethan, they gave me the motivation to complete this work.

Dedicated to my family:

A mis abuelos, Ramon y Corealina.

My wife, Noelia, and my kids, Asael and Ethan for giving me a purpose.

TABLE OF CONTENTS

Chapter	Page
1. INTRODUCTION …………………………………………………………….……	1
1.1 Infrared Radiation ………………………………………………….…..	1
1.2 Radiometry & Blackbody Radiation ……………………………….….	3
1.3 Optical Imaging System ………………………………………….....	8
1.4 Infrared Radiation Transmission in Earth's Atmosphere ….…….	11
2. OPTICAL DETECTORS ……………………………………………….……	13
2.1 Optical Detection Classifications ………………………………..….	13
2.2 Photon Detectors Versus Thermal Detectors ………………….....	15
2.3 Thermal Infrared Detector ………………………………………....	16
2.3.1 Bolometer - Principle of Operation ………………………..	16
2.3.2 Thermal Detector Heat-balance Equation ……………..….	19
2.3.3 System Noise ……………………………………………..……	27
2.3.4 Figures of Merit ……………………………………………..….	30
2.3.5 Optical Infrared Imaging System ………………………..…….	34
3. MODELING OF RADIATIVE PROPERTIES ……………………….....	36
3.1 Radiation-Matter Interaction ……………………………………..….	36
3.2 Matrix Method (Multi-Rad) ………………………………………..…..	38
4. UNCOOLED MICROBOLOMETER ……………………………….…...	44
4.1 Background ……………………………………………………………..….	44
4.2 Microbolometer - Materials Selection ……………..……………..….	47

TABLE OF CONTENTS
(Continued)

Chapter **Page**

4.2.1 P-silicon as Thermosensing Material …………………..… 48

4.2.2 Radiative Properties of Thin Films of Common Dielectric Materials …………………………………………….... 52

4.2.3 Dielectric Materials as Infrared Filters ……….……….... 58

4.2.4 Silicon Nitride as IR Radiation Absorber ………………... 59

4.2.5 Microbolometer - Electrical Interconnection and IR Reflective Layer …………………………………………. 60

4.2.6 Optical Constants of Microbolometer Materials …..…..... 60

4.3 Microbolometer Structural Design ..…………………….…... 64

4.4 Optimization of Microbolometer Radiative Properties ..…..….. 68

4.5 Numerical Calculations of Microbolometer ………………….... 80

4.5.1 Figures of Merit …………………………………….…. 85

4.5.2 $NETD$ of Microbolometer ………………………….… 88

4.6 Numerical Calculations of Improved Microbolometer ………… 90

4.6.1 Figures of Merit of Improved Microbolometer …………... 92

4.6.2 $NETD$ of Improved Microbolometer ……………..…….. 94

4.6.3 Summary ……………………………………………..… 96

5. MICROBOLOMETER FABRICATION PROCESS ……...………… 98

5.1 Method of Microbolometer Fabrication …………………….... 98

6 CONCLUSIONS AND FUTURE WORK ……………….……..….. 105

TABLE OF CONTENTS
(Continued)

Chapter **Page**

6.1 Conclusions ……………………………………………………….… 105

6.2 Future Work …………………………………………………….... 107

REFERENCES ……………………………………………………….….. 109

LIST OF TABLES

Table		Page
4.1	Total Value of Radiative Properties of Al_2O_3 (spectral range: 1.5-14.2 μm) ……………………………………………………………	57
4.2	Total Value of Radiative Properties of SiO_2 (spectral range: 1.5-14.2 μm) ……………………………………………………………	57
4.3	Total Value of Radiative Properties of AlN (spectral range: 1.5-14.2 μm) ……………………………………………………………	58
4.4	Total Value of Radiative Properties of Si_3N_4 (spectral range: 1.5-14.2 μm) ……………………………………………………………	58
4.5	Band-pass Range and Transmittance for Various Dielectric Materials Considered as IR Filters (spectral range: 1.5-14.2 μm; 30 ˚C) ……………………………………………………………	59
4.6	Optical Properties of the Proposed Two-Level Multilayer Structure (Reflectance and absorptance total values) …………………………	75
4.7	Enhancement of Absorptance with Cavity/Au Reflectance Layer....	78
4.8	Physical and Thermal Properties of Materials Used in the Proposed Microbolometer ……………………………………………………	83
4.9	Parameters of Proposed Microbolometer ……………………………..	85
4.10	Parameters of Modified Proposed Microbolometer …………………	92

LIST OF FIGURES

Figure		Page
1.1	The electromagnetic spectrum …………………………………….……..……	2
1.2	Spectral radiance vs. wavelength for blackbody temperatures from 300 K to 1000 K …..…………………………………...………..……	4
1.3	Total radiant exitance from a blackbody at 300 K is the area under the spectral exitance curve ………………………………………....	6
1.4	Optical detection imaging system ……………………….…….….…..	9
1.5	Infrared radiation transmission in earth's atmosphere, over 6000 ft horizontal path at sea level, containing 17 mm of precipitate water	11
2.1	Schematic block diagram of a thermal detector …………….………..	17
2.2	Schematic diagram of a thermal detector operation ……….………..	18
2.3	Schematic of electrical biasing circuit for bolometer ….………….....	19
2.4	Schematic diagram of optical system ………….………….….…..……	35
3.1	Notation of matrix method of multilayers ……..…………..……….….	40
4.1	Energy bands in a p-type extrinsic semiconductor …………….….	49
4.2	Carrier transport of p-type extrinsic semiconductor ………….……..	50
4.3	TCR as a function of electrical resistivity for n-type and p-type silicon (23 ºC) …….……………………….……...………….....	51
4.4	Absorptance, transmittance and reflectance for varying thicknesses of (a) Al_2O_3 and (b) SiO_2, at room temperature (30 ºC)	55
4.5	Absorptance, transmittance and reflectance for varying thicknesses of (a) AlN and (b) Si_3N_4, at room temperature ……….	56
4.6	Optical constants (n and k) of silicon ……………………….………	61
4.7	Optical constants (n and k) of silicon nitride ……………….……..	62
4.8	Optical constants (n and k) of aluminum ………………..…….....	63

LIST OF FIGURES
(Continued)

Figure **Page**

4.9 Optical constants (n and k) of gold …………………………………… 63

4.10 Total reflectance of aluminum and gold ……………………………….…….. 64

4.11 Schematic of the proposed microbolometer (Two-level 50 x 50 μm^2) ……………………………………………………………………… 68

4.12 Cross-sectional schematic of proposed microbolometer multilayer structure (cross view) ………………………………………………….. 69

4.13 Simulated total reflectance, transmittance and absorptance as function of variable Si_3N_4 thickness for the top layer (free standing) of the proposed microbolometer structure (p-Si thickness=0.097 μm) ……………………………………………………………….... 72

4.14 Simulated total reflectance, transmittance and absorptance as function of variable Si_3N_4 thickness for the top layer (free standing) of the proposed microbolometer structure (p-Si thickness=0.145 μm) ……………………………………………………………….……… 72

4.15 Simulated total reflectance, transmittance and absorptance as function of variable Si_3N_4 thickness for the top layer (free standing) of the proposed microbolometer structure (p-Si thickness=0.290 μm) ……………………………………………………………….…... 73

4.16 Simulated total reflectance and absorptance as function of cavity thickness for the proposed microbolometer structure (two-level structure) (p-Si thickness=0.097 μm) ……………………………….. 74

4.17 Simulated total reflectance and absorptance as function of cavity thickness for the proposed microbolometer structure (two-level structure) (p-Si thickness=0.145 μm ……………………………….... 74

4.18 Simulated total reflectance and absorptance as function of cavity thickness for the proposed microbolometer structure (two-level structure) (p-Si thickness=0.290 μm) ……………………………..…. 75

4.19 Evolution of simulated optical spectral of the proposed two-level multilayer with/without cavity-Au layer (p-Si thickness 0.097 μm) ... 76

LIST OF FIGURES
(Continued)

Figure **Page**

4.20 Evolution of simulated optical spectral of the proposed two-level multilayer with/without cavity-Au layer (p-Si thickness 0.145 μm) ... 77

4.21 Evolution of simulated optical spectral of the proposed two-level multilayer with/without cavity-Au layer (p-Si thickness 0.290 μm)… 77

4.22 Simulated optical spectra of Si_3N_4/p-Si/Si_3N_4/Vacuum/Au/SiO_2/Si (p-Si thickness 0.097 μm) ……………………………………..………... 79

4.23 Simulated optical spectra of Si_3N_4/p-Si/Si_3N_4/Vacuum/Au/SiO_2/Si (p-Si thickness 0.145 μm) …………………………………………….…... 79

4.24 Simulated optical spectra of Si_3N_4/p-Si/Si_3N_4/Vacuum/Au/SiO_2/Si (p-Si thickness 0.290 μm) ……………………………...……….…. 80

4.25 Top-view schematic of the proposed microbolometer multilayer structure (interconnection Ohmic contact) …………………………... 83

4.26 Calculated R_v as function of applied bias voltage and modulation frequency ω of IR source (p-Si thickness 0.290 μm) ……………..… 86

4.27 Calculated NEP as function of applied bias voltage and modulation frequency ω of IR source (p-Si thickness 0.290 μm) ……………….. 87

4.28 Calculated D^* as function of applied bias voltage and modulation frequency ω of IR source (p-Si thickness 0.290 μm) ……………… 87

4.29 Calculated $NETD$ as function of applied bias voltage and modulation frequency ω of IR source at $f/_{\#}$=1 (p-Si thickness 0.290 μm) ……………………………………………………………….. 89

4.30 Calculated $NETD$ as function of applied bias voltage and modulation frequency ω of IR source at $f/_{\#}$=2 (p-Si thickness 0.290 μm) ……………………………………………………..……….. 89

4.31 Calculated $NETD$ as function of applied bias voltage and modulation frequency ω of IR source at $f/_{\#}$=3 (p-Si thickness 0.290 μm) ……………………………………………………………..... 90

LIST OF FIGURES
(Continued)

Figure **Page**

4.32 Schematic of improved proposed microbolometer (Two-level 50 x 50 μm^2) 91

4.33 Calculated R_v as function of applied bias voltage and modulation frequency ω of IR source (p-Si thickness= 0.290 μm) 93

4.34 Calculated NEP as function of applied bias voltage and modulation frequency ω of IR source (p-Si thickness= 0.290 μm) 93

4.35 Calculated D^* as function of applied bias voltage and modulation frequency ω of IR source (p-Si thickness= 0.290 μm) 94

4.36 Calculated $NETD$ as function of applied bias voltage and modulation frequency ω of IR source at $f/_{\#}$=1 (p-Si thickness 0.290 μm) 95

4.37 Calculated $NETD$ as function of applied bias voltage and modulation frequency ω of IR source at $f/_{\#}$=2 (p-Si thickness 0.290 μm) 95

4.38 Calculated $NETD$ as function of applied bias voltage and modulation frequency ω of IR source at $f/_{\#}$=3 (p-Si thickness 0.290 μm) 96

5.1 Fabrication process flow of two-level microbolometer (cross-section view). (Continued).................... 102

CHAPTER 1

INTRODUCTION

1.1 Infrared Radiation

In 1800, Sir William Hershel discovered infrared radiation and wrote "…There are rays coming from the sun…invested with a high power of heating bodies, but with none of illuminating objects… [1]." This portion of the electromagnetic spectrum attracted the attention of physicists during the second half of the nineteenth century, and experimental and theoretical approaches were developed in efforts to explain the energy distribution of what Hershel called "invisible rays." In the study of thermal radiation, the work of scientists such as Kirchhoff, Boltzmann, Wien, Rayleigh and Planck led to the introduction of the term blackbody and the evolution of the application of the laws of classical physics and quantum physics [1].

The electromagnetic spectrum is the arrangement of all known frequencies and their relation to wavelengths of the known electromagnetic radiations. The electromagnetic radiation ranges are grouped depending on the nature of the source (heat, radio waves, sunlight and X rays) and are transmitted in the form of waves (electromagnetic waves) or particles (photons). The optical laws of reflection, refraction, interference, polarization and refractions are the same for all the electromagnetic radiation [1]. Electromagnetic waves are described by physical properties such as: frequency ν (Hz), wavelength λ (m), and photon energy E_{ph} (J). The photon energy is expressed as,

$$E_{ph} = h\nu = \frac{hc}{\lambda} \tag{1.1}$$

where, h (6.626 x 10^{-34} Js) is Planck's constant, ν is the frequency (Hz), λ is the wavelength (m) and c (2.998 x 10^{8} ms^{-1}) is the speed of light in vacuum [2].

At temperatures above absolute zero (-273 ºC), the molecules and atoms oscillate, and will radiate electromagnetic waves; this radiation is referred as thermal radiation [3]. Thermal energy can be transferred by conduction and convection in the presence of a material medium; and by radiation without the presence of any medium. The thermal radiation emitted by an object is called infrared radiation (IR) and depends of its surface conditions and temperature [4].

The electromagnetic infrared region extends from 0.75 µm to 1000 µm, and is classified in four regions: 0.75-3 µm (near IR), 3-6 µm (intermediate IR), 6-15 µm (far IR), and 15-1000 µm (extreme IR). The infrared spectral range is depicted in detail in Figure 1.1.

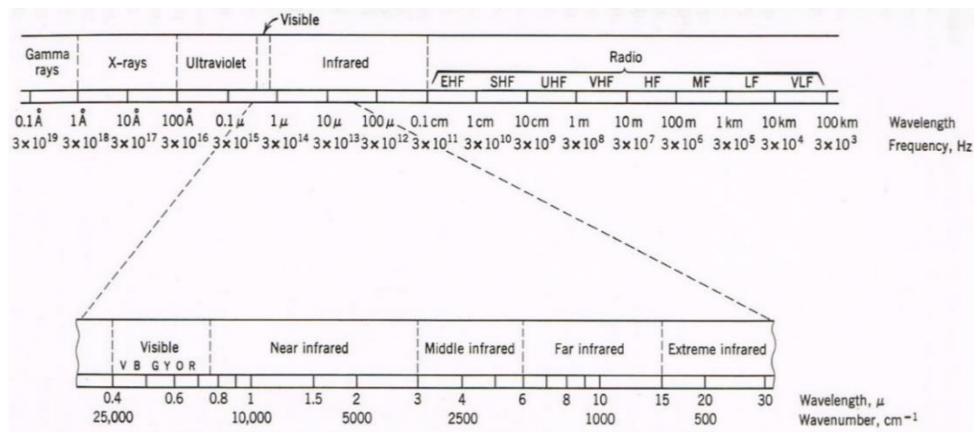

Figure 1.1 The electromagnetic spectrum.
Source: [1].

1.2 Radiometry & Blackbody Radiation

Radiometry is the branch of optical physics that focuses on the study of the electromagnetic spectrum covering from the ultraviolet region to the infrared region. Radiometric measurements characterize and quantify the spectral parameters of the optical radiation sources and the distribution of their emitted optical radiation.

Optical radiant emission is investigated in terms of the ideal concept of a blackbody model. A blackbody is a hypothetical body that absorbs and emits all possible incident electromagnetic radiation, regardless of frequency or angle of incidence, while it is in thermal equilibrium [5]. A blackbody, in thermal equilibrium, emits an electromagnetic radiation spectrum that is determined by its temperature and not by its body composition or its shape [6].

Planck's law considers that the energy is quantized at the atomic level and describes the radiant properties of a blackbody in a continuum of wavelength, as a function of wavelength and source temperature [7], and is expressed as,

$$L_{e,\lambda}(\lambda, T) = \frac{2\,h\,c^2}{\lambda^5\left(e^{\frac{hc}{\lambda k_B T}} - 1\right)} \qquad (1.2)$$

where, $L_{e,\lambda}$ ($Wcm^{-2}\mu m^{-1}sr^{-1}$) is the spectral radiance emittance, h (6.626×10^{-34} Js) is the Planck's constant, c (2.998×10^{8} ms^{-1}) is the speed of light in vacuum, λ is the wavelength (m), k_B (1.38×10^{-23} JK^{-1}) is the Boltzmann's constant, and T (K) is the absolute temperature of the optical source. The infrared spectral radiance

emittance distribution of a blackbody $L_{e,\lambda}$, in the temperature range of 300-1000 K [7], is plotted in Figure 1.2.

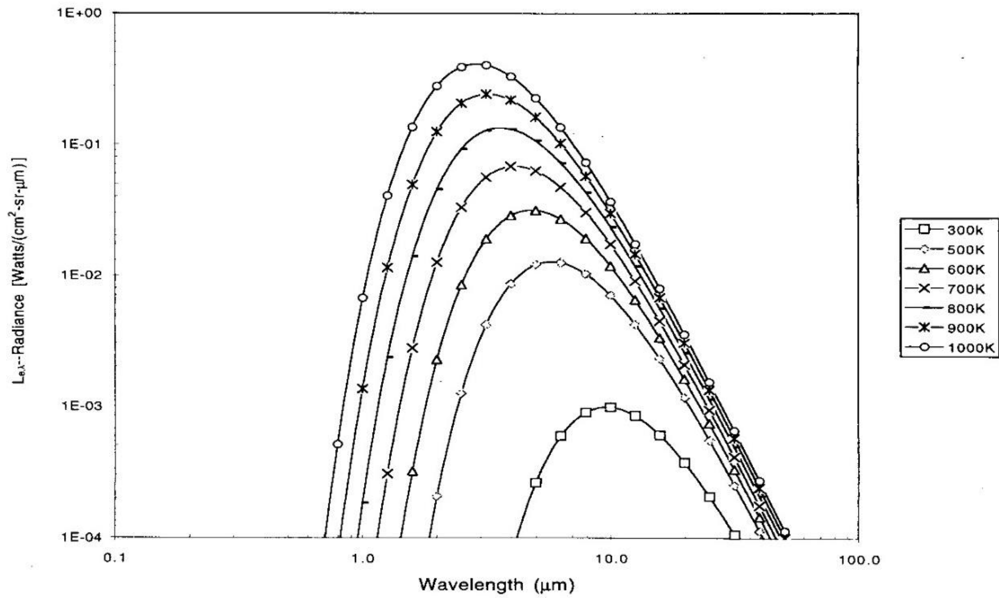

Figure 1.2 Spectral radiance vs. wavelength for blackbody temperatures from 300 K to 1000 K.
Source: [7].

A blackbody source is considered to be a perfect Lambertian radiator, in which the radiance is the same in all directions independent of view angle. The relationship between the spectral radiance emittance and the radiant exitance $M_{e,\lambda}$ ($Wcm^{-2}\mu m^{-1}$) for a planar Lambertian source can be written as,

$$M_{e,\lambda}(\lambda, T) = \pi L_{e,\lambda} \tag{1.3}$$

The total spectral radiance emittance L_e ($Wcm^{-2}sr^{-1}$) and the total spectral radiant exitance M_e (Wcm^{-2}) of an optical source, at a specific temperature, is

integrated over a finite spectral range [7], and is expressed by Equations 1.4 and 1.5.

$$L_e = \int_{\lambda 1}^{\lambda 2} L_{e,\lambda}(\lambda, T)\, d\lambda \tag{1.4}$$

$$M_e = \int_{\lambda 1}^{\lambda 2} M_{e,\lambda}(\lambda, T)\, d\lambda = \pi L_e \tag{1.5}$$

In Equation 1.5, integration is performed over all wavelengths (λ_1=0 to λ_2=∞) and can be modified as in Equation 1.6, and is called as Stefan-Boltzmann law. It states that the relationship between the total radiant exitance and the temperature of the blackbody is as shown in Figure 1.3, where σ (5.67 x 10^{-12} $Wcm^{-2}K^{-4}$) is called the Stefan-Boltzmann constant [7],

$$M_e(T) = \int_{0}^{\infty} M_{e,\lambda}(\lambda, T)\, d\lambda = \sigma T^4 \tag{1.6}$$

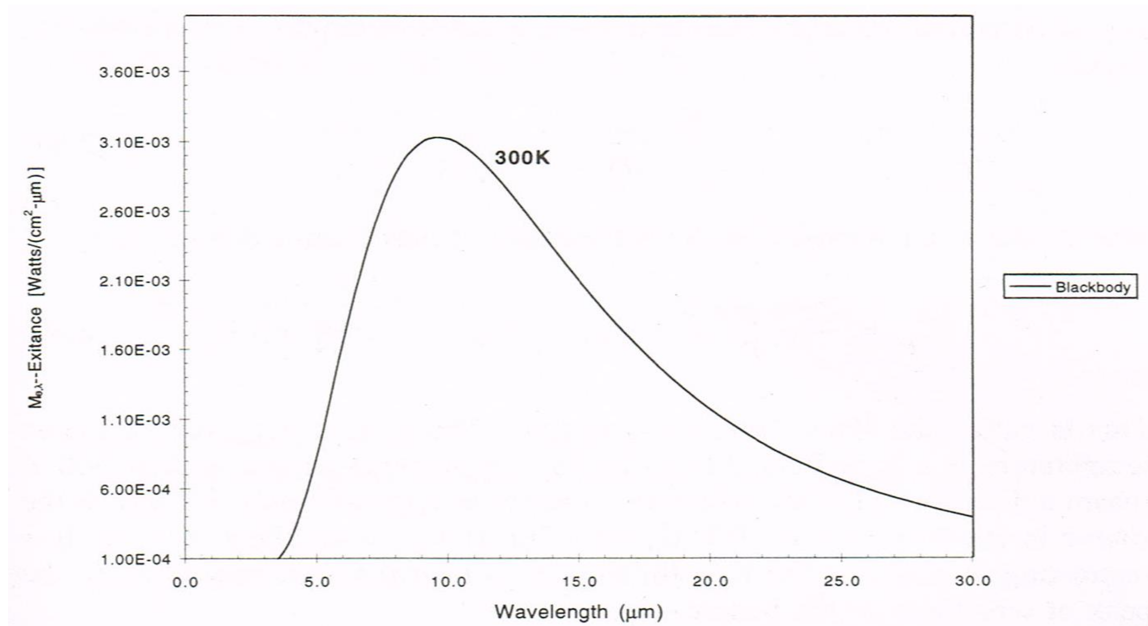

Figure 1.3 Total radiant exitance from a blackbody at 300 K is the area under the spectral exitance curve.
Source: [7].

Differentiating Planck's law and solving for wavelength at the maximum spectral exitance gives Wien displacement law. It quantifies the decreasing wavelength of peak exitance with increase in object temperature, and is expressed in the following equation,

$$\lambda_{max} = \frac{2898}{T} \tag{1.7}$$

where, λ_{max} (μm) is the wavelength at maximum spectral exitance, emitted by an object at a particular temperature T [7]. A blackbody source at T =300 K (room temperature) has a peak exitance at λ_{max}= 9.66 μm.

The blackbody energy spectrum model is an ideal concept, but real sources behave differently. The radiation spectrum of a real body and an ideal blackbody

are related by a factor called emissivity ε, that is the ratio of the radiant exitance of the real source and the radiant exitance of a blackbody, at the same temperature. Emissivity is a dimensionless number that is ≤ 1, and it is = 1 for a blackbody or = 0 for a non-radiant source. A real source is called as a selective radiator if its emissivity depends on wavelength and emissivity is less than unity, or gray-body, if its emissivity is constant and is independent of wavelength. Emissivity depends on the type of material, material surface, wavelength emitted and temperature of the material [7]; it is expressed as,

$$\varepsilon(\lambda, T) = \frac{M_{e,\lambda}(\lambda, T)Source}{M_{e,\lambda}(\lambda, T)Blackbody} \tag{1.8}$$

When radiant energy, ϕ (W), is incident on a surface that is at thermal equilibrium with its surroundings, in order for the energy to be conserved, a fraction of the energy may be absorbed, a fraction of the energy may be reflected and a fraction of the energy may be transmitted [7],

$$\phi_{incident=}\phi_{absorbed} + \phi_{reflected} + \phi_{transmitted} \tag{1.9}$$

Dividing Equation 1.9 by the incident radiation $\phi_{incident}$, Equation 1.10 is obtained,

$$1 = a_{\lambda,T} + r_{\lambda,T} + t_{\lambda,T} \tag{1.10}$$

where, a is the absorptance, r is the reflectance and t is the transmittance. By definition, a blackbody absorbs all the incident radiation; therefore a =1 and r = t = 0.

Kirchoff's law states that if a body is in thermal equilibrium with its surrounding environment at a temperature T, the integrated absorptance a equals the integrated emissivity ε, where absorptance and emittance are function of wavelength λ and temperature T. Kirchhoff's law is valid if there is no significant temperature gradient or if the phonons and electrons are in thermal equilibrium. Kirchhoff's law, on a spectral basis, can be stated as [7],

$$a_{\lambda,T} = \varepsilon_{\lambda,T} \tag{1.11}$$

1.3 Optical Imaging System

The detection of infrared radiation depends on the energy radiated by the source and the optical system that is used for detection. An optical lens is required to collect the incident radiation to be directed to the infrared radiation detector element. Figure 1.4 shows the ray schematic of an imaging system: source-lens-image (detector) [7].

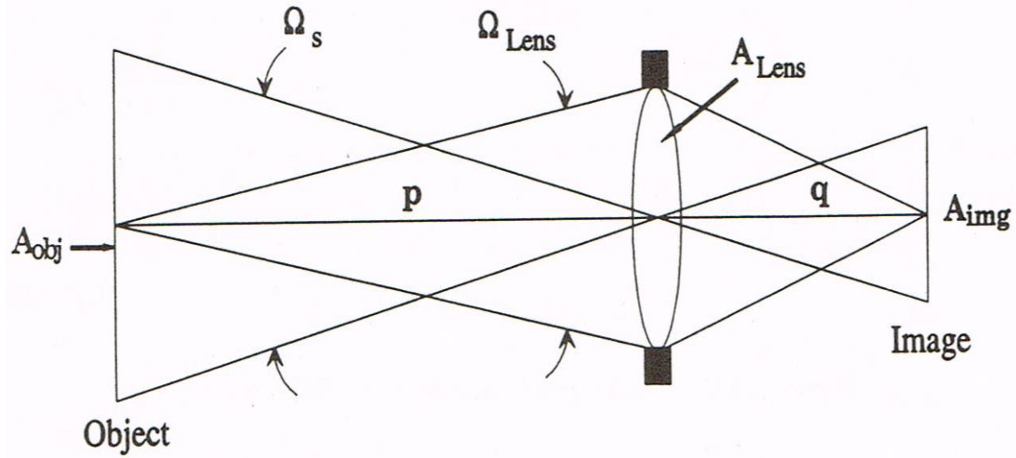

Figure 1.4 Optical detection imaging system.
Source: [7].

The lens aperture A_{lens} acts as a collector receiver and the amount of radiant energy (flux) ϕ (W) collected by the optical system can be expressed as,

$$\phi = LA_{obj}\Omega_{lens} = LA_{lens}\Omega_{obj} \tag{1.12}$$

where A_{obj}, A_{lens} , and A_{img} are the area (cm^2) of the object (radiation source), the area of the lens and the area of the radiation detector A_{det}, respectively; and L (Wcm^{-2}μm^{-1}sr^{-1}) is the spectral radiance emittance. The solid angle of the lens and the solid angle of the image are,

$$\Omega_{lens} = \frac{A_{lens}}{p^2} \tag{1.13}$$

$$\Omega_{obj} = \frac{A_{det}}{q^2} \tag{1.14}$$

where, A_{det} is the area of the radiation detector, p (cm) is the distance between the object (radiation source) and the transmission lens, and q (cm) is the distance between the transmission lens and the radiation detector. Substituting the solid angles into Equation 1.12, the total amount of flux can be expressed as,

$$\phi = L\frac{A_{lens}A_{obj}}{p^2} = L\frac{A_{lens}A_{det}}{q^2} \tag{1.15}$$

where the maximum image quality is obtained when $A_{det} = A_{obj}\left(\frac{q}{p}\right)^2$.

From Equation 1.15, the optical radiation that reaches the detector area is called irradiance E_{det} (Wcm^{-2}). It is the total flux collected by the lens divided by the radiation detector area,

$$E_{det} = \frac{\phi}{A_{det}} = L\frac{A_{lens}}{q^2} \tag{1.16}$$

For distant objects (radiation sources) $p \to \infty$, and distance $q = f$, where f is the focal length of the lens, the focal number of the optic system is defined as,

$$f/_{\#} = \frac{f}{D_{lens}} \tag{1.17}$$

where, D_{lens} is the diameter of the lens. The focal number is related to the dimensions of the diameter of the lens and the distance between the lens and the detection element.

1.4 Infrared Radiation Transmission in Earth's Atmosphere

Earth's atmosphere selectively absorbs and scatters infrared radiation by its composition of gaseous molecules. Figure 1.5 shows the infrared transmission in the earth's atmosphere over 1.8 km as a function of wavelength (0-15 μm) [1]. The infrared radiation transmission in the atmosphere is restricted to three main windows in the following wavelength regions: 0.8-2.5 μm (near IR), 3-5 μm (intermediate IR) and 8-14 μm (far IR). The transmission bands in the atmosphere are due to the IR absorption and scattering by gas molecules such as carbon dioxide (CO_2), ozone (O_3), oxygen (O_2) and water (H_2O) [1].

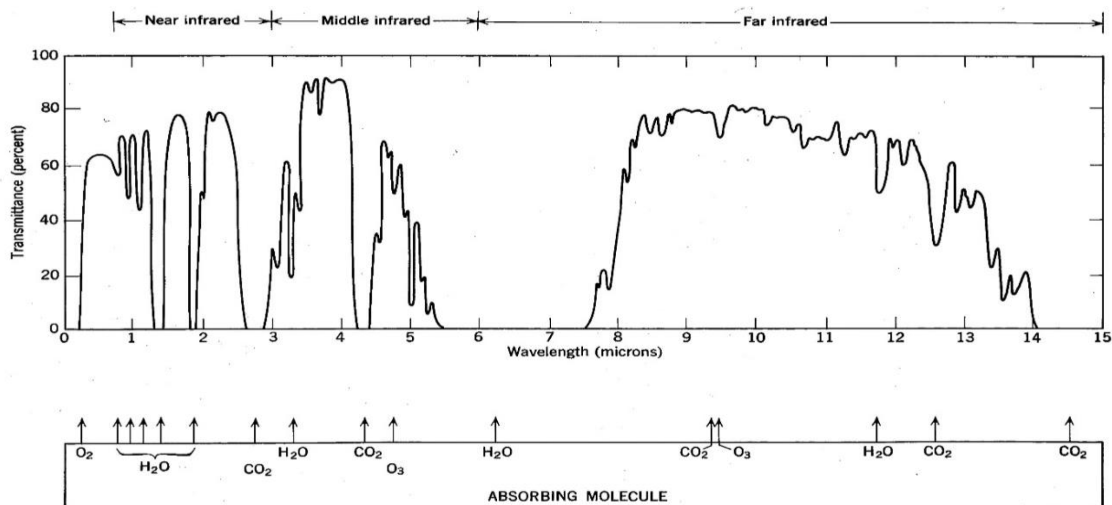

Figure 1.5 Infrared radiation transmission in earth's atmosphere, over 6000 ft horizontal path at sea level, containing 17 mm of precipitate water.
Source: [1].

The three atmospheric infrared transmission windows determine the design and optimization of infrared detectors for each specific infrared window and with a specific detection application [7]. The IR band, 8-14 μm (far IR), is the infrared spectral region of choice for uncooled infrared imaging detection systems due to the existence of an atmospheric window and at room-temperature (300 K), objects register maximum infrared radiation emissivity [8].

CHAPTER 2

OPTICAL DETECTORS

2.1 Optical Detection Classifications

The electromagnetic spectrum range, 0.2-1000 μm, is considered to be optical radiation; it includes visible radiation (0.4-0.75 μm) and infrared radiation (0.75-1000 μm). The infrared radiation spectrum is not visible to the human eye that can just detect wavelengths in the visible range. Infrared radiation is the second most intense source of radiation on earth; this is the reason for the efforts, during the last century, towards the study and development of infrared radiation detectors.

An infrared detector is an opto-electronic device that reacts to infrared radiation, transducing infrared radiation into an electrical signal. Electromagnetic radiation interacts with matter in various ways that determine the physical mechanism involved in the detection process and can be classified as due to: photon effect, thermal effect and wave interaction effect. This radiation-matter interaction depends on the infrared absorber material and the infrared spectral range. Infrared radiation detectors can be classified into two classes: photon detectors and thermal detectors [9].

Thermal detectors respond to the heating effect caused by the absorbed photon radiation that causes changes in the temperature of the detector and in its electrical properties. The detection process of thermal detectors is divided in two steps. First, the radiation is absorbed generating phonons and causing changes in the lattice temperature of the absorber material. Second, the change in temperature induces changes in a measurable parameter of the detector active

element. The response of the thermal detector is proportional to the energy absorbed [9]. Thermal detectors, most used by the infrared industry, are bolometers, thermopiles and pyroelectrics. Bolometers are detectors in which the absorption of radiation causes changes in the electrical resistance of its thermal sensing materials (for example, VOx, a-Si – at room temperature). They exhibit high responsivity and bias is required (DC response). Thermoelectric detectors (thermopiles) are formed by the junction of two materials (Bi/Sb, Al/Poly-Si) with high Seebeck coefficients. They exhibit low responsivity and no bias is required (DC response). Pyroelectric detectors are made using dielectric materials ($LiTaO_3$, $Ba_xSr_{1-x}TiO_3$) that modify their polarization under the influence of changes in temperature and need a chopper system in order to generate a modulation in their polarization. They exhibit high responsivity and no bias is required (current response).

Photon detectors are devices that detect optical radiation by direct interaction of individual photons with active charge carriers within the atomic lattice of the detector material. The transition of the active charges from the valence band to the conduction band depends on the energy band gap of the material and causes changes in physical parameters such as resistance, capacitance, voltage or current [10]. The photodetector response is proportional to the number of photons absorbed [11]. Among the many photon detectors, the photoconductive and the photovoltaic are the most used. Photoconductive detectors use the increase in electrical conductivity resulting from increase in the number of free carriers generated when photons are absorbed (generation of current), whereas in

photovoltaic detectors, current is generated as a result of the absorption of photons due to a voltage difference across a p-n junction (generation of electron-hole pair across the junction and a voltage).

2.2 Photon Detectors Versus Thermal Detectors

A wide variety of photon detectors and thermal detectors have been developed by the infrared detection/imaging industry; each detection mechanism has advantages and disadvantages that determine the most appropriate approach depending on the infrared spectrum range for the detection, application and measurement conditions.

The time response of the thermal detector is a two-step process; it is slower than the corresponding time response of the photon detector, in which the absorption of a photon and the generation of an electron-hole pair is faster. Photon detectors are more sensitive than thermal detectors, but they can only operate at specific and narrow wavelength range in comparison with thermal detectors that can respond continuously over a broad range of wavelengths. Thermal detectors have the advantage to operate at room temperature, in contrast with photon detectors that need to be cooled, as a direct result of the thermal generation-recombination that increases the noise effect. In photon detectors, in order to reduce the thermally induced generation of charge carriers, the temperature of the detector must be maintained at cryogenic levels of 77 K or below [12], by using cooling systems such as Stirling cooling, Peliter cooling etc. This increases the cost, complexity, weight, size and power consumption of the infrared detection

imaging systems [13]. The low cost and portability are the main reasons why uncooled thermal detectors are considered as an alternative to replace cooled photon detectors.

2.3 Thermal Infrared Detector

Thermal detectors have been accepted extensively for applications in infrared detection, where it is impractical to use cooled infrared detectors (for example, military systems, space applications, portable electronics). Among the thermal detectors, the most used is the bolometer. Advantages of bolometer include operation at the desired temperature including room temperature, flat response over the infrared spectrum and conservative time response; this allows to consider bolometer infrared detectors as the ideal choice in the development of uncooled infrared detectors and imaging systems.

2.3.1 Bolometer-Principle of Operation

A bolometer is an infrared thermal detector used in the infrared spectral range that transduces the optical radiation absorbed into an electrical readable signal. A typical bolometer has two main components - an optical radiation absorber material coupled to an active element material. The absorbed incident optical radiation is converted into heat in the lattice by the absorber material, which produces changes in a measurable physical property (electrical resistivity) of the active element material (thermosensing material) and the change is transduced into an electrical output signal [14]. The resistance change information is electrically transferred to the read-out integrated circuit (ROIC) for further

processing and producing a thermal output/image. Figure 2.1 shows the schematic block diagram of a thermal detector [14].

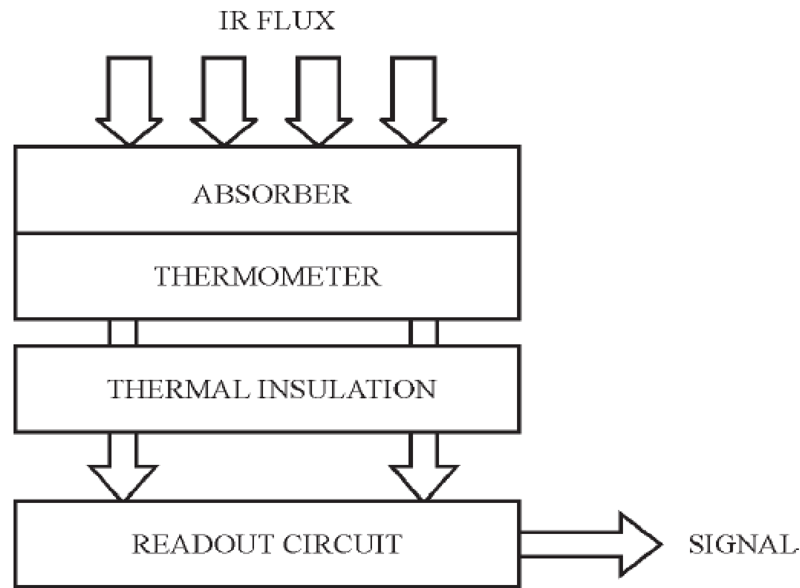

Figure 2.1 Schematic block diagram of a thermal detector.
Source: [14].

The operation of a bolometer is based on the electrical resistance change of a thermosensing material as a function of temperature. The optical radiation absorber and the thermosensing material are connected thermally and electrically through a support structure to the substrate that acts as a heat sink. The basic representation of the thermal detector operation is shown in Figure 2.2. The thermal detector with thermal capacitance C_{th} is connected by a thermal link of thermal conductance G_{th} to a heat sink, assuming that there is no other heat loss path [15].

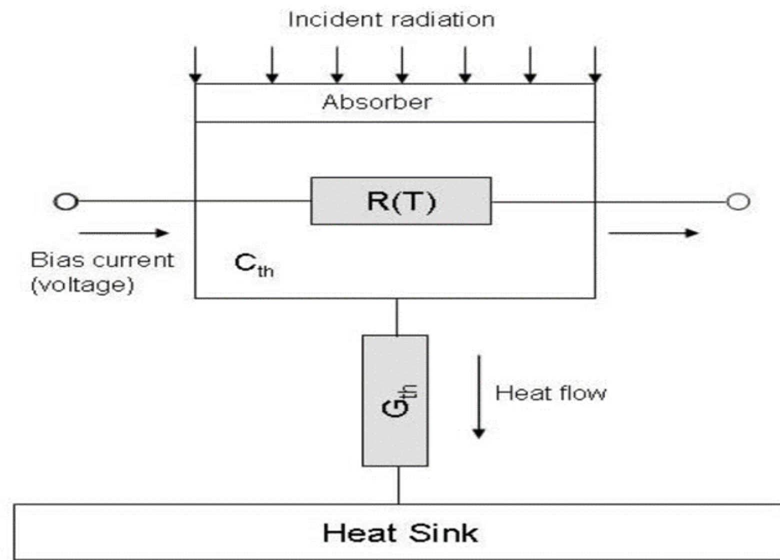

Figure 2.2 Schematic diagram of a thermal detector operation.
Source: [15].

In order to measure changes in its resistance, the bolometer needs to be connected to a DC circuit biased with a constant current source. The electrical circuit, commonly used to interface the bolometer into the reading system, is a voltage divider circuit configuration [16]. Figure 2.3 shows the schematic of a voltage divider circuit. A bias voltage is applied across a load resistor and the bolometer, where V_{bias} (V) is the bias voltage applied to the circuit, R_b (Ω) is the bolometer resistance and R_L (Ω) is the load resistance. The measurement readout electric circuit introduces Joule heating $I_b^2 R_b$ (W) as a source of heat to be considered, where I_b is constant current (A).

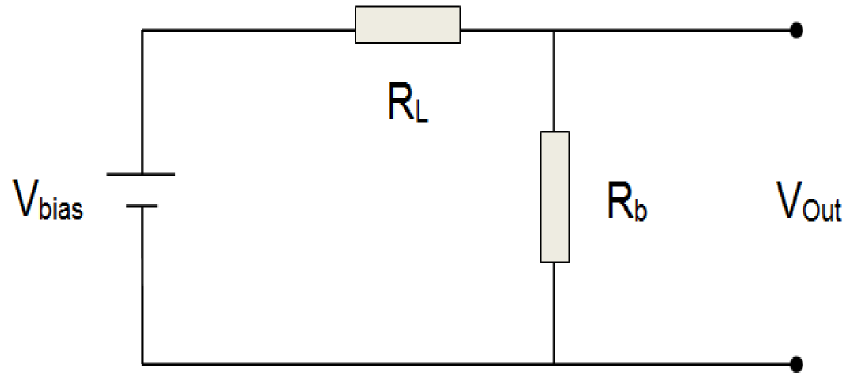

Figure 2.3 Schematic of electrical biasing circuit for bolometer.

2.3.2 Thermal Detector Heat-Balance Equation

The relationship between the incident radiation and heat loss of the thermal detector (bolometer), considering the Joule heat source, can be described by the heat-balance equation [17],

$$C_{th}\frac{d(\Delta T)}{dt} + G_{th}\Delta T = \varepsilon \Phi_i + I_b^2 R_b \qquad (2.1)$$

where, C_{th} (JK^{-1}) is the thermal capacitance coupled via a thermal conductance G_{th} (WK^{-1}) to a heat sink, t (s) is the radiation absorption time, ΔT is the change in temperature between the bolometer and the heat sink due to the incident optical signal Φ_i (Wcm^{-2}), ε ($0< \varepsilon < 1$) is the emissivity (absorptance) of the IR sensitive film, I_b (A) is the circuit biased current and R_b (Ω) is electrical resistance of the bolometer active element.

The thermal capacitance (heat capacity) of the thermal bolometer is given by,

$$C_{th} = \sum_i c_i \rho_i d_i A \qquad (2.2)$$

where, c (Jg^{-1}K^{-1}) is the specific heat capacity of the material, ρ (gm^{-3}) is the density of the material, d (m) is the thickness of the bolometer and A (m^2) is the area of the bolometer. The thermal detector is the combination of a series of thin film layers and the subscript i denotes them.

Assuming that the absorbed incident optical radiation is a modulated function $\Phi_i = \Phi_0 e^{\mathrm{i\omega t}}$, where Φ_0 is the amplitude of sinusoidal radiation and $\omega = 2\pi f$ (rad s^{-1}) is the angular frequency of modulation, the heat-balance Equation 2.1 can be rewritten as,

$$C_{th}\frac{d(\Delta T)}{dt} + G_{th}\Delta T = \varepsilon \Phi_0 e^{\mathrm{i\omega t}} + I_b^2 R_b \qquad (2.3)$$

The thermal conductance G_{th} of the bolometer is the combination of the conductance by convection G_{conv}, the conductance by radiation G_r, and the conductance by conduction G_{cond} throughout the link to the heat sink. Considering that the bolometer is completely isolated from the environment under vacuum conditions, the heat loss of thermal conductance by convection G_{conv} is negligible; therefore the thermal conductance can be expressed by,

$$G_{th} = G_{cond} + G_r \qquad (2.4)$$

The thermal conductance by conduction G_{cond} is the heat conductance through the link to the heat sink and is written as,

$$G_{cond} = \sum_{i} \frac{K_i A_i}{L_i} \qquad (2.5)$$

where, K (Wm^{-1}K^{-1}) is the thermal conductivity of the link, A (m^2) is the area of the link and L (m) is the respective length of the link to the heat sink, and the subscript i denotes the thermal conductance and the dimensions of each thin film layer of the heat link.

When the bolometer absorbs the incident optical radiation and its temperature increases by an amount ΔT, it will radiate a total flux that is estimated by the Stefan-Boltzmann total radiation law. The thermal conductance by radiation, where σ is the Stefan-Boltzman constant [17], is given by,

$$G_r = 4A\varepsilon\sigma T^3 \qquad (2.6)$$

Considering all the heat losses in the thermal detector, the heat-balance Equation 2.3, that describes the relationship between the absorbed optical radiation and the heat loss, can be rewritten as,

$$C_{th} \frac{d(\Delta T)}{dt} + (G_{cond} + 4A\varepsilon\sigma T^3)\Delta T = \varepsilon \Phi_0 e^{\mathrm{i}\omega \mathrm{t}} + I_b^2 R_b \qquad (2.7)$$

The equation relating the thermal detector resistance change with temperature is given by,

$$R_b(T) = R_0(1 + \alpha\Delta T) \tag{2.8}$$

where, $R_b\ (T)$ is the bolometer resistance as function of temperature, R_0 is the bolometer resistance at room-temperature and ΔT (K) is the change in bolometer temperature. TCR, the temperature coefficient of resistance α (%/K), is defined as,

$$\alpha = \frac{1}{R_0}\frac{dR_b}{dT} \tag{2.9}$$

where, dR_b is the change in the bolometer resistance due to the change in bolometer temperature dT.

The response of the bolometer can be measured with a readout circuit interface that typically has a voltage divider configuration; the voltage divider circuit is shown in Figure 2.3. When a DC voltage source sends in a constant current I_b, the output voltage of the voltage divider circuit is given by,

$$V_{out} = V_{bias}\frac{R_b}{R_b + R_L} \tag{2.10}$$

At a constant biased current, from Equation 2.9, the bolometer change in output voltage is,

$$\Delta V_b = I_b \Delta R_b = I_b R_0 \alpha \Delta T = V_{out} \alpha \Delta T \tag{2.11}$$

where, ΔV_b (V) is the voltage change across the bolometer, as function of its temperature change ΔT and resistance change ΔR_b.

The Joule effect term $I_b^2 R_b$ can be expressed as,

$$I_b^2 R_b = \frac{V_b^2 R_b}{(R_L + R_b)^2} \tag{2.12}$$

At thermal equilibrium, when the bolometer is not exposed to optical radiation $\Phi_0 = 0$ and a current bias is applied, then the steady-state solution to Equation 2.7 is,

$$G_0 \Delta T = I_b^2 R_b = \frac{V_b^2 R_b}{(R_L + R_b)^2} \tag{2.13}$$

where G_0 is the thermal conductance of the material at temperature T.

At a constant current bias, the Joule heating depends on the resistance that is temperature dependent; therefore, the joule heat effect is temperature dependent in the dynamic heat Equation 2.7 and solving its derivative with respect to temperature yields,

$$\frac{d}{dT}(I_b^2 R_b) = \frac{d}{dR_b}(I_b^2 R_b)\frac{dR_b}{dT} \tag{2.14}$$

By substituting Equation 2.9 and 2.13 into Equation 2.14, and solving the derivative with respect to bolometer resistance, we get the following equations,

$$\frac{d}{dR_b}(I_b^2 R_b)\frac{dR_b}{dT} = \frac{d}{dR_b}\left(\frac{V_b^2 R_b}{(R_L + R_b)^2}\right)\alpha R_b = \alpha\left[\frac{V_b^2 R_b}{(R_L + R_b)^2}\right]\left(\frac{R_L - R_b}{R_L + R_b}\right) \tag{2.15}$$

From Equation 2.14 and 2.15, the following equation is obtained,

$$I_b^2 R_b = \alpha\left[\frac{V_b^2 R_b}{(R_L + R_b)^2}\right]\left(\frac{R_L - R_b}{R_L + R_b}\right)\Delta T \tag{2.16}$$

For the thermal detector, the thermal heat-balance Equation 2.7 can be rearranged as,

$$C_{th}\frac{d(\Delta T)}{dt} + (G_{cond} + 4A\varepsilon\sigma T^3)\Delta T = \varepsilon\Phi_0 e^{\mathrm{i}\omega\mathrm{t}} + \alpha\left[\frac{V_b^2 R_b}{(R_L + R_b)^2}\right]\left(\frac{R_L - R_b}{R_L + R_b}\right)\Delta T \tag{2.17}$$

$$C_{th}\frac{d(\Delta T)}{dt} + \left[(G_{cond} + 4A\varepsilon\sigma T^3 - \alpha\left[\frac{V_b^2 R_b}{(R_L + R_b)^2}\right]\left(\frac{R_L - R_b}{R_L + R_b}\right)\right]\Delta T = \varepsilon\Phi_0 e^{\mathrm{i}\omega\mathrm{t}} \tag{2.18}$$

where the total thermal conductance of the bolometer depends on the thermal conductance by conductivity in the arms, the thermal conductance by radiation and the joule effect as a function of bolometer temperature change. The effective thermal conductance G_e is defined as,

$$G_e = \left[(G_{cond} + 4A\varepsilon\sigma T^3 - \alpha \left[\frac{V_b^2 R_b}{(R_L + R_b)^2} \right] \left(\frac{R_L - R_b}{R_L + R_b} \right) \right] \tag{2.19}$$

The thermal detector dynamic thermal heat-balance can be finally written as,

$$C_{th} \frac{d(\Delta T)}{dt} + G_e \Delta T = \varepsilon \Phi_0 e^{\mathrm{i}\omega\mathrm{t}} \tag{2.20}$$

Equation 2.20 is an inhomogeneous first-order differential equation and the change in temperature of the bolometer, due to the absorption of incident optical radiation flux, is the solution,

$$\Delta T = T_0 e^{-(\frac{G_e}{C_{th}})t} + \frac{\varepsilon \Phi_0 e^{i\omega t}}{G_e + i\omega C_{th}} \tag{2.21}$$

The first term of the heat transfer solution is a transient term and as time increases, it decreases exponentially to zero. The second term represents the relationship between the incident radiation power and heat loss. The change in

temperature of a thermal detector, due to absorption of incident optical radiation and Joule effect is,

$$\Delta T = \frac{\varepsilon \Phi_0}{(G_e + \omega^2 C_{th}^2)^{1/2}} \quad (2.22)$$

Considering a fixed infrared radiation power, the change in temperature of the device is dominated by the radiation absorption in the absorber material and the thermal conductivity of the support structure**.** Equation 2.22 shows that, in order to achieve a large change in the bolometer temperature, the thermal conductance and the thermal capacity should be as small as possible, and a high emissivity of the optical radiation absorber material is required. It can also be observed that, as ω increases, the term $\omega^2 C_{th}^2$ increases and the temperature change will decrease.

Introducing the effective thermal time constant response τ_e (s) as the ratio of thermal capacity to the thermal conductance, it is defined as,

$$\tau_e = \frac{C_{th}}{G_e} \quad (2.23)$$

The effective thermal time constant or integration time of the system is the time it takes for the detector output to reach a value of 70% of its final, steady state value.

The time response constant is given by Equation 2.23 where the cut-off frequency f_c (-3 dB frequency) of the responsivity is improved by reducing the heat capacity and reducing the thermal conductance of the detector element.

Equation 2.22 can be rewritten as,

$$\Delta T = \frac{\varepsilon \Phi_0}{G_e(1 + \omega^2 \tau_e^2)^{1/2}} \tag{2.24}$$

The effective thermal time constant characterizes the radiation flux transition between the low and high frequency regions. At low frequencies, the detector temperature is inversely proportional to the thermal conductance of the heat link. At high frequencies, the detector temperature is inversely proportional to the thermal capacitance and falls off inversely with the frequency of the optical signal.

At low frequencies $\omega^2 \tau_e^2$ <<1 $$\Delta T = \frac{\varepsilon \Phi_0}{G_e} \tag{2.25}$$

At high frequencies $\omega^2 \tau_e^2$ >>1 $$\Delta T = \frac{\varepsilon \Phi_0}{\omega C_{th}} \tag{2.26}$$

2.3.3 System Noise

The detector output signal is disturbed by a variety of noise sources, resulting in random fluctuations of the measured signal. The performance of an optical detector is determined by the noise, which is the combination of the noise

generated by the detector, the noise generated by readout electronic system and the noise from the radiation background against which the signal is detected [18]. Noise sets the limit to the minimum optical radiation power to be detected and dictates the detector design parameters to be considered to achieve a high signal to noise detection system. The noise sources are required to define the detectors' figures of merit such as noise equivalent power NEP and normalized detectivity D^*.

The total noise of the bolometer is the combination of thermal fluctuation noise, Flick noise (1/f), thermal background fluctuation noise and Johnson noise [17]. The square of the total noise voltage of the detection system is,

$$V_n^2 = V_j^2 + V_{th}^2 + V_b^2 + V_{1/f}^2 \tag{2.27}$$

The Johnson noise or Johnson-Nyquist noise V_j (V) is associated with electrical resistors and is caused by the thermal agitation of atoms and charge carriers within a conductor material. In order to minimize this, the detector resistance R, temperature T and the measurement noise bandwidth Δf , related to the integration time, should be minimized. Johnson noise is defined by Equation 2.28, where k_B is the Boltzmann constant and R is the detector resistance at room temperature [18].

$$V_j^2 = 4k_BTR\Delta f \tag{2.28}$$

The thermal fluctuation noise V_{th} (V) is caused by temperature fluctuations in the detector and is caused by fluctuation in the rate at which heat is released from the detector to its surroundings with which it is thermally connected. This noise is inherent of thermal detectors and its main heat loss is through the thermal link connected to the heat sink. The thermal fluctuation voltage noise is derived from the heat-balance equation [18] and expressed as,

$$V_{th}^2 = \frac{4k_B T^2 \Delta f}{G_e(1+\omega^2\tau_e^2)} \frac{\Delta V}{\Delta T} \tag{2.29}$$

where, ΔV is the change in the electrical output of the detector corresponding to the detector change of temperature ΔT.

The background noise V_b (V) is caused by the radiative heat exchange between the detector and the surrounding environment that is being observed [19].

$$V_b^2 = \frac{8k_B \varepsilon\sigma A(T_d^2 - T_b^2)}{G_e^2(1+\omega^2\tau_e^2)} \left(\frac{\Delta V}{\Delta T}\right)^2 \tag{2.30}$$

where A is the optical radiation absorber area of the detector, T_d is the detector temperature and T_b is the temperature of the surrounding observed environment.

The Flick noise (1/f) is a component caused by conductivity fluctuations [19] in all resistors and can be described by the empirical equation,

$$V_{1/f}^2 = k_{1/f} \frac{I^\delta}{f^\beta} \Delta f \tag{2.31}$$

where the coefficient $k_{1/f}$, is a factor of proportionality, and coefficients β and δ have values of about 1. These coefficients depend on the methods of material preparation and processing.

The Flick noise (1/f) is attributed to surface factors (McWhorter model) and to bulk defects (Hoogen model). The McWhorter model implies fluctuations in the number of carriers [17] and the Hoogen model considers the carrier mobility [21]. 1/f is a conductivity noise that, for low frequencies, tends to be the limiting factor, depending on the number of effective carriers and not the number of carriers. The number of effective carriers is reduced due to scattering with crystal lattice imperfections, non-Ohmic contacts and grain boundaries [22].

2.3.4 Figures of Merit

The detector performance can be described quantitatively and evaluated in terms of figures of merit. Figures of merit are parameters that relate the detector response to the optical absorbed radiation and characterize the performance of optical detectors. Some figures of merit allow to compare the performance between optical detectors, independent of their optical radiation absorption mechanism, while others are dependent on these mechanisms and detector geometry dimensions.

The performance of a bolometer is determined by figures of merit such as responsivity R_v, noise equivalent power NEP and normalized detectivity D^*.

The responsivity R_v (V/W) of the detector anticipates the signal output for a specific optical radiation absorbed. Responsivity is defined as the ratio of the output signal ΔV_b to the input radiant power incident that is absorbed, Φ_0, by the detector and is given by [1],

$$R_v = \frac{\Delta V_b}{\Phi_0} \tag{2.32}$$

When the detector is interfaced with a voltage divider configuration readout circuit as shown in Figure 2.3, substituting Equations 2.10, 2.11 and 2.24 in Equation 2.32, the responsivity can be rewritten as,

$$R_v = \frac{\varepsilon\alpha}{G_e(1+\omega^2\tau_e^2)^{1/2}} \frac{V_{bias}R_b}{(R_b+R_L)} \tag{2.33}$$

The detector output signal must be above the detector noise level that determines the minimum absorbed optical radiation level the detector can discern; the noise equivalent power NEP (W) is the signal power needed to achieve a signal-to-noise ratio of 1, and it can be expressed in terms of responsivity as [1],

$$NEP = \frac{V_n}{R_v} \tag{2.34}$$

The normalized detectivity D^* (cmHz$^{1/2}$W^{-1}) is the reciprocal of the noise equivalent power normalized to 1-cm^2 area and 1-Hz noise equivalent bandwidth and is defined as [1],

$$D^* = \frac{\sqrt{A_d \Delta f}}{NEP} \tag{2.35}$$

where, A_d (cm^2) is the area of the detector (area of radiation absorption) and Δf (Hz) is the detector noise equivalent bandwidth related to the modulation frequency of the radiation source. The normalized detectivity defines the resolving power of the detector and allows to compare the detector performance with different sizes and technology.

The detector noise equivalent bandwidth is the frequency over which the noise is measured and is expressed as,

$$\Delta f = \frac{1}{2\pi\tau_e} \tag{2.36}$$

The figures of merit mentioned before are the parameters that allow the characterization of infrared detectors (single element) and their performance comparison with other infrared detectors, independent of the radiation absorption mechanism and the active area of absorption. The figures of merit and the various device parameters that are described above are applicable to array/s of detectors.

An optical infrared imaging system consists of an array of infrared detectors located at the focal plane (FPA) of an optical detection imaging system, integrated with a read-out integrated circuit (ROIC). The arrays can be one-dimensional (1D) or two-dimensional (2D), depending on the purpose and application of the imaging system/s. A significant figure of merit of the infrared imaging system is the noise equivalent temperature difference $NETD$ (mK) [23], that is defined as,

$$NETD = \frac{4\left(f/_{\#}\right)^{2}\sqrt{\Delta f}}{\tau_a \tau_0 \sqrt{A_d}\, D^{*}\left(\Delta L/_{\Delta T}\right)_{\lambda 1-\lambda 2}} \tag{2.37}$$

where, $f/_{\#}$ is the focal number of the optical detection imaging system, A_d is the detector area, τ_0 is the transmittance of the optics system, τ_a is the atmospheric transmittance and $\left(\Delta L/_{\Delta T}\right)_{\lambda 1-\lambda 2}$ is the temperature contrast of total spectral radiance emittance at 300 K, and represents the change in IR radiation power detected on the detector element per unit change in temperature of the source object within the spectral wavelength band under consideration.

The $NETD$ parameter is referred as thermal contrast and measures the smallest temperature change that a thermal infrared detector is able to distinguish between the infrared radiation source and its background. $NETD$ is typically expressed in milli-Kelvin (mK) and is inversely proportional to the detectivity. Commercial state-of-the-art uncooled infrared bolometer arrays have typically $NETD$ values in the order of less than 100 mK.

2.3.5 Optical Infrared Imaging System

A determining figure of merit used by the imaging industry, to characterize and compare the performance of an optical infrared imaging system (array of infrared detectors) that could be used to calculate the performance of a single detector, is the noise equivalent temperature difference $NETD$ (Equation 2.37); this parameter specifies the minimum detectable temperature difference by the detection system.

IR Cameras Manufacturers measure $NETD$, using different parameters, but the most important is the focal number $f/_{\#}$ of the optical lens used during the measurements. The comparison of different imaging systems' detection performance is based on the comparison of the $NETD$ values with the same $f/_{\#}$, that is usually normalized to 1. For an imaging system to have a considerable performance, the $NETD$ should be less than 100 mK and for a state-of-the-art system, it should be less than 50 mK. Another important parameter, in the imaging industry, is the frame rate at which the camera operates; standard FPA systems operate in a range of 9-100 Hz and is typically in the range of 30-60 Hz. The frame rate is the rate at which the FPA imaging system creates images and a common practice is to make the detector (pixel) thermal time response not to exceed one-third of the reciprocal of the frame rate. Equation 2.38 shows the frame rate relationship with the detector thermal time constant,

$$Frame\ rate = \frac{1}{3\tau_e} \tag{2.38}$$

Figure 2.4, shows the schematic diagram of a standard optical system, where f is the focal length. Using optics lens with larger diameters allows to build more sensitive IR thermal imaging systems (cameras), but glass lens does not have a high IR radiation transmittance and optics lens made of high IR transmittance germanium (Ge) are used by the IR industry. Germanium optics lenses are expensive and an increase in the diameter of the optical lens results in an increase in the cost of the IR thermal camera; this is the reason why manufacturers use optics lens with small diameters, or high focal number.

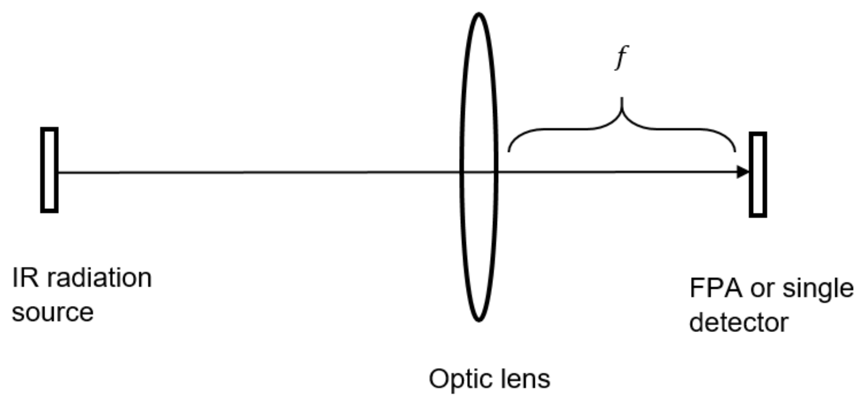

Figure 2.4 Schematic diagram of optical system.

CHAPTER 3

MODELING OF RADIATIVE PROPERTIES

3.1 Radiation-Matter Interaction

Electromagnetic wave radiation interacts with matter in three ways: reflection, absorption and transmission. The reaction of atoms to an incoming radiation is determined by the frequency of the incoming radiation; if its energy matches one of the excited states of the atoms, the radiation is absorbed, and if its frequency is lower than the resonance frequencies of the atoms, the radiation is scattered [24].

The interaction of radiation with matter is determined by the radiation wavelength and the optical properties of the material. The index of refraction n and the extinction coefficient k describe the material optical properties. The index of refraction is generally a complex number that consists of a real and imaginary part [25],

$$\bar{n} = n + ik \tag{3.1}$$

The real term $n = c/v$ represents the wave phase velocity, where c is the speed of light, v is the wave velocity in the medium and the imaginary term k represents the absorption losses of the electromagnetic wave by the media. The extinction coefficient k represents the degree of damping of the radiation wavelength.

The optical properties can be represented as the complex dielectric function (permittivity),

$$\bar{\varepsilon} = \varepsilon_1 + i\varepsilon_2 \qquad (3.2)$$

where $\varepsilon_1 = n^2 - k^2$ is the real term and $\varepsilon_2 = 2nk$ is the imaginary term called the absorption product. The complex dielectric function is frequency dependent and is related to the electronic structure and band structure of the material.

Combining Equation 3.1 and 3.2, the following equations are obtained,

$$n^2 = \frac{1}{2}\left(\sqrt{{\varepsilon_1}^2 + {\varepsilon_2}^2} + \varepsilon_1\right) \qquad (3.3)$$

$$k^2 = \frac{1}{2}\left(\sqrt{{\varepsilon_1}^2 + {\varepsilon_2}^2} - \varepsilon_1\right) \qquad (3.4)$$

The permittivity, index of refraction and extinction coefficients should be measured at the same wavelength, because they are wavelength dependent.

The optical properties n, k, ε_1 and ε_2 can be deduced by measurement techniques that have been developed to calculate these properties as a function of radiation reflected, absorbed and transmitted by a material. The nature of the material determines the technique that can be used to measure its optical properties; each technique has specifications and advantages. Some of these techniques include the analytical approaches such as Kramers-Kronig analysis, or

the experimental techniques such as spectroscopic ellipsometry and differential reflectrometry [26].

The radiative properties of a medium can be predicted by the Fresnel's equations. The Fresnel's equations are derived from Maxwell's electromagnetic equations by applying the boundary conditions at the boundary between two media. The reflected and transmitted component of the radiation depends on the angle of incident radiation with respect to the interface of the medium and the optical properties of the interface. When the multilayer stack has more than three layers, a transfer matrix method is considered to analyze and solve the propagation of radiation throughout a multilayer medium.

3.2 Matrix Method (Multi-Rad)

Multi-Rad is an optical modeling software developed by Massachusetts Institute of Technology (MIT) [27]. Multi-Rad facilitates the calculation of the optical radiative properties of thin-film stacks using the matrix method of multilayers [28-30]. This method predicts the reflectance and transmittance of a multilayer stack with the assumption that the layers are optically smooth, parallel and optically isotropic (the optical constants are independent of the crystallographic direction). The radiative properties can be calculated considering optical radiation at different angles of incidence (0-90°) in the spectral range of 0.4-20 µm at a determined thin-film stack temperature (30-1400 ˚C). For a multilayer stack, with specific values of index of refraction n and extinction coefficient k for each layer, at specific temperature, angle of incident radiation and wavelength range of incident radiation, the radiative

properties such as absorptance, reflectance and transmittance are determined [27].

For normally incident radiation, the coherent optical reflectance and transmittance of a multilayer structure are readily represented as a product of matrices. A multilayer structure, composed of optically isotropic and homogeneous layers, with plane and parallel faces, is assumed for this matrix method. The elements of the system, transfer matrix, can be written in terms of the complex-amplitude reflection and transmission coefficients of the multilayer structure [31].

A generic layer structure is shown in Figure 3.1. “There are N layer interfaces (circled) and $N+1$ “layers” (squared), including the unbounded transparent media on each side of the actual stack. A_i and B_i are the amplitudes of the forward and backward propagating electric field vectors on the left side of interface i. The prime notation on A'_{N+1} and B'_{N+1} indicates that these are the amplitudes on the right side of interface N. Light is incident on interface 1, with an angle of incidence θ_1 [32].”

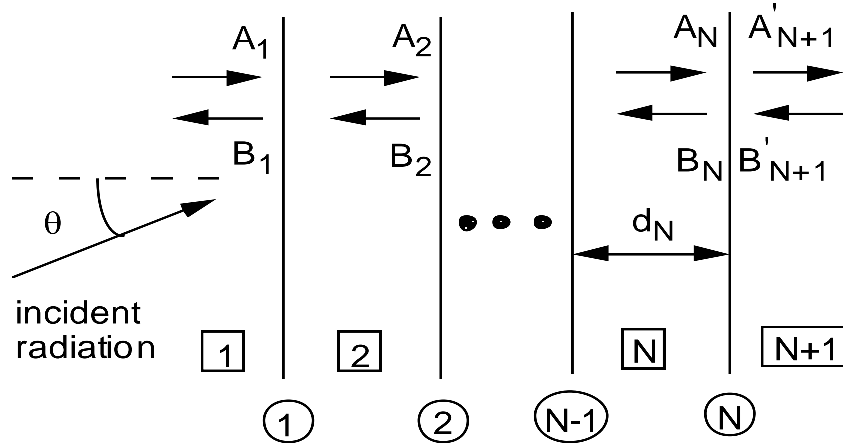

Figure 3.1 Notation of matrix method of multilayers.
Source: [31].

The multilayer theory relates the amplitudes on the left side of interface 1 with those on the right side of interface N and is expressed in this equation:

$$\begin{pmatrix} A_1 \\ B_1 \end{pmatrix} = \left[\prod_{i=1}^{N} P_i D_i^{-1} D_{i+1} \right] \begin{bmatrix} A'_{N+1} \\ B'_{N+1} \end{bmatrix} = \begin{bmatrix} m_{11} & m_{12} \\ m_{21} & m_{22} \end{bmatrix} \begin{bmatrix} A'_{N+1} \\ B'_{N+1} \end{bmatrix} \tag{3.5}$$

“where P_i is the propagation matrix, D_i is the dynamical matrix, and m_{ij} is an element of the transfer function matrix. The propagation matrix accounts for the effect of absorption and interference within a layer i bounded by two interfaces [32].”

In this approach, it is assumed that the bounding media is vacuum and because layer 1 is not bound by two interfaces, the propagation matrix P_i is,

$$P_i = \begin{bmatrix} e^{i\phi_i} & 0 \\ 0 & e^{-i\phi_i} \end{bmatrix} \tag{3.6}$$

The propagation matrix accounts for the effect of absorption and interference within a layer bounded by two interfaces, where the phase shift is,

$$\phi_i = 2\pi \bar{n}_i d_i \cos \bar{\theta}_i / \lambda \tag{3.7}$$

The complex refractive index is $\bar{n}_i = n_i + ik_i$, where n_i is the refractive index and k_i is the extinction coefficient of the i layer. The thickness of each layer is d_i, $\bar{\theta}_i$ is the complex angle and the wavelength of the incident wave in vacuum is λ.

The dynamical matrix D_i relates the amplitudes of the reflected and refracted radiation waves at the interface i, and it depends on the state of polarization of the radiation wave. The dynamical matrix solution for the electric field vector perpendicular (s) and parallel (p) to the plane of incident is given by,

$$D_i = \begin{pmatrix} 1 & 1 \\ \bar{n}_i cos\bar{\theta}_i & -\bar{n}_i cos\bar{\theta}_i \end{pmatrix} \text{ s wave} \tag{3.8}$$

$$D_i = \begin{pmatrix} cos\bar{\theta}_i & cos\bar{\theta}_i \\ \bar{n}_i & -\bar{n}_i \end{pmatrix} \text{ p wave} \tag{3.9}$$

The reflectance for the multilayer stack, for an electric field vector perpendicular (s) and parallel (p) to the plane of incidence is the ratio of the intensities of the forward and backward propagating waves on the left side of interface 1 and is given by Equation 3.10. The transmittance is the ratio of the

intensities of the forward propagating wave on the right side of the interface N and the forward propagating wave on the left side of interface 1 and is given in Equation 3.11.

$$R_{s/p} = \frac{B_1}{A_1} = \left|\frac{m_{21}}{m_{11}}\right|^2 \tag{3.10}$$

$$T_{s/p} = \frac{\bar{n}_{N+1}\cos\theta_{N+1}}{\bar{n}_1\cos\theta_1}\frac{A'_{N+1}}{A_1} = \frac{\bar{n}_{N+1}\cos\theta_{N+1}}{\bar{n}_1\cos\theta_1}\left|\frac{m_{21}}{m_{11}}\right|^2 \tag{3.11}$$

The spectral directional absorptance is calculated by assuming Kirchhoff's law on a spectral basis:

$$\alpha_{\lambda,\theta} = \varepsilon_{\lambda,\theta} = 1 - R_{\lambda,\theta} - T_{\lambda,\theta} \tag{3.12}$$

where, absorptance $\alpha_{\lambda,\theta}$, emittance $\varepsilon_{\lambda,\theta}$, reflectance $R_{\lambda,\theta}$ and transmittance $T_{\lambda,\theta}$ are function of wavelength λ and incident angle of the incoming radiation θ (directional properties). Kirchhoff's law, on a spectral basis, is valid if the emitting object is in local thermodynamic equilibrium and it can be characterized by a single temperature. The emission and absorption coefficients depend on the nature of the surface (roughness) and wavelength. Kirchhoff's law is valid if there is no significant temperature gradient or if the phonons and electrons are in thermal equilibrium [32].

Multi-Rad predicts the radiative properties for a specific wavelength range and the total values of radiative properties as a function of the wavelength range. In order to calculate the total IR radiation absorbed, reflected and transmitted in a certain spectral range, the radiative properties are integrated with respect to wavelength for a certain blackbody distribution of energy .The total absorptance in a band i is [27],

$$\alpha_i = \frac{1}{\sigma T_b^4 \phi_{T_s}^k} \int_{\lambda_1}^{\lambda_2} e_b(\lambda, T_b) \alpha_\lambda(\lambda) d\lambda \tag{3.13}$$

where, $\phi_{T_s}^k$ is the fraction of the blackbody energy in the spectral range evaluated at the blackbody temperature, e_b is the Planck function evaluated at the blackbody source temperature T_b in the spectral range $\lambda_1 - \lambda_2$ and α_λ is the spectral absorptance. The emittance, transmittance and reflectance are calculated similarly to Equation 3.13.

CHAPTER 4

UNCOOLED MICROBOLOMETER

4.1 Background

A microbolometer is an infrared detector that is generally fabricated by micromachining technology. A microbolometer consists of a thin multilayer structure thermally isolated and connected to a substrate, through support structures that act as heat links and electrical connectors. The two main components of the multilayer structure are an optical infrared absorber material coupled to a thermosensing material. The absorbed incident optical radiation is converted into heat by the infrared absorber material, producing changes in the resistivity of the thermosensing material that is transduced into an electrical signal.

A wide variety of materials have been used in the design and fabrication of microbolometers, and new absorbers and thermosensing materials have been considered to improve the performance of these devices in the last decade.

Historically, black metals (platinum, tungsten, titanium and gold) have been used as absorbers of optical infrared radiation since the 1930's [33-37] and have been extensively utilized as infrared absorber coatings. Surface modification techniques such as electroplating, chemical and mechanical etching have been traditionally used to achieve high porosity metal surfaces that are the most effective mechanism for the absorption of infrared radiation [38,39]. New surface modification techniques such as femtosecond lasers have been implemented in

the fabrication of black metals that exhibit an extremely low reflectance across the infrared wavelength spectra [40].

New IR radiation absorber materials have emerged with extremely low reflectance exhibited across the IR spectra. Vantablack, a composite of thin film of carbon nanotubes and black silicon (BSi), a surface modification of silicon, exhibits absorptance close to unity [41-45]. Black gold with infrared absorptance close to unity have been developed [46]; but the thin film fabrication process technology that is required for the deposition of these materials may not be compatible with all semiconductor processes and it does not allow the mass production of uncooled microbolometers [47,87]. Black gold, obtained by thermal evaporation methods, exhibits an absorptance close to unity [49-51]; but the fragile structure of this material and the degradation in absorption properties, when it is exposed to temperatures higher than 300 ºC, does not make it feasible for mass production [52].

A variety of polycrystalline materials such as Vanadium oxide (VO_x) and amorphous silicon (a-Si) have been widely used as IR thermosensing materials [53-55]; these materials have the advantage of high temperature coefficient of resistance required by the imaging industry to achieve a high sensitivity detector response.

Vanadium oxide (VOx) has been the thermosensing material of choice in a variety of microbolometers [56] with temperature coefficient of resistance in the range of -2 to -3 %/ K [57-60] at room temperature, but it is not a standard material in the integrated circuit (IC) fabrication process technology [61]. Vanadium oxide

is not a single crystal material and compositional variations have to be controlled very precisely; it has some problems such as unstable phases, and poor reproducibility [62,63]. Thin films of vanadium oxide can be prepared by a variety of techniques, including reactive RF sputtering [64-66], pulsed laser deposition [67], ion beam sputtering and magnetron controlled sputtering that are high cost methods [68,69].

Amorphous silicon (a-Si), an alternative material that is compatible with the silicon technology, requires high values of electrical resistivity in order to achieve a high TCR [70-72]. In order to achieve a TCR of -3 to -4 %/K [73] at room temperature, amorphous silicon should be exposed to high annealing temperatures resulting in a high electrical resistivity and a high pixel resistance in the order of Mega-Ohms (MΩ) [74]. This high value of resistance causes large Johnson noise and consequently low detector sensitivity as well as a mismatch with the input impedance of the CMOS read-out circuits.

The disadvantage of these materials is that both of them exhibit high 1/f noise due to their non-crystalline structure. For most materials, 1/f noise constant is not very well documented in the literature. It is a material parameter that can vary by several orders of magnitude for different materials. Even small variations of the material composition can dramatically change the 1/f noise constant [75].

The complexity in the fabrication process technology, that is required for the deposition and patterning of these thermosensing materials and the high electrical resistivity needed to achieve high TCR, does not make them cost-effective for mass commercialization.

Previously, some experimental studies have been performed to develop the use of n-type silicon to optimize uncooled bolometers [76]. An uncooled microbolometer structure with n-well layer as the active element has been proposed and fabricated [77-79]. However, n-Si has not been used in the fabrication and development of commercial uncooled infrared microbolometers that is dominated by VO_x [80] and other polycrystalline materials. n-Si requires an intermediate step in the form of heavily doped n-Si (n^{++} -Si) for forming an Ohmic contact with the metal.

4.2 Microbolometer - Materials Selection

In the present study, low doped p-type silicon Si (1.45 Ω-cm) as an active thermosensing element is introduced in combination with silicon nitride (Si_3N_4) as an infrared absorber material. The $NETD$ of state-of-the-art uncooled infrared microbolometer is limited by the 1/f noise from the thermosensing material [81,82]. Mono-crystalline materials can have a significantly lower 1/f noise constant as compared to amorphous or polycrystalline materials. Thus, the use of mono-crystalline silicon as a thermosensing material will reduce the $NETD$ of a microbolometer with a low 1/f noise constant [83,84]. Aluminum (Al) is considered as interconnection material because of its electrical properties and gold (Au) is used as an infrared radiation reflector layer.

4.2.1 P-Silicon as Thermosensing Material

The process of doping introduces impurities in the intrinsic Si semiconductor via substitutional atoms such as boron or phosphorous with lower or higher valence,

respectively. This increases the charge carrier density and the intrinsic semiconductor becomes an extrinsic semiconductor. These impurity atoms are called donors if they add electrons to the conduction band or acceptors (holes) if they add positive charges to the valence band.

Depending on the type of dominant carriers, the extrinsic semiconductor is called n-type or p-type. Silicon doped with phosphorous receives an extra free electron resulting in n-type Si. Silicon doped with boron creates holes resulting in p-type Si. The energy gap for acceptor and donor levels with respect to the corresponding energy bands is smaller than the energy gap between the valence and conduction bands [85].

As shown in Figure 4.1, the migration of an electron from the valence band to the acceptor band leaves behind a hole in the valence band. In a p-type extrinsic semiconductor, the majority carriers are holes in the valence band and they are called positive carrier type (p-type); the binding energy (activation energy E_a) is small and while the holes are the charge carriers, the electrons participate in bonding [86]. Figure 4.1 shows the energy bands in a p-type extrinsic semiconductor, where E_a is the acceptor band energy, E_{f1} is the Fermi energy for an intrinsic semiconductor, E_c is the conduction band energy, E_f is the extrinsic Fermi energy and E_v is the valence band energy.

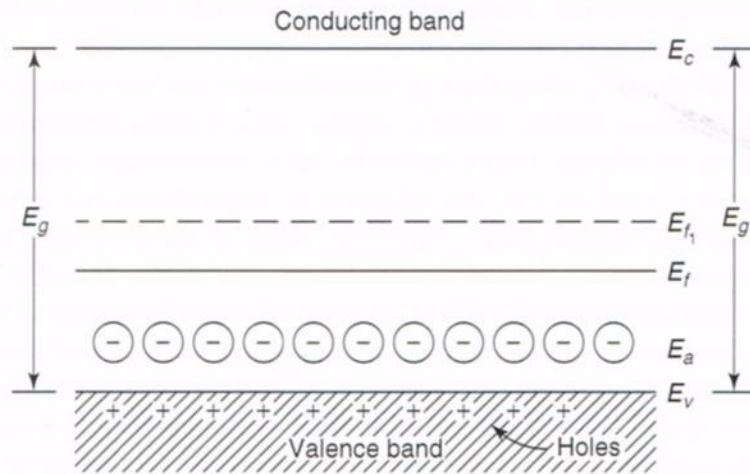

Figure 4.1 Energy bands in a p-type extrinsic semiconductor.
Source: [86].

When a trivalent atom such as boron is introduced substitutionally in the crystalline silicon covalent bonded lattice of silicon, one of the covalent bonding orbital is missing and a hole is created. In the presence of an external electric field, an electron carrier from another tetrahedral bond can attain sufficient energy to move to the missing bond ionizing with charge of -1 from the boron atom and creating a boron-silicon valence bond. The migration of an electron from a silicon atom to a boron atom is only 0.005 eV small compared with 1.1 eV required to transfer an electron from the valence band to the conduction band. Figure 4.2 shows the creation of the hole by the ionization of boron; it behaves as a positive charge that moves in the crystal silicon lattice in the direction of the negative terminal [86].

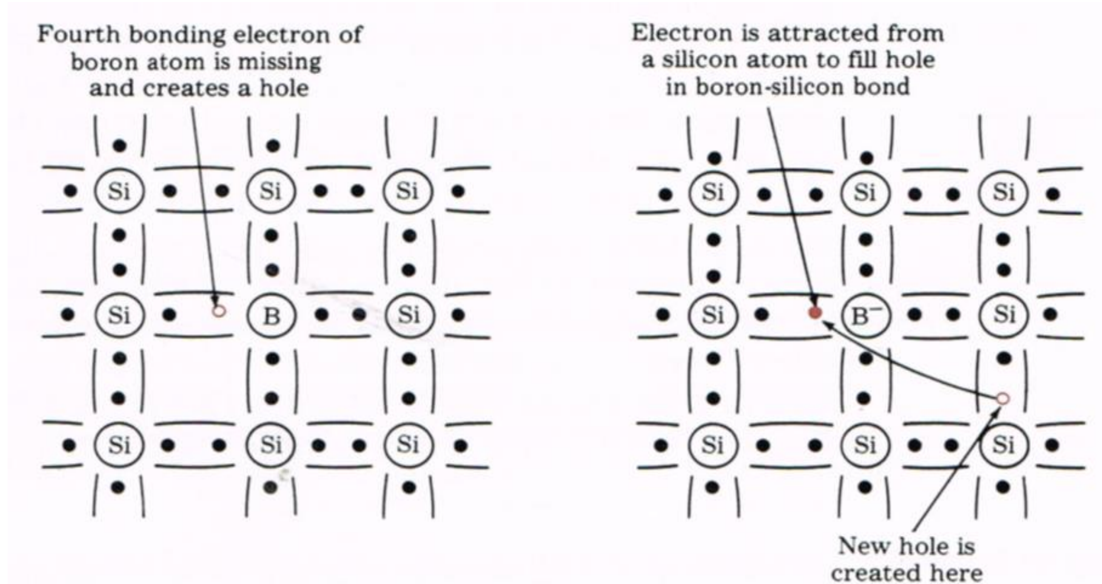

Figure 4.2 Carrier transport in p-type extrinsic semiconductor.
Source: [86].

Electrical conductivity in intrinsic semiconductors is an exponential function of temperature and band gap; the conductivity of extrinsic semiconductors is a function of charge carrier density and charge carrier mobility. At low temperature, the electrical conductivity increases as the charge carrier concentration increases; at intermediate temperature, the number of charge carriers is nearly independent of temperature (exhaustion range); at higher temperatures, the carrier mobility decreases as a result of increase in phonon scattering; at still higher temperatures, once the charge carriers are completely ionized, the extrinsic semiconductor behaves as an intrinsic semiconductor [87].

The thermosensing p-type silicon layer is considered with a doping concentration of 10^{16} cm^{-3} with a TCR of 0.74 %/K [88,89]. Figure 4.3 shows the results of measurements by the National Bureau of Standards (now, NIST – the National Institute of Standards and Technology) of the temperature coefficients of

resistance at a temperature of 23 °C for n-type and p-type silicon [89]. The TCR of silicon is determined by the type of carrier, carrier concentration and carrier mobility. Although the TCR value is low in comparison with the standard thermosensing materials used by the infrared detector industry, the use of p-doped silicon has some significant advantages. These include low resistivity that reduces pixel resistance and Johnson noise, low resistance values that are compatible with readout circuits, negligible 1/f noise due to its single crystal nature and it is a cost-effective manufacturing technology (MEMS technology).

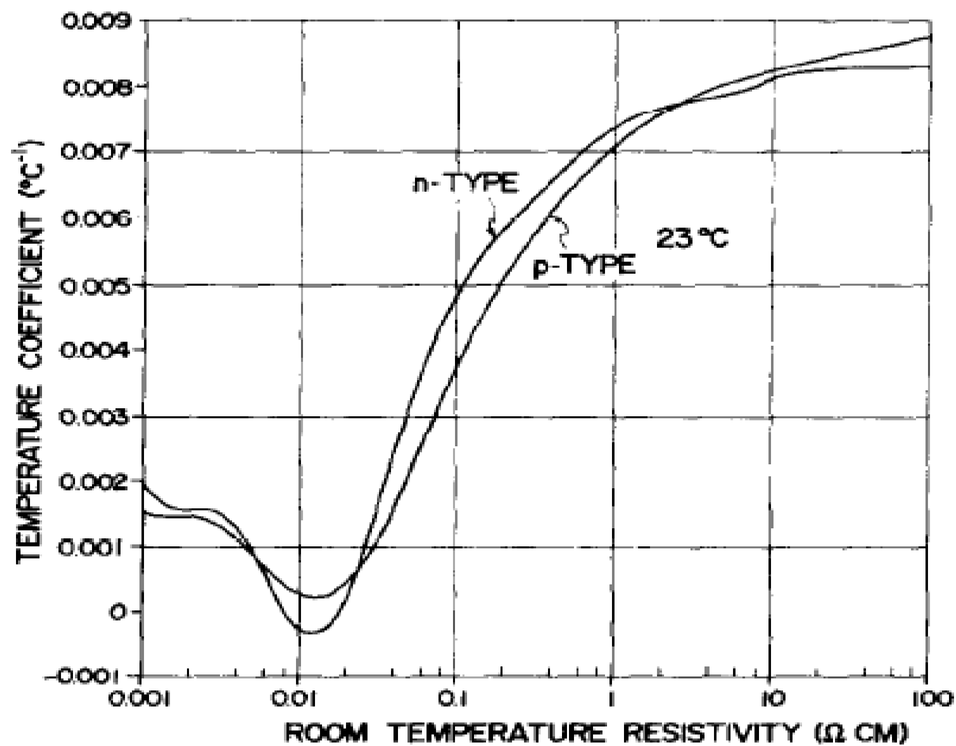

Figure 4.3 TCR as a function of electrical resistivity for n-type and p-type silicon (23 ºC).
Source: [89].

4.2.2 Radiative Properties of Thin Films of Common Dielectric Materials

For the manufacture of microbolometers, for excellent absorbers, there is a need for low-cost standard semiconductor materials with high emissivity in the IR spectral range. These materials also need to be compatible with the actual manufacturing process as well as integrate with the required optoelectronic circuits.

In this study, radiative properties of common dielectric materials such as Al_2O_3, SiO_2, AlN and Si_3N_4 are simulated in the infrared spectral range of 1.5-14.2 μm. These common dielectric materials are routinely used as electrical insulators, anti-reflection coatings as well as passivation layers in a variety of applications including microbolometers, light emitting diodes, displays, sensors, solar cells and other photonic devices. In particular, the design of coatings (highly reflective and anti-reflective) requires accurate knowledge of the radiative properties of the dielectric material.

With the rapid growth of application of materials in the infrared and advancements in related technology, manufacturers have begun to utilize infrared materials in the design and manufacture of micro-optics components such as band-pass filters, beam splitters, lenses, mirrors, and polarizers in the IR. These IR materials vary in their optical, mechanical, thermal and electrical properties, and these properties determine their applications in the IR.

In this study, the radiative properties of dielectric materials for varying thicknesses at room temperature, are simulated using Multi-Rad. The thin films (dielectric materials) are considered to be suspended (free standing) in vacuum. A

standard blackbody is considered as the source of infrared radiation with an angle of incidence normal to the thin film surface (Blackbody temperature = 30 ºC; zero transmittance losses between source and sample). The smaller increment in spectral wavelength is 0.1 μm and the range of wavelengths in which the radiative properties are simulated is 1.5-14.2 μm.

In Figures 4.4 and 4.5, plots of emissivity, reflectance and transmittance in arbitrary units, for varying thickness (0.1-3 μm) of the dielectric materials (Al_2O_3, SiO_2, AlN and Si_3N_4), at room temperature (30 ˚C), are presented for the infrared wavelength range of 1.5-14.2 μm. The range of thickness of the dielectric films, considered in this study, are consistent with the industry standards.

As can be seen in Figure 4.4a, the absorptance increases with increase in thickness of Al_2O_3 for the wavelength range of 4-14.2 μm, reaching its peak value of 0.76 at a wavelength of 13.6 μm. It may be observed that the transmittance, with varying thickness, is higher than 0.8 in the wavelength range of 1.5-8.5 μm; it shows a decreasing trend with increasing thickness in the wavelength range of 8.5-14.2 μm. The corresponding reflectance is less than 0.2 in the wavelength range of 1.5 -10.9 μm; as can be seen in the wavelength range of 9.6-14 μm, the reflectance increases as the thickness is increased, reaching a peak value of 0.31 at the wavelength of 12.3 μm.

Figure 4.4b shows the increase in absorptance with increasing SiO_2 thickness. In the wavelength range of 4.8-14.4 μm, three peak values are observed at wavelengths of 8.4, 9.9 and 12.4 μm, with respective emissivity values of 0.60,

0.70 and 0.60. As can be noted, the transmittance is higher than 0.89 in the wavelength range of 1.5-7.5 μm, with a decreasing trend in the wavelength range of 7.5-14.2 μm as the thickness is increased. The lowest values of transmittance, with varying thickness, occur at 9.3 μm and 12.5 μm. It is observed that the reflectance increases with thickness, in the wavelength range of 7.4-14.2 μm, reaching its highest value of 0.7 at 9 μm.

As can be seen in Figure 4.5a, the absorptance increases with increasing AlN thickness in the wavelength range of 7-14.2 μm, reaching a peak value of 0.68 at 11.2 μm. It is found that the transmittance is higher than 0.64 in the wavelength range of 1.5-10.2 μm; it shows a decreasing trend with increase in thickness for wavelengths longer than 10.2 μm. The corresponding reflectance is increasing with increase in thickness, in the wavelength range of 10.2-14.2 μm, reaching the highest value of 0.45 at 14.2 μm.

It is noted from Figure 4.5b that for Si_3N_4, the absorptance increases, as the thickness is increased, in the wavelength range of 5-14.2 μm, reaching its highest peak value of 0.84 at 9.4 μm. An increase in the Si_3N_4 membrane thickness causes an increase in the peak amplitude and it shifts to lower wavelengths. It is found that the transmittance is higher than 0.5 in the wavelength range of 1.5-6 μm, with a trend of decrease in transmittance with increase in thickness for wavelengths longer than 6 μm.

In addition to the wavelength-dependent fundamental optical constants, n and k, the peaks in emissivity at different wavelengths (8-14 μm), for these

materials, is due to the associated vibrational modes of molecules. The implication of these peaks and the corresponding wavelengths is that these materials are useful candidates in the manufacture of microbolometers.

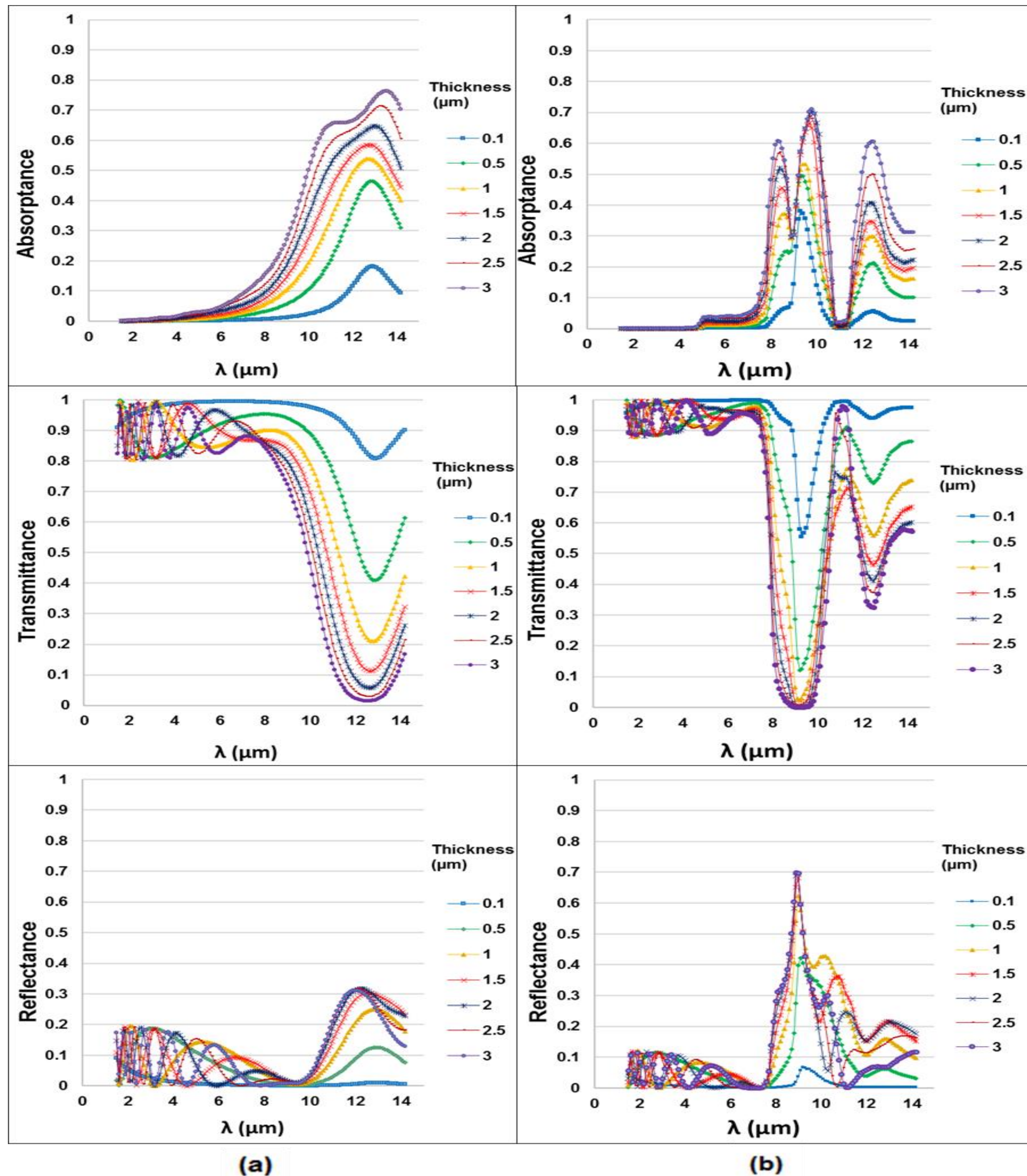

Figure 4.4 Absorptance, transmittance and reflectance for varying thicknesses of (a) Al_2O_3 and (b) SiO_2, at room temperature (30 ºC).

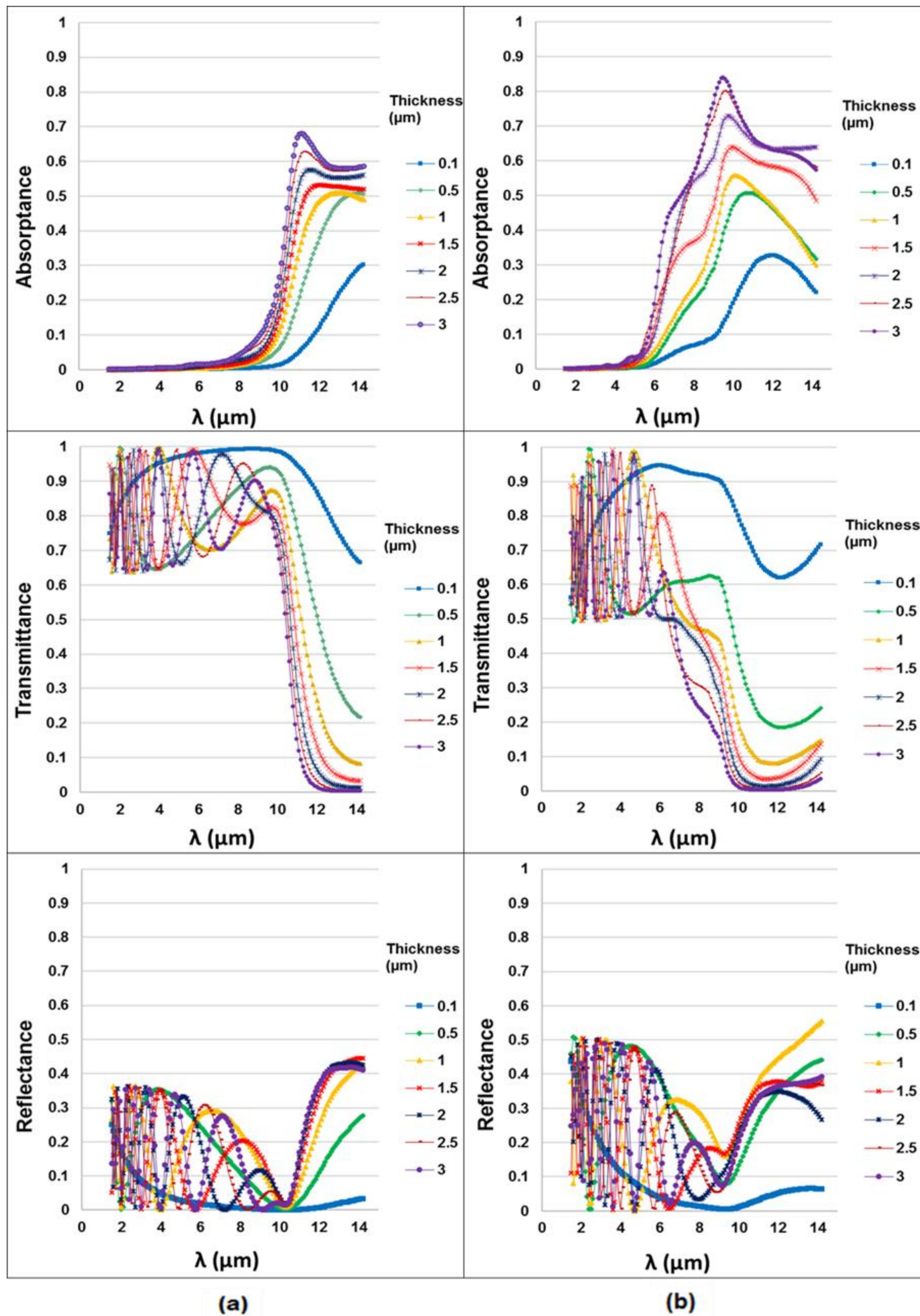

Figure 4.5 Absorptance, transmittance and reflectance for varying thicknesses of (a) AlN and (b) Si_3N_4, at room temperature (30 ºC).

Tables 4.1-4.4 summarize the total infrared radiative properties of the dielectric materials studied in the spectral range considered (1.5-14.2 μm). From these tables, it is observed that Si_3N_4 exhibits the highest total absorptance values throughout the varying thickness range. The results of the evolution of radiative properties, as a function of dielectric material thickness, suggest the possibility to consider Al_2O and Si_3N_4 as viable candidates to be used as IR radiation absorbers in the fabrication of uncooled microbolometers in the infrared spectral range of 8-14 μm (atmospheric window).

These results demonstrate that Si_3N_4 exhibits the highest total emissivity values in the spectral wavelength range of 8-14 μm, throughout the varying thickness range. Therefore, Si_3N_4 is considered in this study as the IR radiation absorber material of choice in the design of the proposed uncooled microbolometer in the infrared spectral range of 8-14 μm (atmospheric window).

Table 4.1 Total Value of Radiative Properties of Al_2O_3 (spectral range: 1.5-14.2 μm)

Thickness (μm)	0.1	0.5	1	1.5	2	2.5	3
Absorptance	0.052	0.168	0.233	0.280	0.328	0.375	0.415
Transmittance	0.945	0.782	0.660	0.594	0.548	0.505	0.468
Reflectance	0.030	0.050	0.106	0.126	0.124	0.120	0.117

Table 4.2 Total Value of Radiative Properties of SiO_2 (spectral range: 1.5-14.2 μm)

Thickness (μm)	0.1	0.5	1	1.5	2	2.5	3
Absorptance	0.061	0.141	0.182	0.227	0.266	0.297	0.329
Transmittance	0.927	0.744	0.616	0.558	0.540	0.529	0.506
Reflectance	0.011	0.115	0.202	0.215	0.194	0.174	0.164

Table 4.3 Total Value of Radiative Properties of AlN (spectral range: 1.5-14.2 μm)

Thickness (μm)	0.1	0.5	1	1.5	2	2.5	3
Absorptance	0.065	0.167	0.206	0.235	0.264	0.289	0.311
Transmittance	0.925	0.702	0.588	0.566	0.549	0.519	0.493
Reflectance	0.010	0.124	0.205	0.199	0.188	0.191	0.197

Table 4.4 Total Value of Radiative Properties of Si_3N_4 (spectral range: 1.5-14.2 μm)

Thickness (μm)	0.1	0.5	1	1.5	2	2.5	3
Absorptance	0.170	0.316	0.351	0.462	0.545	0.567	0.589
Transmittance	0.796	0.413	0.319	0284	0.224	0.189	0.167
Reflectance	0.034	0.270	0.330	0.254	0.231	0.244	0.245

4.2.3 Dielectric Materials as Infrared Filters

IR optical filters are used in many systems for military and commercial applications. These IR filters are essential components in the development of optical sensing systems that can be optimized by using materials better suited to the task. Materials such as calcium fluoride, germanium, optical glass N-BK7 and potassium bromide are the standard IR filter materials used by the IR industry, but at the microfabrication level, there is a need to replace them with new materials that are more compatible with the actual silicon-based microfabrication process.

Table 4.5 provides a detailed comparison of the cut-off wavelengths and IR transmittance of the dielectric materials that have been considered, with varying thickness, in the spectral range of 1.5-14.2 μm. The results show that these dielectric materials can be considered as IR band-pass filters to transmit certain wavelength band at wavelengths in the IR spectral range and to block others (by

reflection and absorption) at longer wavelengths. From Figures 4.4 and 4.5, a trend in suppressing the IR radiation at longer wavelengths, as the thickness of the dielectric materials increase, is observed.

The results of the evolution of the radiative properties, as a function of dielectric material thickness, show the possibility to consider these dielectric materials as band-pass optical filters and absorber materials in the IR spectral range considered.

Table 4.5 Band-pass Range and Transmittance for Various Dielectric Materials Considered as IR Filters (spectral range: 1.5-14.2 μm; 30 ˚C)

Dielectric Materials	Al_2O_3	SiO_2	AlN	Si_3N_4
Band-pass range (μm)	1.5-8.5	1.5-7.5	1.5-10.2	1.5-6.0
Transmittance	≥ 0.80	≥ 0.89	≥ 0.64	≥ 0.50

4.2.4 Silicon Nitride as IR Radiation Absorber

Silicon nitride (Si_3N_4) is commonly used in the semiconductor industry as a passivation layer in integrated circuit (IC) fabrication, because it protects the electronics from the diffusion of water and alkali ions [90]. Silicon nitride is an excellent dielectric material [91] with a dielectric strength of the order of 10^7 V/cm and a reasonable thermal conductivity that is required to transfer heat from the microbolometer multilayer structure to the substrate [92]. Thin silicon nitride membranes are almost transparent in the infrared range except for a wide absorption peak exhibited around 12 μm [93]; this absorptance peak is due to the

vibrations of the diatomic basis of silicon nitride and it grows in amplitude as the nitrogen content is raised [94]. An increase in the silicon nitride membrane thickness causes an increase in the peak amplitude and it shifts to lower wavelength [95].

4.2.5 Microbolometer - Electrical Interconnection and IR Reflective Layer

In this study, aluminum (Al) was selected as an electrical interconnection material to the read-out integrated circuit (ROIC) because it provides an excellent Ohmic contact with the low doped p-Si thermosensing element [96]. When the device is heated to about 550 $^{\circ}$C, after the aluminum interconnection layer has been deposited on p-type silicon, aluminum diffuses into silicon yielding a highly conductive heavily doped p^{+}-region. Aluminum is commonly used as interconnect due to its low electrical resistivity (ρ=2.65 μΩ-cm) that introduces a low noise contribution to the system [97]. Also, aluminum is easy to deposit, does not contaminate Si and exhibits excellent adhesion to dielectrics.

The proposed microbolometer structure is suspended over a cavity with a gold (Au) layer deposited under it and on top of the substrate surface. Gold has a high reflectivity close to unity in the infrared region. The gold layer, in combination with the cavity thickness, creates a resonant cavity, enhancing the radiation absorptance of the multilayer stack.

4.2.6 Optical Constants of Microbolometer Materials

The microbolometer materials were chosen, based on their electrical, thermal, mechanical and optical properties. The interaction of radiation with matter is determined by the radiation wavelength, the surface nature and the optical

properties of the material. The index of refraction n and the extinction coefficient k describe the material optical properties and determine their radiative optical properties.

Silicon is almost transparent in the infrared wavelength range. The optical constants of the thermosensing p-type silicon layer, considered with a low doping concentration of 10^{16} cm^{-3}, are similar to that of undoped silicon. Figure 4.6 shows the optical constants of silicon, in the infrared spectral range of 0-25 μm [98]. As can be seen in this figure, the extinction coefficient is negligible throughout the infrared spectral range. An increase in the silicon membrane thickness causes an increase in the absorptance of the incident radiation.

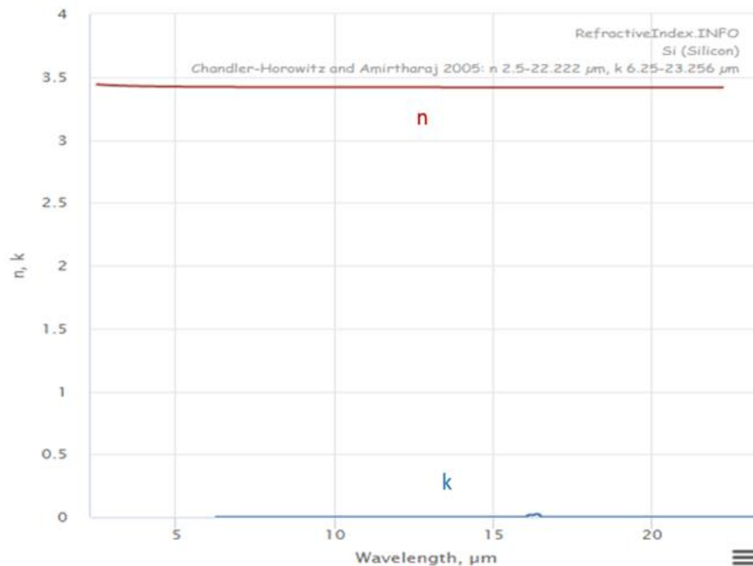

Figure 4.6 Optical constants (n and k) of silicon.
Source: [98].

Thin silicon nitride membranes are almost transparent in the infrared range except for a wide absorption peak that is exhibited around 12 μm. Figure 4.7 shows

the optical constants of silicon nitride in the infrared spectral range of 0-15 µm. It is evident from this figure that the peak of the extinction coefficient is at 12 µm. This peak is due to the vibrations of the diatomic basis of silicon nitride [94]. An increase in the silicon nitride membrane thickness causes an increase in the absorptance of the incident radiation.

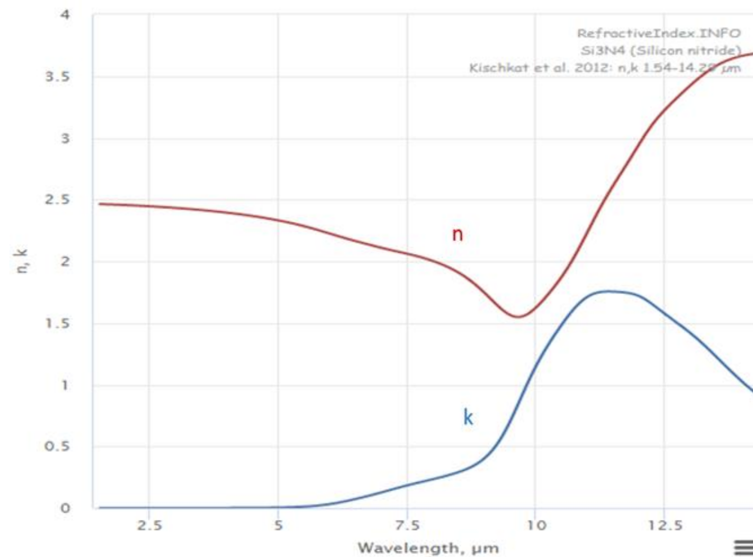

Figure 4.7 Optical constants (n and k) of silicon nitride.
Source: [99].

Metals with large electrical conductivities are characterized by a large reflectivity in the infrared spectral range. Gold and aluminum have a high reflectivity close to unity in the infrared region considered, that is suggested by large extinction coefficient throughout the infrared spectral range. Figures 4.8 and 4.9 show optical constants of aluminum and gold in the infrared spectral range of 0-200 µm and 0-25 µm, respectively [100,101]. Gold is utilized as the infrared radiation reflective layer to enhance the radiation absorptance of the multilayer stack chosen in this work, because aluminum can be oxidized as a result of the

microfabrication process, reducing its reflective properties in the infrared spectral range.

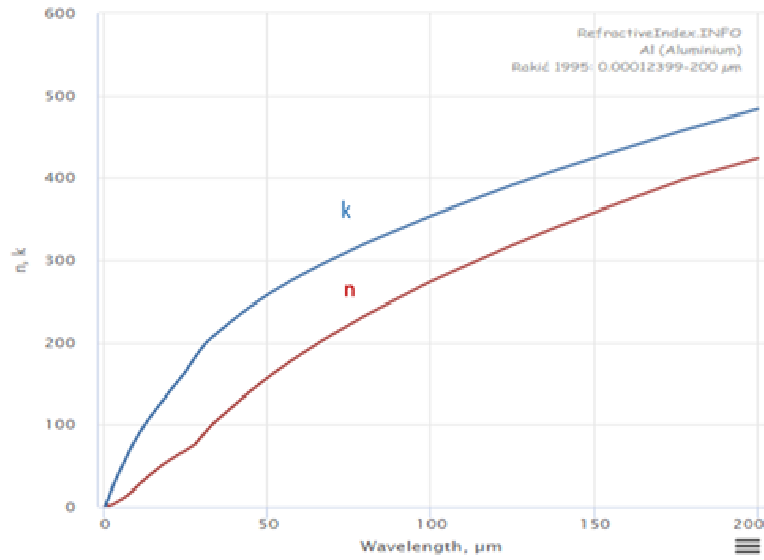

Figure 4.8 Optical constants (n and k) of aluminum.
Source: [100].

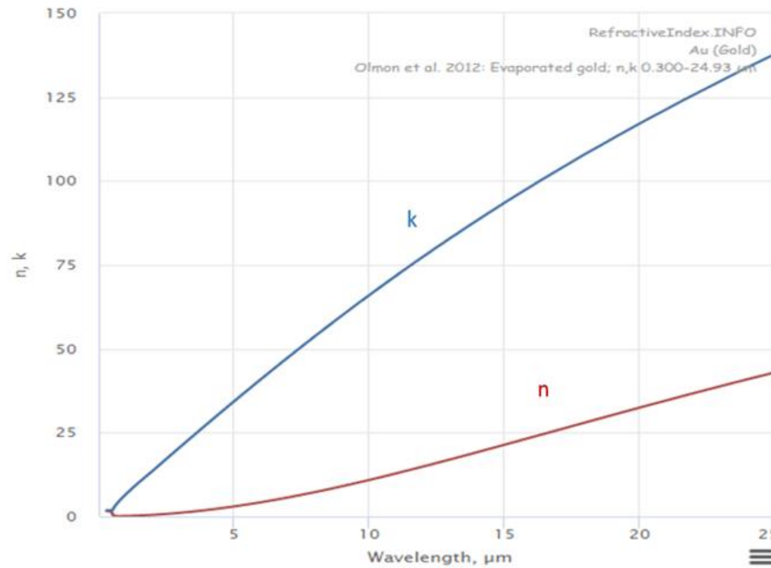

Figure 4.9 Optical constants (n and k) of gold.
Source: [101].

The total reflectivity values of aluminum and gold are predicted by Multi-Rad, as function of thin film thickness, in the spectral range considered (8 – 14 μm). When the thin film thickness is larger than 0.1 μm, the total reflectivity is constant; the transmittance is negligible and the absorptance is less than 2%, as can be seen in Figure 4.10.

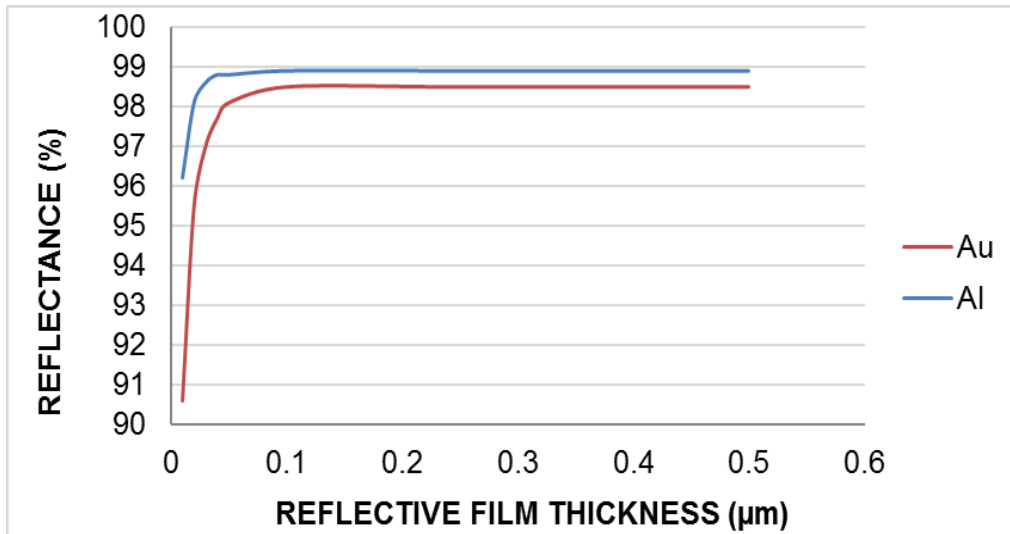

Figure 4.10 Total reflectance of aluminum and gold.

4.3 Microbolometer Structural Design

In a standard infrared imaging system, single IR detector elements (pixels) are laid out in a two-dimensional array, called focal plane array (FPA). The microbolomer, proposed in this work, has the potential for applications in focal plane array imaging systems. The thermal isolation and efficient radiation absorption of single detector elements (microbolometers) are the key factors for high performance infrared focal plane array systems [102].

The uncooled microbolometer two-level structure, considered in this study, was originally developed and patented by Honeywell Inc., and licensed to several companies for the development and manufacture of focal plane arrays of uncooled microbolometers.

The performance of a microbolometer is determined by the material characteristics and its structural design parameters (structure geometry and dimensions) [103]. In order to obtain a high performance microbolometer, some conditions are required in the design of the multilayer structure. These include the following:

1- High temperature coefficient of resistance, TCR, of thermosensing material;
2- Efficient absorption of IR radiation by the absorber layer;
3- Low thermal conductance with surroundings;
4- Low thermal capacitance of pixel;
5- Fast response;
6- Low noise.

Efficient IR radiation absorption by the absorber layer, in combination with a thermosensing material with high TCR, provides a high responsivity of the microbolometer.

A high TCR of the thermosensing material is key to the performance of the detector. In order to obtain a high TCR, a low doping concentration that leads to a high electrical resistivity is required. This increases the Johnson noise and is undesirable for the read-out integrated circuit. Consequently, a trade-off must be found between the TCR and the detector electrical resistivity.

One of the most important microbolometer design parameters is a low thermal conductance between the bolometer and its surroundings (important at low frequencies); this is the reason why conventional bolometers operate in a vacuum package to reduce the thermal conductance between the bolometers and their surroundings through the surrounding gas. The vacuum environment makes possible that the principal heat loss occurs by the conduction path through the support structure of the suspended membrane to the substrate. Microbolometers need to be packaged in vacuum with vacuum levels < 0.01 mbar [104]. The support structure provides three functions: mechanical support, a thermally conducting path, and an electrically conducting path. The thermal conductance through the supports arms can be minimal, reducing the cross-sectional area, increasing the length and using materials with low thermal conductivity. The optimum thermal isolation of the microbolometer structure can be obtained in devices with the microbolometer multilayer structure suspended over a cavity [105].

In order to minimize the thermal capacitance (important at high frequencies) per unit of area of the microbolometer, it is needed to reduce the thermal mass of the multilayer structure while maintaining a high absorption. The lower the thermal capacitance of the suspended structure, the lower the thermal time constant response required by the imaging system [106].

The most important parameters of a thermal infrared sensor for use in an imaging system are high responsivity and short thermal time constant response. High responsivity is achieved by increased absorption and a short thermal time response requires small heat capacity of the structure and a high thermal

conductance to the substrate. When the thermal conductance decreases, the thermal time constant response increases and the responsivity decreases. When the thermal capacity decreases, the thermal time constant response decreases and the responsivity decreases. A desired high responsivity and fast thermal time constant response in a microbolometer cannot be achieved; a trade-off is needed depending on the microbolometer application requirements [107].

In the proposed two-level structure, an upper square-shaped multilayer stack is thermally isolated in vacuum and connected to the substrate through two legs, that act as structural support (Si_3N_4), thermal path and interconnection (Al) to the read-out integrated circuit (ROIC) on the substrate. The thermally isolated structure consists of a suspended membrane (detector element) composed of three layers: Si_3N_4 layer as a passivation and antireflective element, low doped p-type silicon layer acting as a thermosensing active element and Si_3N_4 as an IR radiation absorber layer. The lower level (silicon substrate) consists of a thin layer of Au acting as an IR radiation reflection layer, deposited on a silicon dioxide (SiO_2) layer on top of the substrate (Si). The two multilayers are separated by a cavity (gap) that, in combination with the thin film of Au, creates a resonant cavity and increases the infrared radiation absorption in the infrared region considered. In order to enhance the IR radiation absorption in the microbolometer upper level membrane, a resonant optical cavity (Fabry-Perot) structure that is optimized for the targeted wavelength interval is required [108]. The two-level microbolometer thin film layer structure is as shown in Figure 4.11.

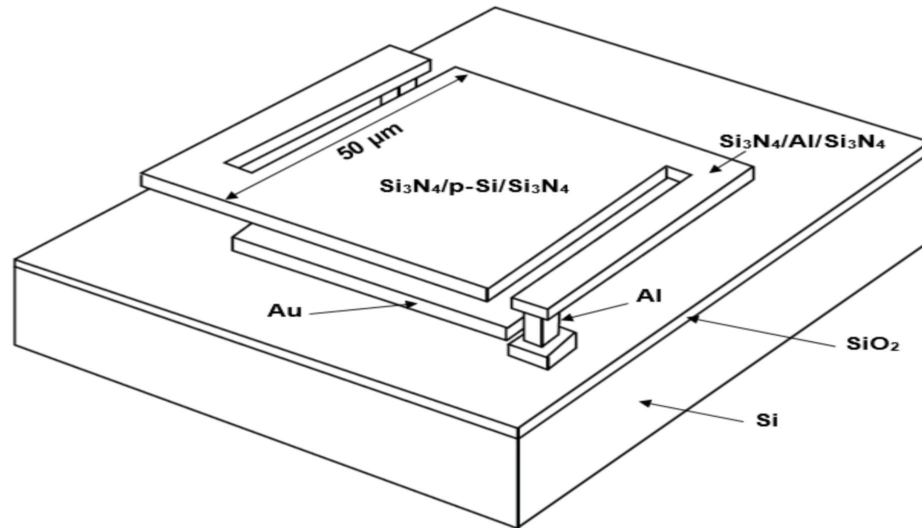

Figure 4.11 Schematic of the proposed microbolometer (Two-level 50 x 50 μm^2).

4.4 Optimization of Microbolometer Radiative Properties

Optical modeling of radiative properties of materials is an essential tool that provides the theoretical information required to be considered in the optimization and structural design approach. In the proposed microbolometer, the optical radiative properties of the microbolometer multilayer structure are predicted using the matrix method of multilayers (Multi-Rad). The simulated results help to understand the material properties and integration process and, at the same time, reduce the fabrication costs.

The stacked layer structure of the proposed microbolometer is considered to be at room temperature (30 ºC), thermally isolated and suspended in vacuum, i.e. "free standing", as shown in Figure 4.12. A standard blackbody is considered as the source of infrared radiation (30 ºC, zero transmission loss). The incident radiation angle is considered to be perpendicular to the surface of the stacked layer; the smaller increment in spectral wavelength is 0.1 μm and the range of

wavelengths in which the spectral radiative properties are calculated is 8-14 μm (atmospheric window).

The optical constants of the materials, considered in the design (Al, Au, and Si_3N_4) of the multilayer stack, are from the sources in the literature [94, 98, 99, 100, 101,109,110]; the optical constants of Si and low doped p-Si are from the Multi-Rad data. All material optical properties were validated with experimental data provided by the literature.

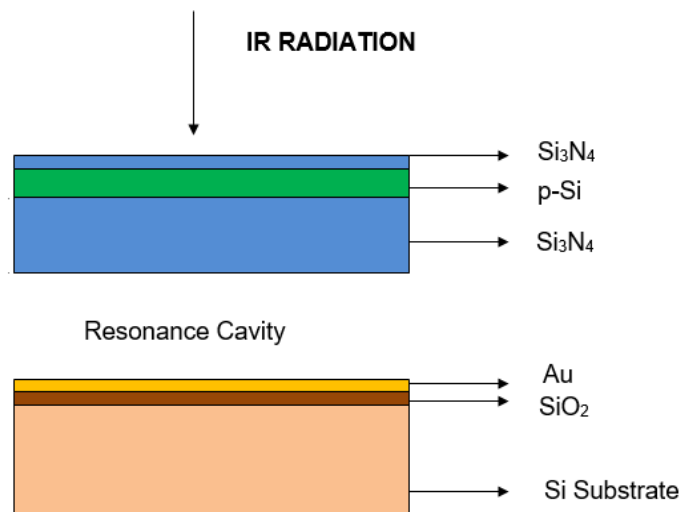

Figure 4.12 Cross-sectional schematic of proposed microbolometer multilayer structure.

In the top level structure, the upper Si_3N_4 layer, i.e. the passivation layer, is fixed at a thickness of 0.005 μm. The p-silicon layer is modeled with thickness of 0.097, 0.145 and 0.290 μm that correspond to a resistance value of 150, 100 and 50 Kilo-Ohm (KΩ), respectively. The top level (pixel) is a square-shaped multilayer; as a result, the resistance of the pixel is a function of the thickness of p-Si. The thickness of the lower Si_3N_4 absorber layer and the vacuum cavity are optimized

in order to achieve the highest infrared absorptance in the spectral range considered. In the bottom level structure, the thickness of the Au reflective layer is fixed at 0.1 μm to obtain the maximum possible reflectivity; the thickness of the SiO_2 is considered to be 0.005 μm and the silicon substrate thickness is considered to be 525 μm. The values of the thicknesses of various layers, considered in this study, are based on commercially available bolometer structures.

In order to understand and interpret the optical properties of the proposed microbolometer structure, the optical properties of each component layer has been considered in detail. This analysis will further facilitate to understand the required enhancement of the IR absorptance throughout the infrared spectral range (8-14 μm).

In the simulation studies presented here, the absorptance optimization of the proposed structure is divided in two parts. First, the study of the optical properties of the top level multilayer structure i.e. "free standing" in vacuum without the reflective effects of the bottom layers, as a function of the (lower) Si_3N_4 infrared absorber layer, is simulated as function of thickness. Second, the simulation of the optical properties of the entire multilayer structure, that consists of the top layers-vacuum cavity-bottom layers, as a function of thickness of vacuum cavity, is performed. The optimization procedure was implemented for each value of the p-Si thickness considered, in order to obtain the highest possible absorptance in each case.

Based on the above considerations, the total values of the optical properties, as a function of wavelength (8-14 μm), were simulated by Multi-Rad. In

Figures 4.13-4.15, the results of the simulated reflectance, transmittance and absorptance, as function of Si_3N_4 thickness for the top layer (free standing) of the proposed bolometer structure, are presented.

One of the important parameters that determines the performance of a microbolometer is a low heat capacity. In order to minimize the heat capacity, the thermal mass of the pixel (top level structure) must be reduced. In each case, the thickness of the Si_3N_4 IR radiation absorber layer is chosen to achieve the maximum absorptance, considering the effect of the Au reflective layer and the resonant cavity on top of the lower structure level, while keeping the absorber layer as thin as possible.

As can be seen in Figures 4.13 and 4.14, the optimum combination of optical properties corresponds to Si_3N_4 thickness of 2 μm and for the p-Si thickness of 0.097 μm and 0.145 μm. For the case with p-Si thickness of 0.290 μm (Figure 4.15), the optimum combination of optical properties corresponds to Si_3N_4 thickness of 1.5 μm.

After performing the optimization of the thickness of the top layers, the vacuum cavity depth is optimized to establish optical resonance and maximize the IR radiation absorption. The simulation of the optical properties of the two-level multilayer structure, that consists of the top layers-cavity-bottom layers, as a function of thickness of cavity, is performed and the results are plotted in Figures 4.16-4.18.

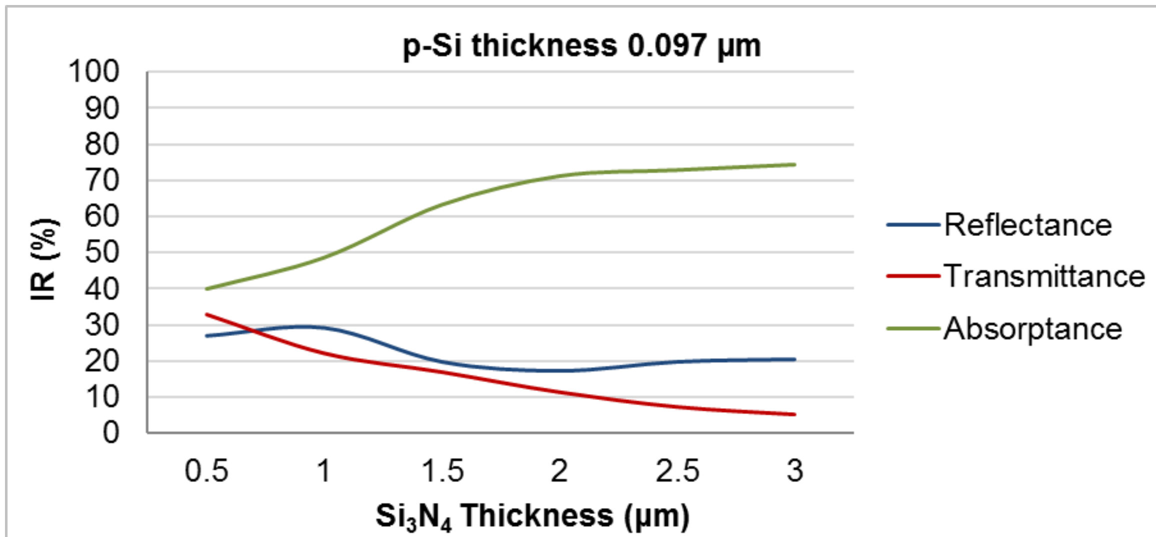

Figure 4.13 Simulated total reflectance, transmittance and absorptance as function of variable Si_3N_4 thickness for the top layer (free standing) of the proposed microbolometer structure (p-Si thickness=0.097 μm).

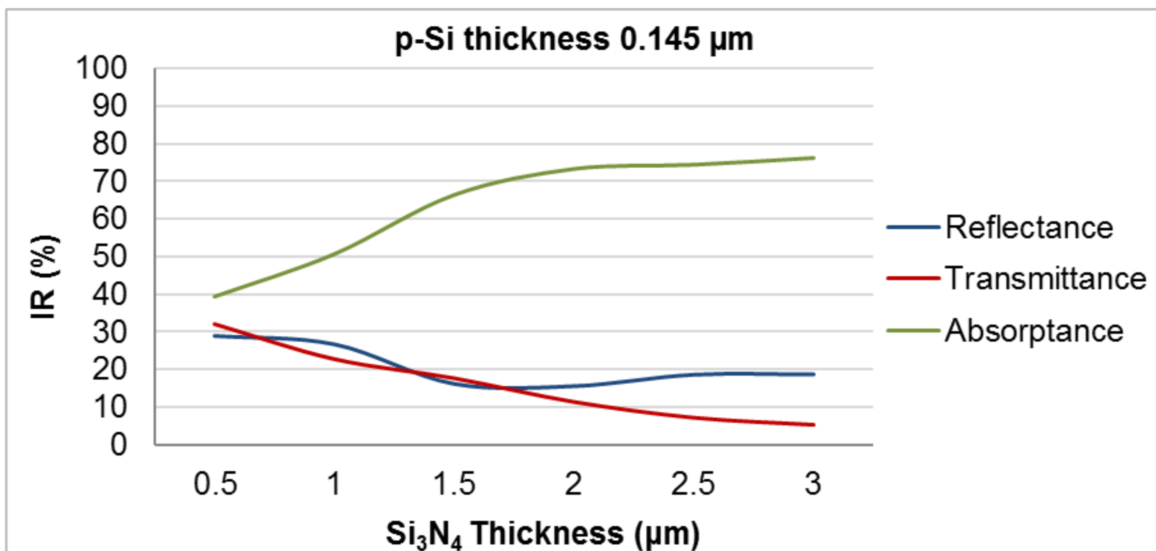

Figure 4.14 Simulated total reflectance, transmittance and absorptance as function of variable Si_3N_4 thickness for the top layer (free standing) of the proposed microbolometer structure (p-Si thickness=0.145 μm).

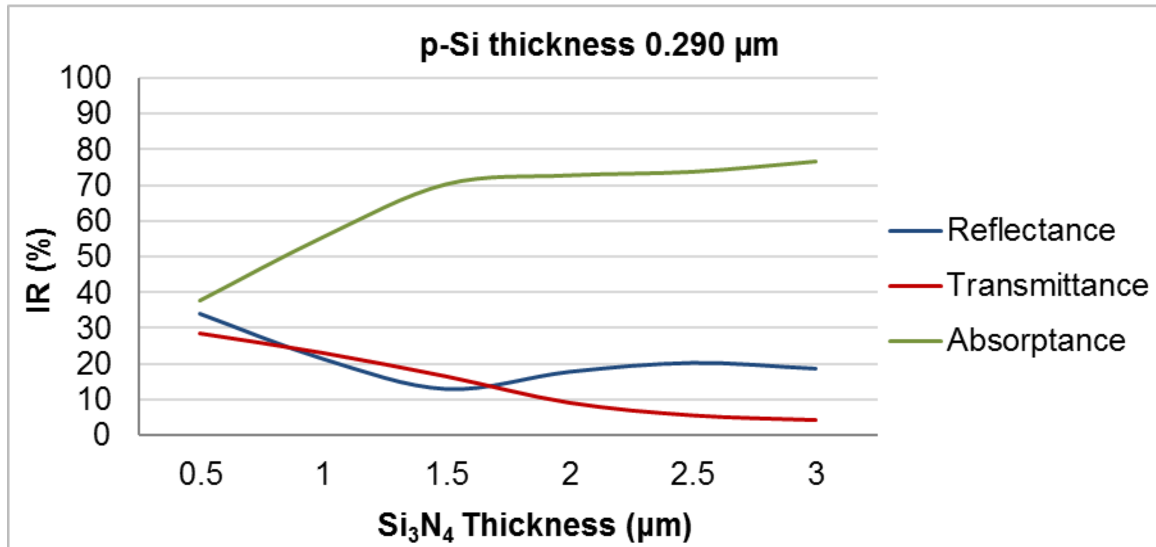

Figure 4.15 Simulated total reflectance, transmittance and absorptance as function of variable Si_3N_4 thickness for the top layer (free standing) of the proposed microbolometer structure (p-Si thickness=0.290 µm).

In Figures 4.16-4.18, the results of the simulated reflectance and absorptance, as function of cavity thickness for the proposed bolometer structure (two-level structure -Figure 4.12), are presented. The gold layer reflects the radiation transmitted by the top level multilayer structure with a negligible radiation transmitted through the lower multilayer. As can be seen in Figures 4.16-4.18, the maximum absorptance corresponds to cavity thickness of 2.0, 1.5 and 2.5 µm for p-Si thickness of 0.097, 0.145 and 0.290 µm, respectively.

The optimum resonant cavity thickness is not equal to $\lambda/4$ at the center of the operating wavelength range, because the two-level microbolometer structure consists of stacked multilayers with different thickness and complex refractive indices. These multilayers act together as a complex structure of cascaded Fabry-Perot (FP) optical resonators, and thus radiative modeling is the most accurate way to find optimum resonant cavity thickness. Each stacked multilayer has a specific transfer matrix function, which depends on the complex refractive indices, extinction coefficients, absorptions, reflections, and transmissions of the different thin film layers.

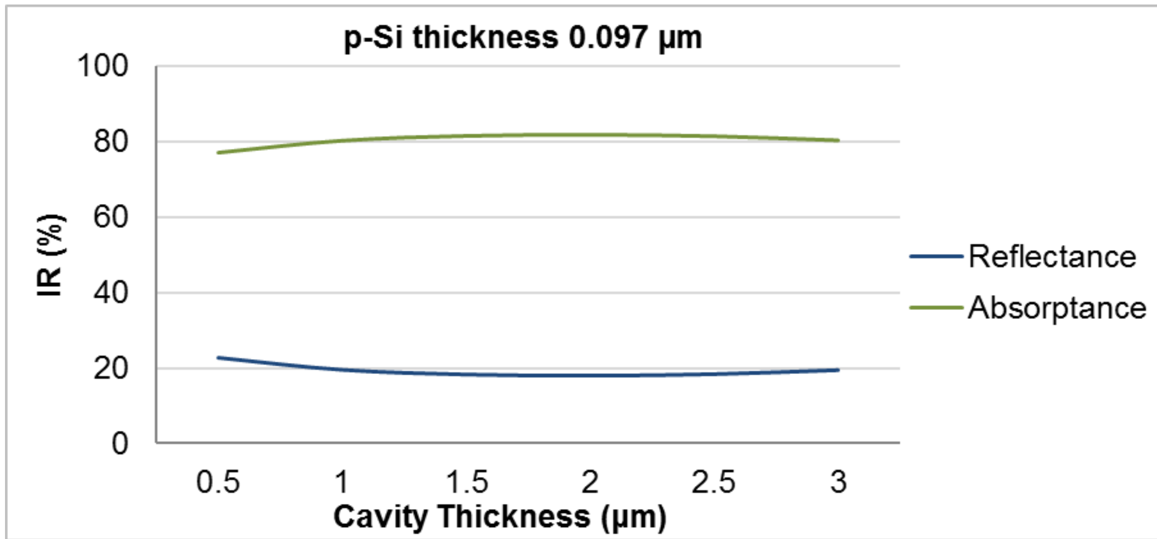

Figure 4.16 Simulated total reflectance and absorptance as function of cavity thickness for the proposed microbolometer structure (two-level structure) (p-Si thickness=0.097 µm).

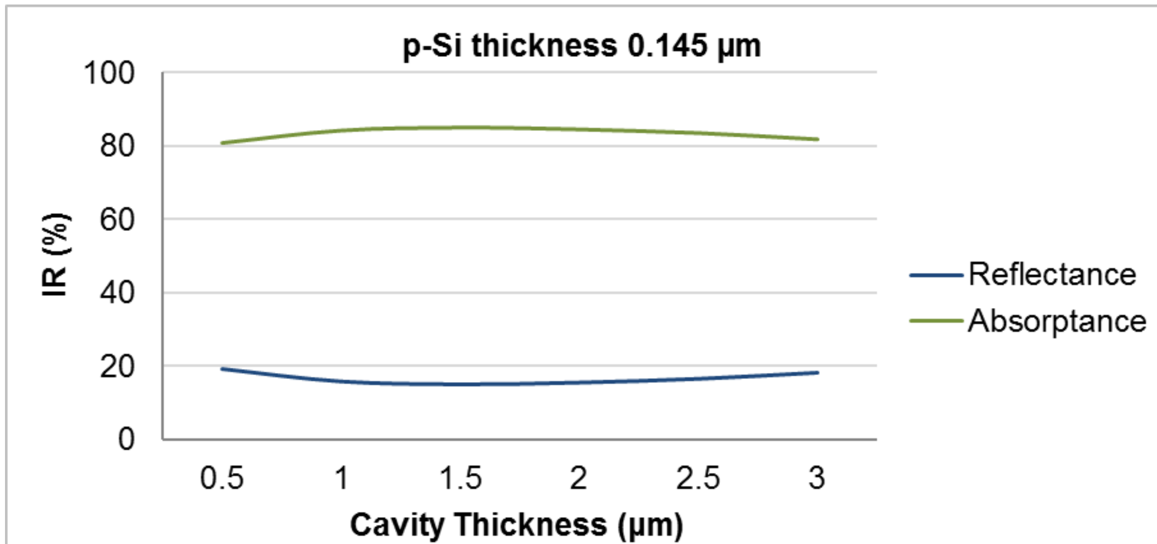

Figure 4.17 Simulated total reflectance and absorptance as function of cavity thickness for the proposed microbolometer structure (two-level structure) (p-Si thickness=0.145 µm).

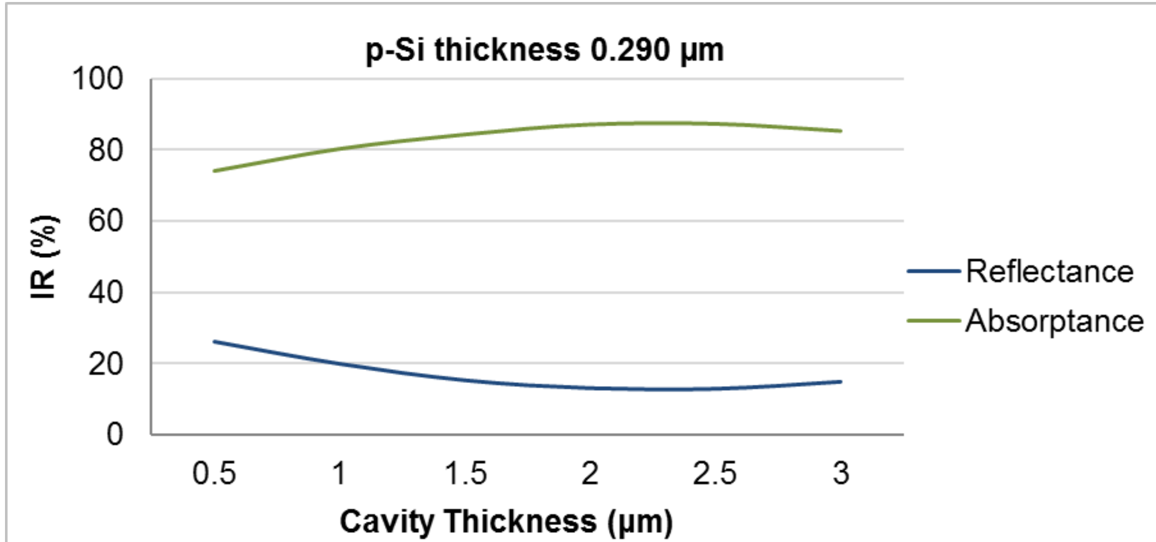

Figure 4.18 Simulated total reflectance and absorptance as function of cavity thickness for the proposed microbolometer structure (two-level structure) (p-Si thickness=0.290 µm).

Table 4.6 shows the optimized total IR radiation absorbed and reflected in the spectral range considered for the two-level multilayer structure for three fixed thickness of p-Si. The total absorptance is generally greater than 80% for the three different p-silicon thicknesses considered and the transmittance is negligible.

Table 4.6 Optical Properties of the Proposed Two-Level Multilayer Structure (Reflectance and absorptance total values)

p-Si Thickness(µm)	Si_3N_4 Thickness(µm)	Cavity Thickness(µm)	Reflectance (%)	Absorptance (%)
0.097	2.0	2.0	18.0	82.0
0.145	2.0	1.5	15.1	84.9
0.290	1.5	2.5	12.8	87.2

Figures 4.19-4.21 show the evolution of the radiative properties of the proposed two level multilayer structure for p-Si thickness (0.097, 0.145, 0.290 µm):

the top level free standing structure without the bottom level structure and with the optimized resonant cavity combined with the reflective gold layer deposited on top of the bottom level (substrate). As can be seen in Figures 4.19-4.21, the resonant cavity, in combination with the reflective gold layer, enhances the infrared radiation absorptance throughout the spectral range considered, reaching the highest absorptance peaks at 8.8 μm and 10.5 μm. It is in this atmospheric spectral region where objects register maximum infrared radiation emissivity (λ_{max}=9.66 μm) at room-temperature (300 K).

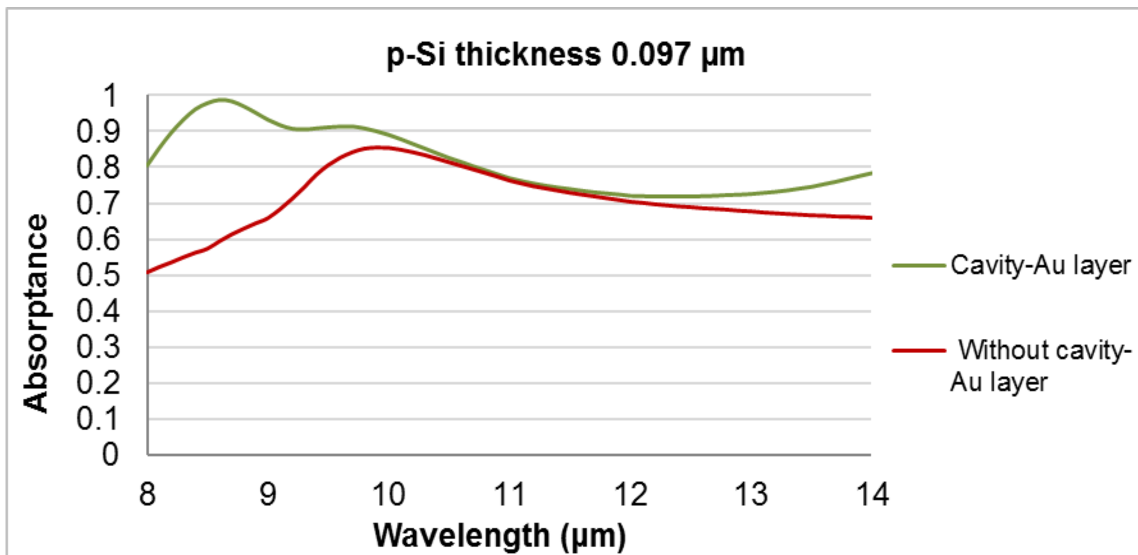

Figure 4.19 Evolution of simulated optical spectra of the proposed two-level multilayer with/without cavity-Au layer (p-Si thickness 0.097 μm).

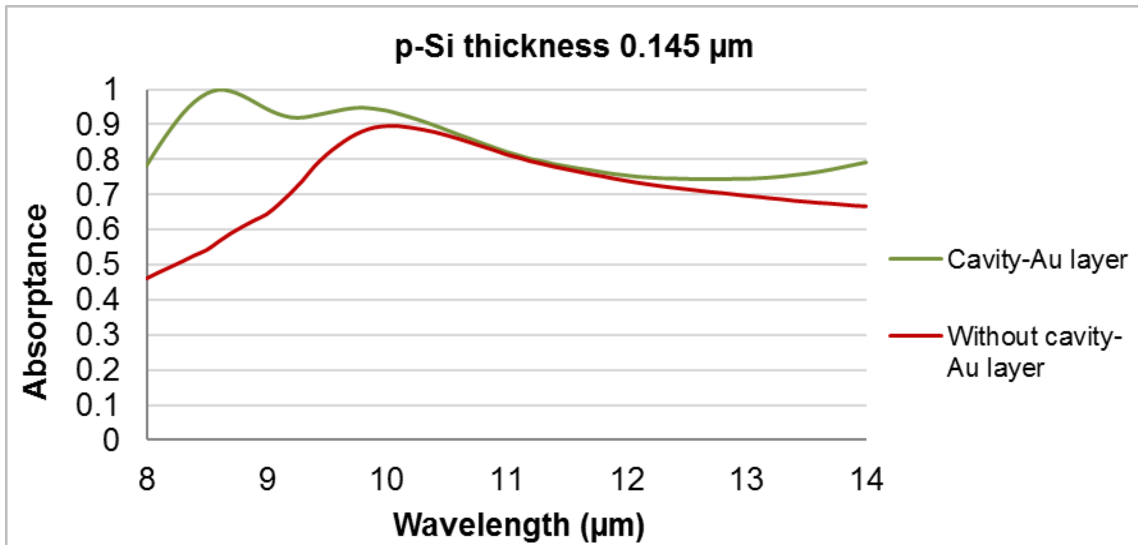

Figure 4.20 Evolution of simulated optical spectra of the proposed two-level multilayer with/without cavity-Au layer (p-Si thickness 0.145 µm).

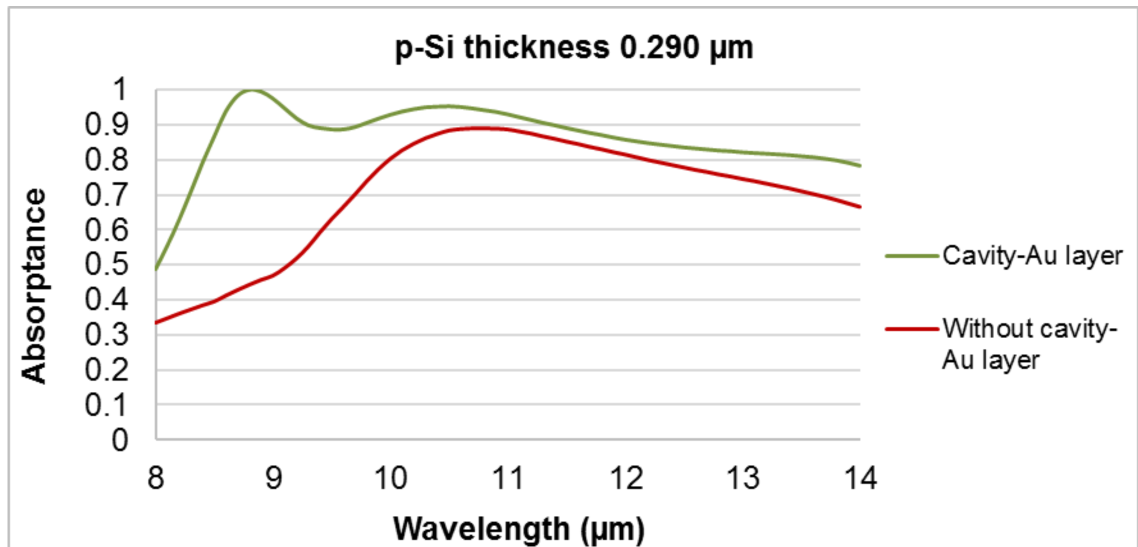

Figure 4.21 Evolution of simulated optical spectra of the proposed two-level multilayer with/without cavity-Au layer (p-Si thickness 0.290 µm).

The optimized resonant cavity, in combination with the IR reflective gold layer, enhances the total absorptance of the free standing multilayer to 15.28%,

15.83% and 19.72% for p-Si thickness of 0.097, 0.145 and 0.290 μm, respectively, as can be seen in Table 4.7.

Table 4.7 Enhancement of Absorptance with Cavity/Au Reflectance Layer

p-Si Thickness (μm)	Absorptance without cavity/Au layer (%)	Absorptance with cavity/Au layer (%)	Increment of absorptance (%)
0.097	71.13	82.0	15.28
0.145	73.3	84.9	15.83
0.290	72.9	87.2	19.72

Simulations of the optical properties for the two-level stacked structure of Si_3N_4/p-Si/Si_3N_4/Vacuum/Au/Si, in the considered spectral range, are presented in Figures 4.22-4.24, for different fixed thicknesses of p-Si (as in Table 4.7). In general, it can be observed that the optical spectra of the multilayer structure are in accord with the optical properties of Si_3N_4 in the long wavelength infrared, i.e. 8-14 μm; the absorptance is enhanced by the optimization of the resonant vacuum cavity thickness in combination with the Au reflective layer. The transmittance is negligible as a result of the reflectivity of the Au layer on top of the Si substrate layer. In summary, in each case, the peak in the absorptance for the proposed bolometer structure, in the spectral range of 9-11 μm, is due to the vibrations of the diatomic basis of silicon nitride, and the peak at 8.5 μm is a result of the optimization of the vacuum resonant cavity. The maximum absorptance is achieved for p-Si layer with thickness of 0.290 μm that corresponds to the lowest resistance value (50 kΩ).

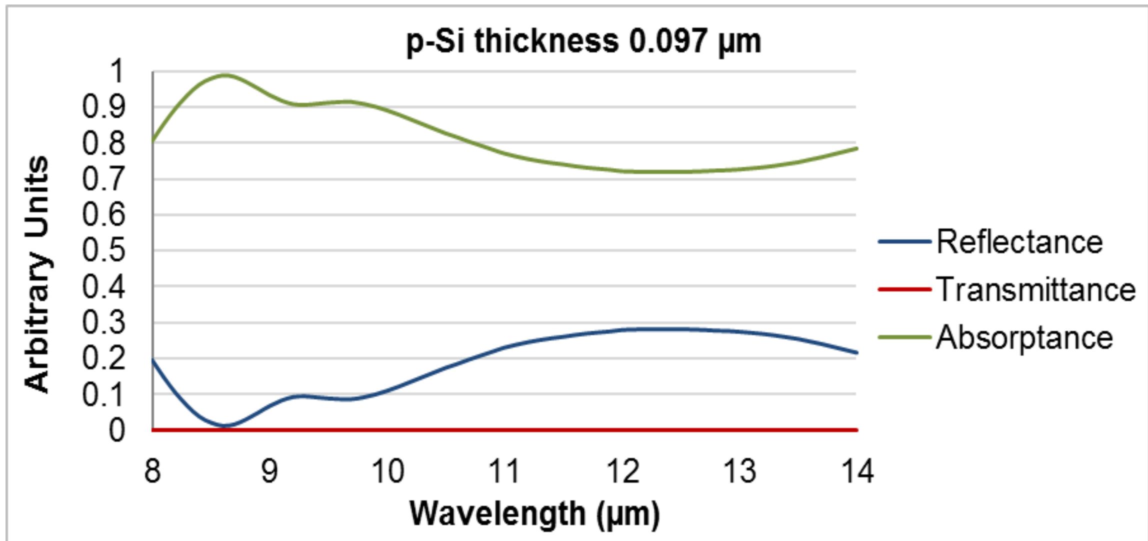

Figure 4.22 Simulated optical spectra of Si_3N_4/p-Si/Si_3N_4/Vacuum/Au/SiO_2/Si (p-Si thickness 0.097 µm).

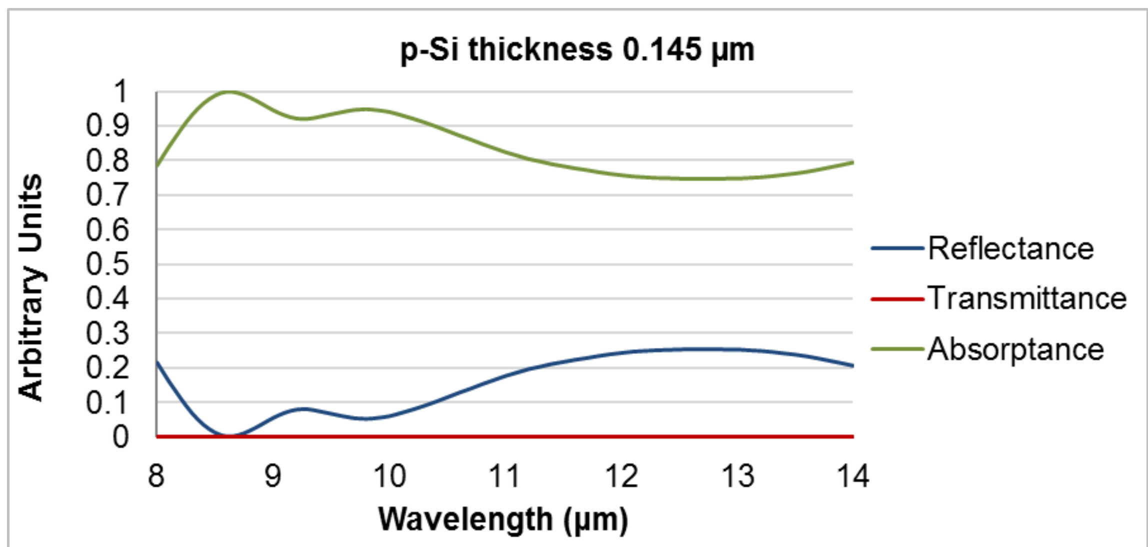

Figure 4.23 Simulated optical spectra of Si_3N_4/p-Si/Si_3N_4/Vacuum/Au/SiO_2/Si (p-Si thickness 0.145 µm).

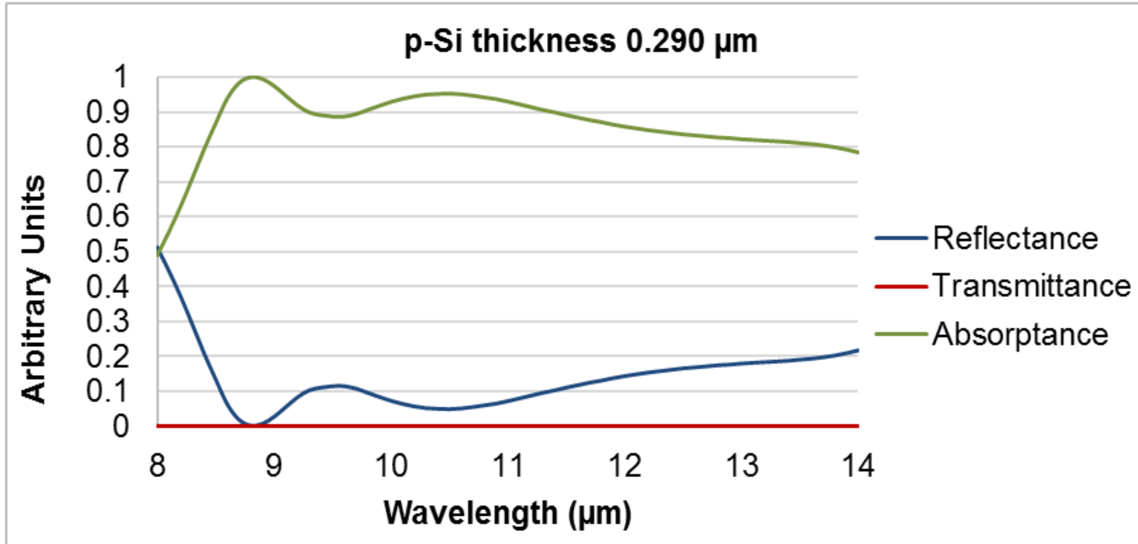

Figure 4.24 Simulated optical spectra of Si_3N_4/p-Si/Si_3N_4/Vacuum/Au/SiO_2/Si (p-Si thickness 0.290 µm).

4.5 Numerical Calculations of Microbolometer

Numerical calculations provide predictions of device performance based on the relationship between material properties and design geometry. The performance of microbolometers is determined by the properties (optical, electrical, mechanical and thermal) of the material used and the geometry and dimension of the structure.

In order to be used by the imaging industry in the fabrication of FPA, the size of the microbolometer IR absorption area (pixel) should be maximized in relation to the total area consumed by the microbolometer. The parameter that defines the portion of the microbolometer pixel area that is used to absorb the incident infrared radiation is defined as the fill factor. The fill factor is the ratio of the IR radiation absorber area to the total area of a single microbolometer (pixel). A high fill factor corresponds to a high efficiency of IR radiation energy absorption.

Standard infrared microbolometer arrays typically have a fill factor between 60 % and 70 % [111].

The infrared imaging industry requires detectors with high responsivity, low noise equivalent temperature difference and the capability to function at a high frame rate. This is only possible if thermal conductance and thermal capacitance are optimized. The thermal conductance and thermal capacitance are critical and a trade-off is required in the optimization of the microbolometer. Thermal capacitance is determined by the suspended multilayer structure and thermal conductance by the support arms to the substrate.

The performance of the microbolometer is dependent on thermal isolation. In order to maximize the thermal isolation, the thermal conductance through the support arms (heat link) between the pixel and the substrate is needed to be minimized. Thermal conductance depends on the thermal conductivity and geometry (dimensions) of the support arms. Reducing the cross sectional area and increasing the length of the arms decreases the thermal conductance. However, the stability of the thermally isolated support structure needs to be considered. At low frequencies, the detector responsivity is determined by the thermal conductance of the support arms. The thermal conductance is inversely proportional to the thermal time constant and to the responsivity of the detector. Therefore, an optimum geometry and dimensions of the support arms will allow to achieve the maximum responsivity that is possible with the thermal time constant required for imaging applications. The thermal conductance by conduction through

the considered heat links (arms) to the heat sink is the combination of three layers (Si_3N_4/Al/Si_3N_4).

The thermal capacitance is a function of thermal mass; in order to minimize the thermal capacitance, the thermal mass must be reduced. At high frequencies, the responsivity is determined by the thermal conductance and the modulation frequency of the radiation. The thermal capacitance of the top level multilayer considered is the combination of the three layers (Si_3N_4/p-Si/Si_3N_4).

The optical modeling of the radiative properties of the proposed multilayer structure clearly shows that the multilayer, with p-type Si thickness of 0.290 μm, achieves the highest total radiation absorptance (87.2 %) with the smaller thermal mass. This multilayer two-level structure is considered to be the optimum choice in the modeling of numerical calculations.

The dimensions and materials of the proposed microbolometer structure were determined in order to optimize the detector response for applications in infrared imaging. The proposed microbolometer (Figure 4.11) square-shaped multilayer (pixel) dimension is chosen to be 50x50 μm^2 that is consistent with commercial high-resolution imaging. The p-type Si thermosensing layer is encapsulated between two Si_3N_4 electrical insulation layers. Aluminum is used as interconnection between the p-type Si element and the ROICs on the substrate, due to its excellent Ohmic contact, low electrical resistivity and low noise contribution. The aluminum interconnection has a width of 4 μm and thickness of 0.1 μm; it is deposited over the lower layer of Si_3N_4 and the thermal sensing element of p-Si to ensure the Ohmic contact, as shown in Figure 4.25. Each

support arm has a length of 55 μm with an area of 8.05 μm^2 (width = 5 μm and thickness = 1.605 μm). The fill factor of the proposed device structure is 64.1 %. The ROIC circuit is placed under the microbolometer membrane to reduce the fill factor and increase the absorption area of an array of microbolometer elements to conform to a focal plane array for imaging systems, maximizing the efficiency of the incident radiation absorption. Figure 4.11, shows a schematic of the proposed microbolometer. Physical and thermal properties of the materials considered in the numerical calculations at 25 ^{o}C [112] are summarized in Table 4.8.

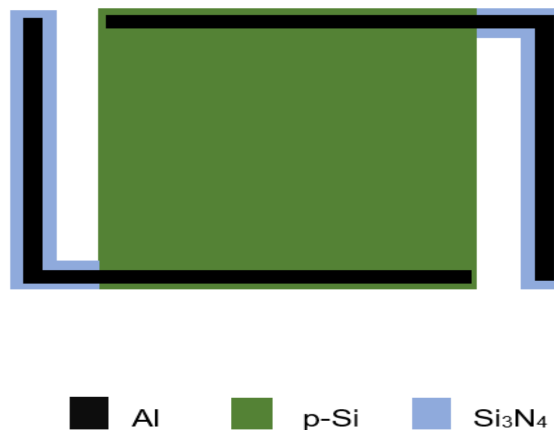

Figure 4.25 Top-view schematic of the proposed microbolometer multilayer structure (interconnection Ohmic contact).

Table 4.8 Physical and Thermal Properties of Materials Used in the Proposed Microbolometer [112]

Material	Al	Si_3N_4	p-Si
Specific heat capacity ($Jg^{-1}K^{-1}$)	0.900	0.733	0.704
Density (gcm^{-3})	2.7	3.1	2.3
Thermal conductivity ($Wm^{-1}K^{-1}$)	236	18.5	149

The proposed microbolometer figures of merit were calculated considering a blackbody radiation source in the infrared wavelength range of 8-14 μm, with an angular modulation frequency in the range of 0-10000 Hz.

The bias voltage applied to the voltage divider circuit is considered to be 2, 4 and 6 V, and the load resistor is chosen to match the microbolometer resistance; Therefore, the voltage applied to the microbolometer is half the voltage bias applied to the voltage divider circuit (1, 2 and 3 V). The microbolometer is considered to operate in a vacuum package to minimize the thermal conduction between the device and the surroundings; Consequently, no transmission losses are considered by convection from the microbolometer. Johnson noise is considered as the predominant source of noise because the thermosensing element is single crystal silicon.

Microbolometer parameters such as thermal conductance, thermal conductivity, thermal time constant, detector noise bandwidth and electrical noise depend exclusively on emissivity (or absorptance) of the multilayer stack; also, the device performance depends on the geometrical and thermal properties of the materials and are independent of the angular frequency of modulation of radiation. Table 4.9 shows the numerical results of these parameters for p-Si with varying thickness. The microbolometer figures of merit (responsivity, normalized detectivity and noise equivalent power) depend on the previously mentioned parameters and are function of the radiation modulation frequency and the applied bias voltage. Responsivity and noise values determine the microbolometer

performance, calculated in terms of NEP and D^*. Johnson noise is a function of noise bandwidth and the detector resistance, as can be seen in Table 4.9.

Table 4.9 Parameters of Proposed Microbolometer

p-Si thickness (μm)	0.097	0.145	0.290
Resistance R_{bol} (kΩ)	150	100	50
Thermal conductance G_e (WK^{-1})	1.001×10^{-5}	1.001×10^{-5}	8.357×10^{-6}
Thermal capacitance C_{th} (JK^{-1})	2.054×10^{-8}	2.054×10^{-8}	1.779×10^{-8}
Thermal time constant τ_e (ms)	2.052	2.052	2.129
Cut-off frequency f_c (Hz)	487	487	469
Noise bandwidth Δf (Hz)	77.543	77.546	74.754
Johnson noise V_j (V)	1.255×10^{-8}	1.300×10^{-8}	2.489×10^{-7}

4.5.1 Figures of Merit

Figures of merit were calculated for the proposed three two-level multilayer structures. The structure with p-Si thickness of 0.290 μm exhibits the highest values of R_v and D^*, and the lowest values of NEP throughout the IR source modulation frequency considered. Figures 4.26-4.28 show these figures of merit (p-Si thickness 0.290 μm) as function of modulation frequency of radiation source (0-1000 Hz) with a bias voltage applied to the microbolomer of 1, 2 and 3 volts.

As can be seen in Figures 4.26 and 4.28, R_v and D^* show a decreasing trend as function of IR source radiation modulation frequency. At the cut-off

frequency f_c (-3 dB frequency) of 469 Hz, the responsivity and normalized detectivity attain 70 % of their value when the IR source radiation modulation frequency is 0 Hz. It is evident that, at low frequencies, the detector responsivity is inversely proportional to the thermal conductance of the heat link; and at high frequencies, the detector responsivity is inversely proportional to the thermal capacitance and falls off inversely with the frequency of the optical signal. As can be seen in Figure 4.27, NEP increases linearly with modulation frequency of the IR source.

The responsivity and normalized detectivity can be enhanced by increasing the bias voltage, but it will also increase the Joule heating. The normalized detectivity achieves values of 10^8 which is comparable to many commercial devices.

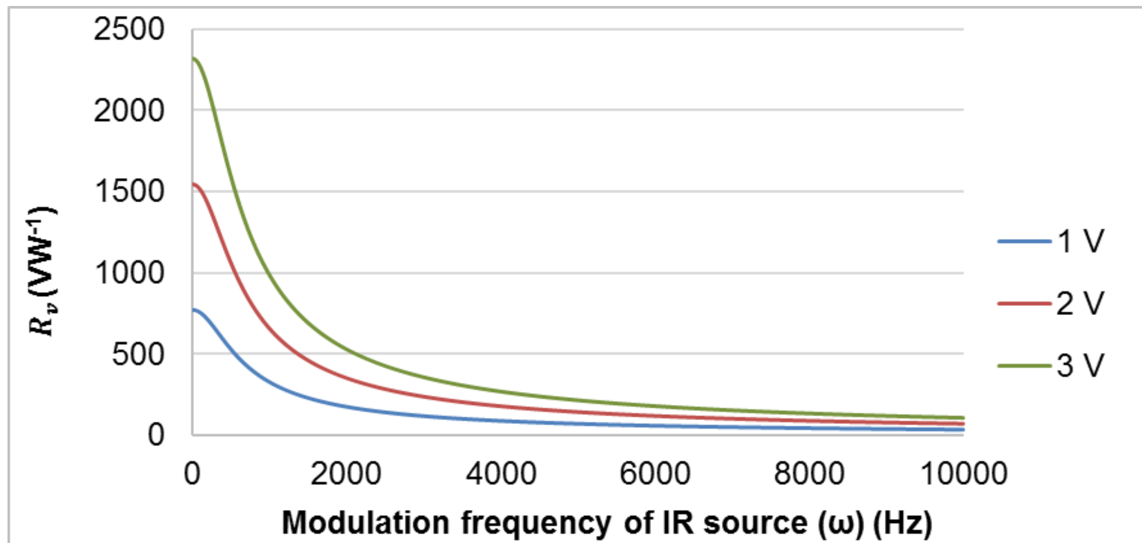

Figure 4.26 Calculated R_v as function of applied bias voltage and modulation frequency ω of IR source (p-Si thickness 0.290 μm).

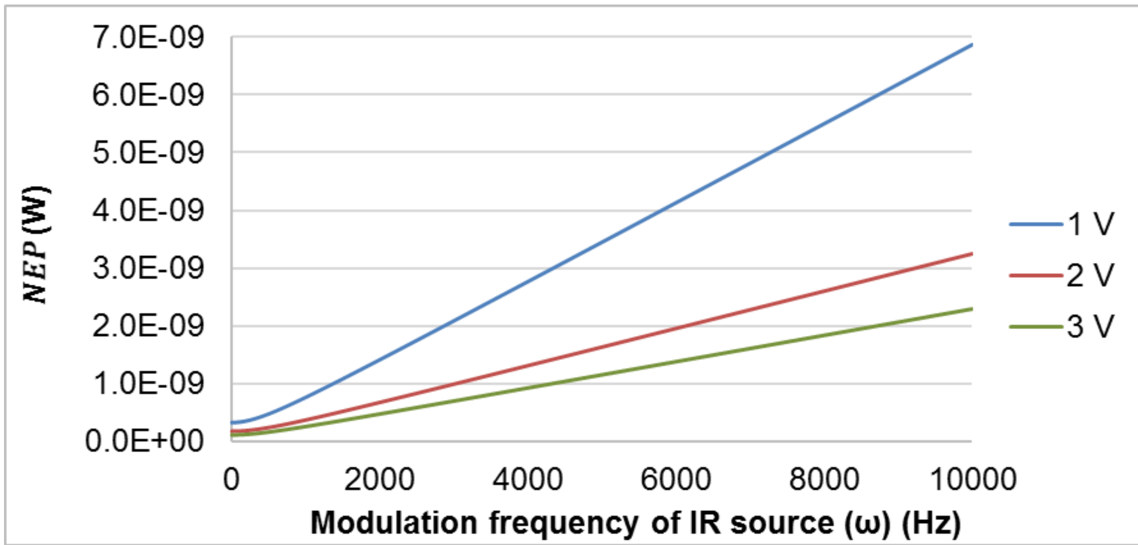

Figure 4.27 Calculated NEP as function of applied bias voltage and modulation frequency ω of IR source (p-Si thickness 0.290 μm).

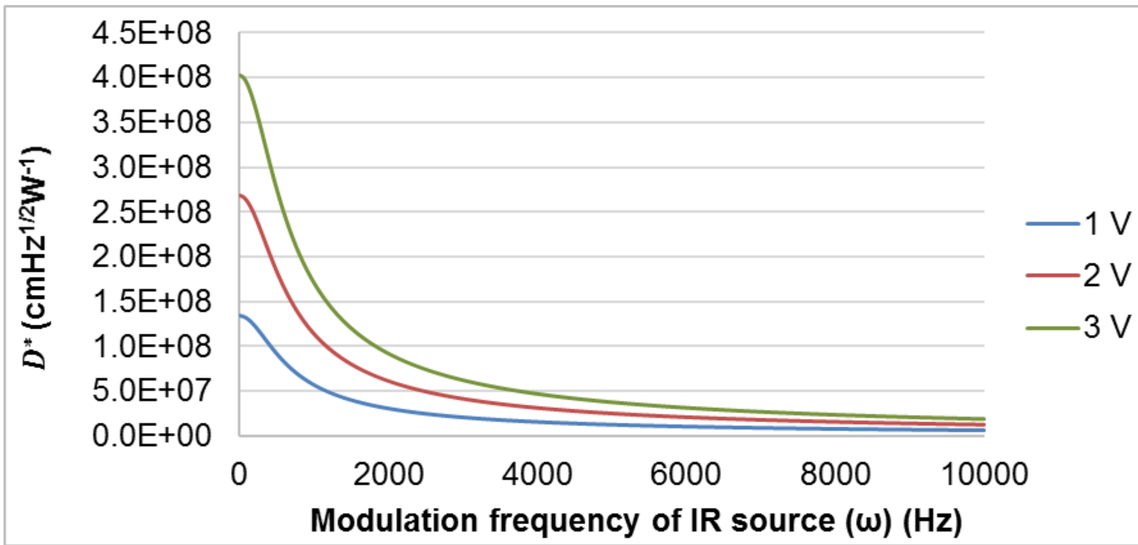

Figure 4.28 Calculated D^* as function of applied bias voltage and modulation frequency ω of IR source (p-Si thickness 0.290 μm).

4.5.2 $NETD$ of Microbolometer

In the numerical calculation of $NETD$, the IR source is considered to be a blackbody source. The transmittance of the optics system τ_0 is considered to be 0.9 (Ge lens); and the atmospheric transmittance τ_a is considered to be lossless. Germanium is commonly used as IR filter, with a radiation transmittance of 0.9 over the wavelength range considered of 8-14 μm. The focal number of the optical detection system $^f/_\#$, is considered to be 1, 2 and 3 that correspond to optics lenses diameters of equal, half and one-third of the focal length, respectively. The imaging system is shown in Figure 2.4 (Schematic diagram of optical system).

Figures 4.29-4.31 show the $NETD$ (p-Si thickness 0.290 μm) as function of source radiation modulation frequency and applied bias voltage to the microbolometer for focal number equal to 1, 2 and 3 of the optical detection imaging system.

The results of $NETD$ show that for practical applications, the proposed two-level structures, with p-silicon thickness 0.097 and 0.145 μm, could be used as IR radiation detectors. Nevertheless, they do not represent the requirements of the imaging industry that requires $NETD$ to be lower than 100 mK.

As is evident in Figures 4.29-4.31, the microbolometer with thickness of p-Si of 0.290 μm exhibits an $NETD$ of less than 100 mK, for a voltage bias of 3 V, $^f/_\#$=1, and for a source modulation frequency of 469 Hz. The thermal time constant of 2.129 ms allows the imaging system to operate at a standard frame rate in the range of 9-157 Hz.

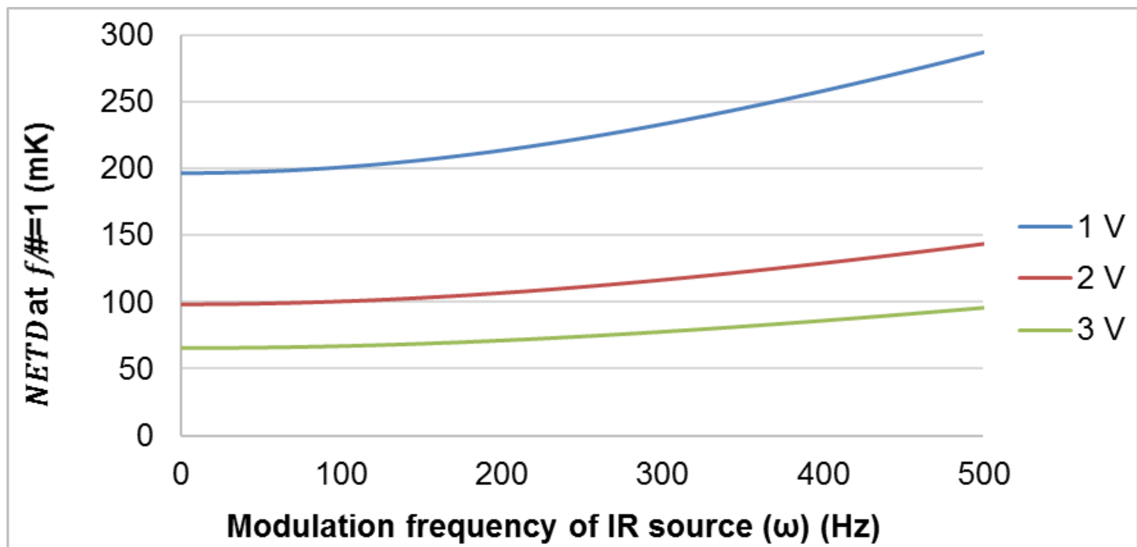

Figure 4.29 Calculated $NETD$ as function of applied bias voltage and modulation frequency ω of IR source at $^{f}/_{\#}$=1 (p-Si thickness 0.290 μm).

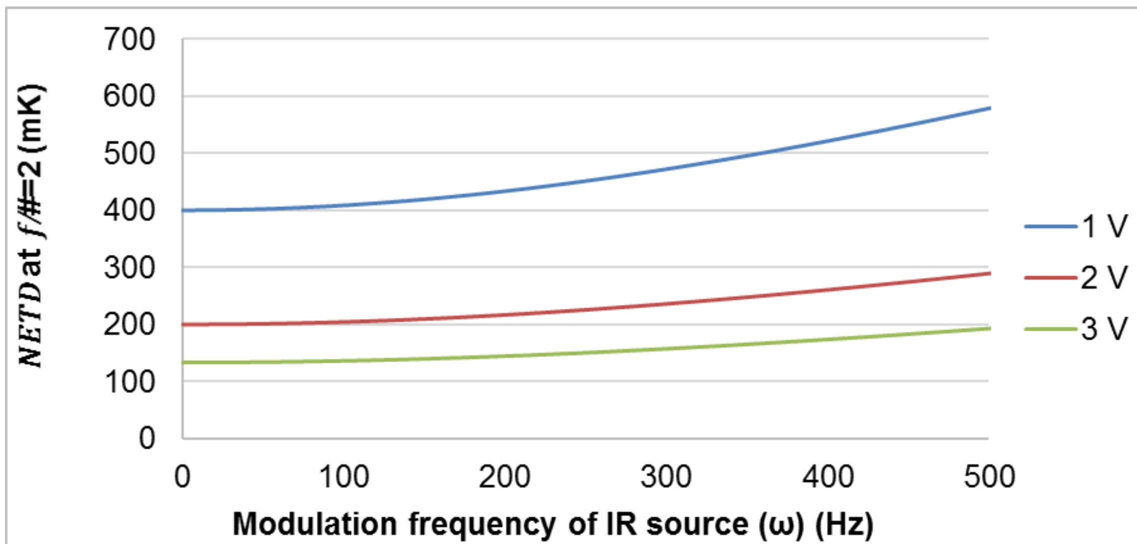

Figure 4.30 Calculated $NETD$ as function of applied bias voltage and modulation frequency ω of IR source at $^{f}/_{\#}$=2 (p-Si thickness 0.290 μm).

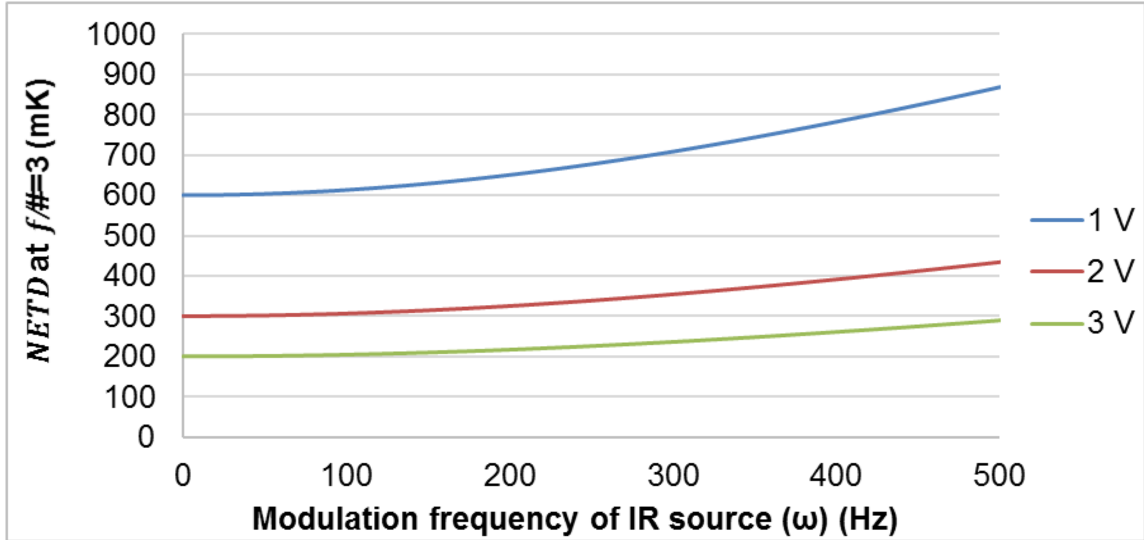

Figure 4.31 Calculated $NETD$ as function of applied bias voltage and modulation frequency ω of IR source at $^{f}/_{\#}$=3 (p-Si thickness 0.290 μm).

4.6 Numerical Calculations of Improved Microbolometer

In order to achieve $NETD$ values lower than 100 mK, some of the proposed parameters of the two-level structure must be modified. Equation 2.37 defines $NETD$, and to reduce its value, the D^* of the detector must be increased. D^* is proportional to R_v, as can be seen from Equations 2.34 and 2.35. The thermal capacitance C_{th} was optimized and fixed; therefore, G_{cond} is the parameter to be modified in order to reduce the $NETD$. By increasing the length of the support arms to the heat sink, the thermal conductance by conduction will decrease as can be seen from Equation 2.5, increasing the responsivity and as a final result, decreasing $NETD$.

To reduce $NETD$, the proposed two-level structure was modified, considering doubling the lengths of the arms to 110 μm, while the rest of the geometrical parameters were kept unchanged. The fill factor of this modified

structure is 51.0 %. Figure 4.32 shows the schematic of the improved two-level microbolometer thin film layer structure. The new microbolometer parameters, for each p-Si thickness considered, are numerically calculated and are summarized in Table 4.10. The thermal time response is less than 5 ms for the three p-Si varying thickness, allowing them to be used by imaging system that operates at frame rates in the range of 9-80 Hz. Comparing Tables 4.9 and 4.10, we can see how G_e and Δf decrease with increment in the length of the arms, while τ_e increased.

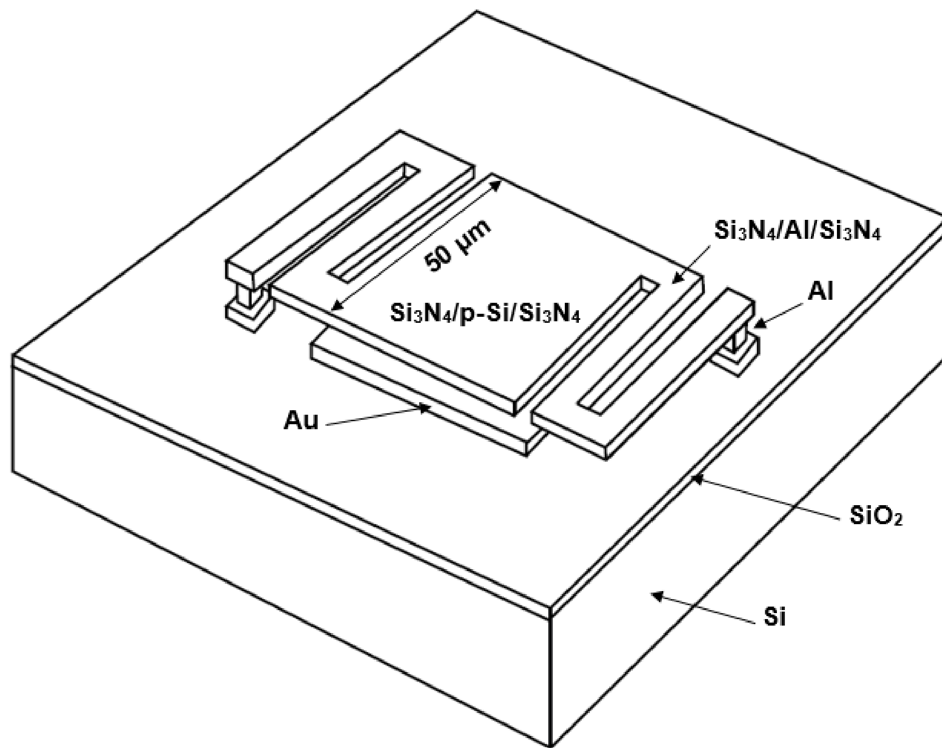

Figure 4.32 Schematic of improved proposed microbolometer (Two-level 50 x 50 µm^2).

Table 4.10 Parameters of Modified Proposed Microbolometer

p-Si thickness (µm)	0.097	0.145	0.290
Resistance R_{bol} (kΩ)	150	100	50
Thermal conductance G_e (WK^{-1})	$5.101x10^{-6}$	$5.101x10^{-6}$	$4.261x10^{-6}$
Thermal capacitance C_{th} (JK^{-1})	$2.054x10^{-8}$	$2.054x10^{-8}$	$1.779x10^{-8}$
Thermal time constant τ_e (ms)	4.027	4.026	4.176
Cut-off frequency f_c (Hz)	248	248	239
Noise bandwidth Δf (Hz)	39.53	39.53	38.12
Johnson noise V_j (V)	$3.134x10^{-7}$	$2.559x10^{-7}$	$1.777x10^{-7}$

4.6.1 Figures of Merit of Improved Microbolometer

Figures of merit calculation for the modified structure show increase in R_v and D^*, with a decrease in NEP; which is a significant improvement over the original proposed structure. The small increase in τ_e still allows the microbolometer to operate at frame rates in the standard range of commercial imaging systems. The changes in the figures of merit are a direct result of the increase in G_e.

Figures of merit were calculated for the proposed three two-level multilayer structures. The structure with p-Si thickness of 0.290 µm results in the highest values of R_v and $D^*,$ and with the lowest values of NEP. Figures 4.33- 4.35 show these figures of merit as function of modulation frequency of radiation source (0-10000 Hz) with a bias voltage applied to the microbolomer of 1, 2 and 3 volts for the modified microbolometer with p-Si thickness of 0.290 µm.

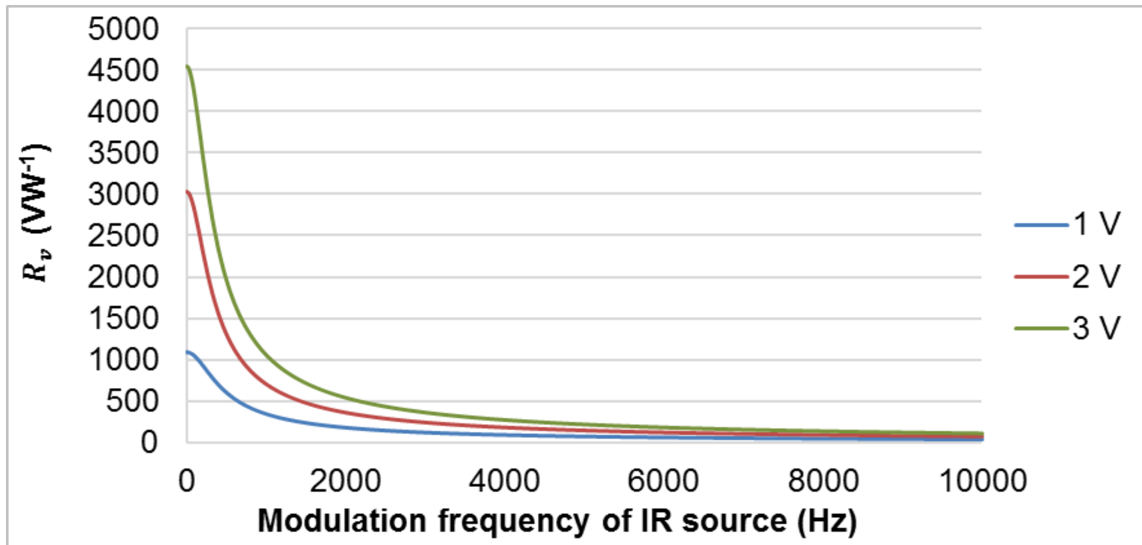

Figure 4.33 Calculated R_v as function of applied bias voltage and modulation frequency ω of IR source (p-Si thickness= 0.290 μm).

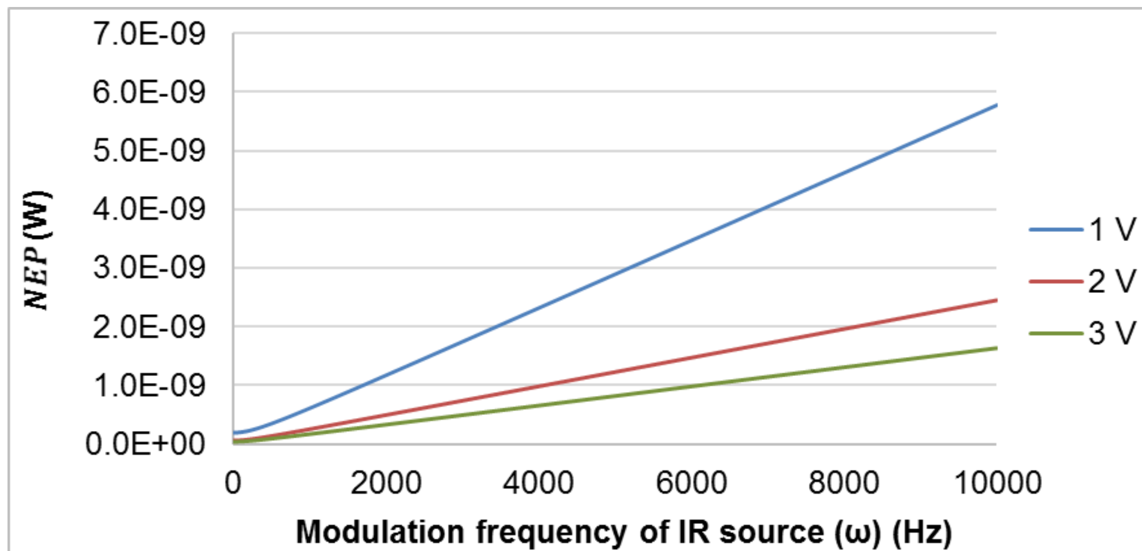

Figure 4.34 Calculated NEP as function of applied bias voltage and modulation frequency ω of IR source (p-Si thickness= 0.290 μm).

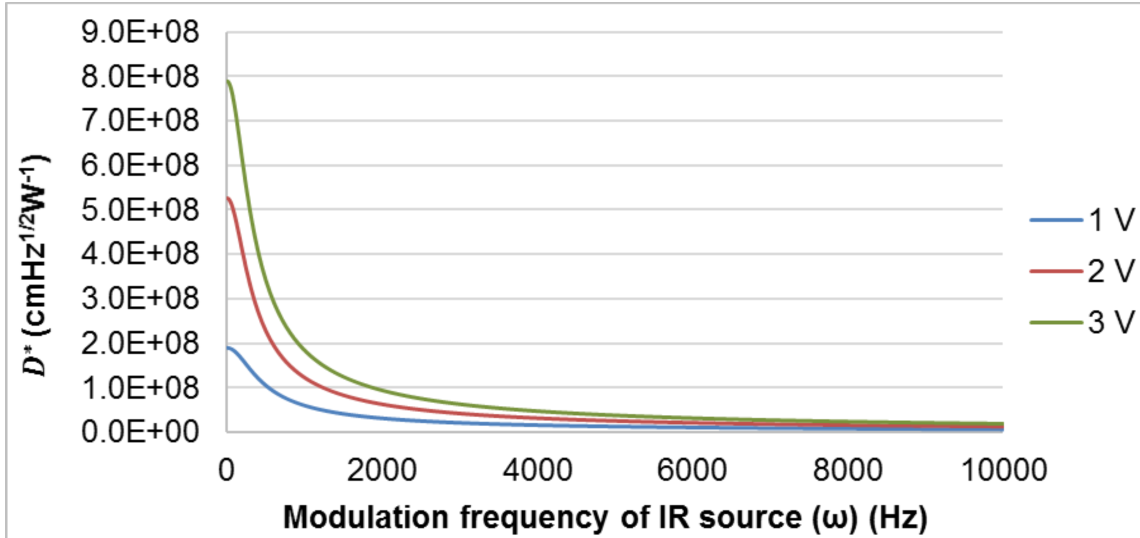

Figure 4.35 Calculated D^* as function of applied bias voltage and modulation frequency ω of IR source (p-Si thickness= 0.290 μm).

4.6.2 $NETD$ of Improved Microbolometer

Figures 4.36-4.38, show the $NETD$ for the improved microbolometer with p-Si thickness= 0.290 μm, as function of modulation frequency of IR source and applied bias voltage to the microbolometer for focal number equal to 1, 2 and 3 .

The $NETD$ results from Figure 4.36 show that at $^f/_\#$=1 and at all bias voltages considered, the $NETD$ is lower than 100 mK for sources with modulation frequencies under 239 Hz. Figure 4.37 shows that at $^f/_\#$=2 and at bias voltages of 2 and 3 V, the $NETD$ is lower than 100 mK for sources with modulation frequencies under 239 Hz. Figure 4.38 shows that at $^f/_\#$=3 and at bias voltages of 3, the $NETD$ is lower than 100 mK for sources with modulation frequencies under 239 Hz.

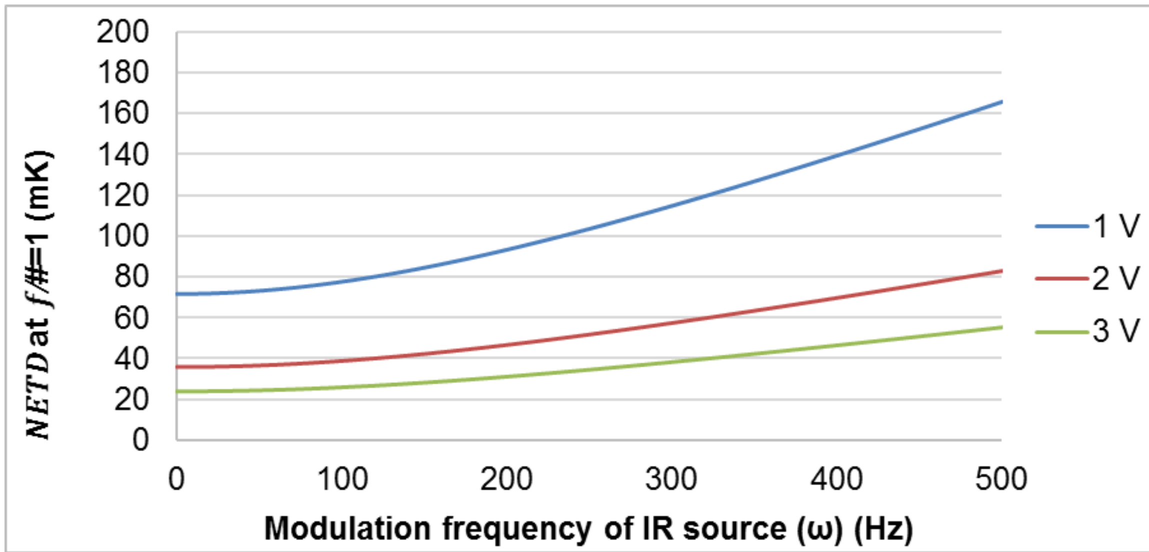

Figure 4.36 Calculated $NETD$ as function of applied bias voltage and modulation frequency ω of IR source at $f/_{\#}$=1 (p-Si thickness 0.290 μm).

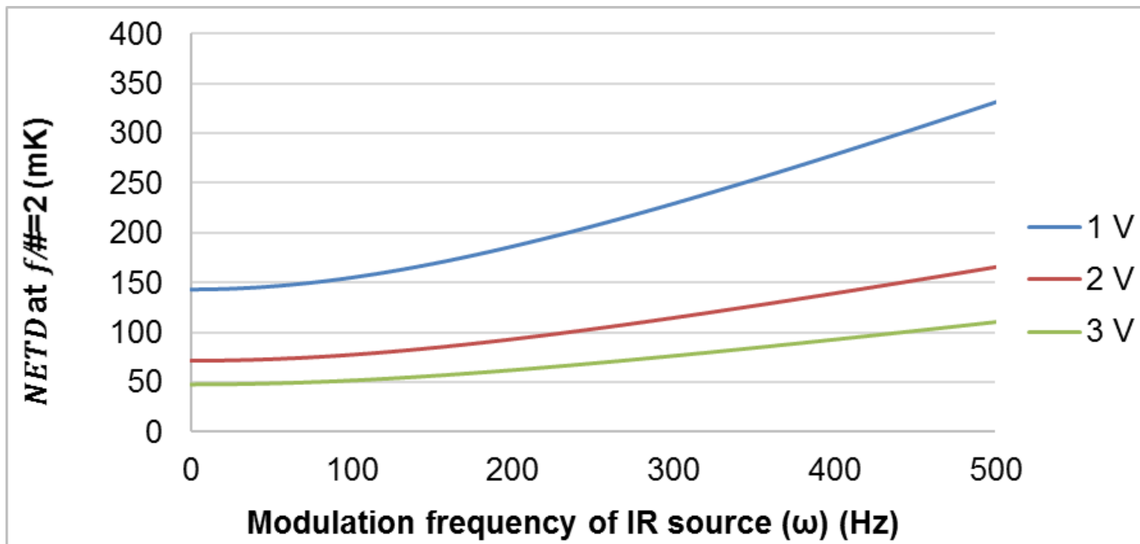

Figure 4.37 Calculated $NETD$ as function of applied bias voltage and modulation frequency ω of IR source at $f/_{\#}$=2 (p-Si thickness 0.290 μm).

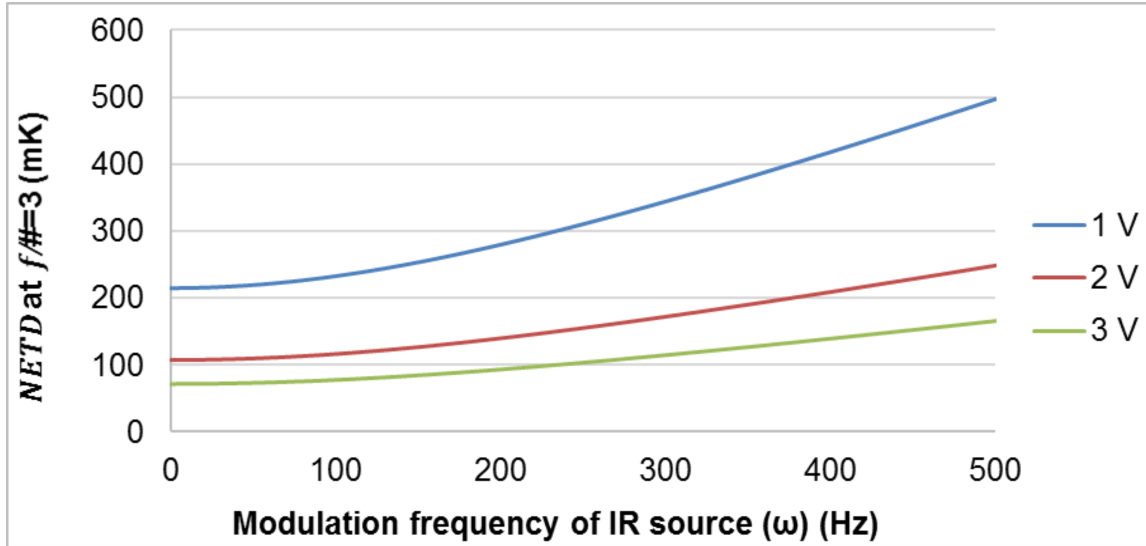

Figure 4.38 Calculated $NETD$ as function of applied bias voltage and modulation frequency ω of IR source at $^f/_{\#}$=3 (p-Si thickness 0.290 μm).

4.6.3 Summary

The initial proposed microbolometer structure does not achieve the $NETD$ values required by the imaging industry. Therefore, in order to meet the standard performance parameters of the IR imaging industry, the initial proposed microbolometer structure had to be modified. Increasing the length of the support arms of the microbolometer increases the thermal conductance. This results in an increase in the responsivity and the normalized detectivity, while the thermal response time increases to 96 %. The noise equivalent power decreases as the modulation frequency of IR source increases.

There is a significant improvement in the figures of merit and the performance of the modified proposed microbolometer with respect to the initial microbolometer structure proposed, while the fill factor decreases from 64.1 % to 51.0 %.

The noise equivalent temperature difference results show that the modified microbolometer structure, with twice the length of the arms, meets the requirements of the standard imaging industry, achieving values lower than 50 mK at $f/_{\#}$=1 in comparison with the initial structure that achieves higher values at the same focal number and applied bias voltage. The thermal time constant increases from 2.129 ms to 4.176 ms; this allows the imaging system to operate at a standard range of 9-80 Hz. The increase in the thermal time constant decreases the cut-off frequency from 469 Hz to 239 Hz.

CHAPTER 5

MICROBOLOMETER FABRICATION PROCESS

5.1 Method of Microbolometer Fabrication

The most common manufacturing approach for microbolometers is monolithic integration [113-115]. Monolithic integration process is a cost-efficient and well-established post CMOS process in which the read-out integrated circuit (ROIC) can be efficiently placed underneath the microbolometer suspended membrane. This is in contrast to the bulk-micromachining manufacturing method in which the ROIC is placed besides the microbolometer, reducing the fill factor [116]. In the monolithic integration microfabrication process, the ROIC is pre-manufactured and the microbolometer material layers are subsequently deposited and patterned on top of the substrate wafer. A stable high-temperature material is used as the sacrificial layer. In the final step of the microfabrication process, the sacrificial layer is removed in an oxygen plasma to obtain the free-standing, thermally isolated microbolometer two-level structure [117].

The proposed microbolometer is fabricated using standard microfabrication techniques. The substrate considered is an industrial standard silicon wafer with a diameter of four inches and thickness of 525 μm.

A method of fabrication of the two-level suspended IR microbolometer is described in detail. The fabrication approach considered is monolithic integration, in which thin film layers are deposited and patterned; this process is cost effective and is an established post CMOS process. The design and fabrication of this

device has six photolithography steps (photomask) throughout the fabrication process. The layers may be patterned by various photolithography and etching techniques.

The fabrication process is shown in Figure 5.1 (Process flow of two-level micro-bolometer). Figure 5.1 shows the fabrication process (cross- section view) for the initial proposed microbolometer structure and this process flow can be used in the fabrication of the modified microbolometer structure with twice the length of the arms. The fabrication method starts with the deposition of a thin dielectric layer over a single side polished silicon wafer (substrate), that acts as a dielectric insulator between the substrate, the reflective gold layer and the ROIC metal pad. The thin dielectric layer may include SiO_2 or Si_3N_4, and may be deposited by thermal oxidation, chemical vapor deposition (CVD), or physical vapor deposition (PVD) techniques. An IR radiation reflective layer of gold (Au) and the ROIC are deposited over the dielectric layer. They are deposited by sputtering, chemical vapor deposition (CVD), or physical vapor deposition (PVD) techniques. The ROIC metal pad materials may be Au, Al, NiCr, or Pt. The use of two masks, to define and transfer the IR radiation reflective gold layer and the ROIC, is required in this first fabrication step (Figure 5.1a).

In the next step of the fabrication method, a sacrificial layer is deposited over the lower level structure, with a thickness corresponding to the gap resonant-cavity required. The sacrificial layer may be comprised of various materials such as polyimide, or photoresist; and may be formed by suitable deposition techniques,

such as spin coating, chemical vapor deposition (CVD), or physical vapor deposition (PVD) techniques (Figure 5.1b).

After the sacrificial layer is deposited over the lower level structure, an IR radiation absorber layer of Si_3N_4 is deposited on top of the sacrificial layer through a low pressure chemical vapor deposition (LPCVD), to achieve the low residual stress thin film required by the suspended micro-bridge (Figure 5.1c).

The p-Si thermosensing layer is deposited on top of the Si_3N_4 absorber layer by plasma enhanced chemical vapor deposition (PECVD) technique using 10% SiH_4 and 90% Ar as precursor, with B_2H_6 (diborane) as p-type doping gas. The use of a mask to pattern and transfer the thermosensing structure is required in this fabrication step (Figure 5.1d).

Next, a plurality of cavities via holes is defined on the sacrificial layer, and etched to deposit the pillars that electrically couple the p-Si thermosensing material and the ROIC metal pad. The plurality of cavities (holes), defined to deposit the pillars that anchor the upper level to the lower level structure, are etched by reactive-ion etching (RIE) technique to achieve the anisotropic etch required. The pillars may be comprised of electrically conducting materials such as Al, Au, Pt, or NiCr; that may be deposited by sputtering or chemical vapor deposition (CVD) techniques. The use of a mask to define the cavities to deposit the pillars is required in this fabrication step (Figure 5.1e).

Subsequently, an interconnection layer is deposited over the thermosensing material and the arms to connect the thermosensing element and the pillars. The interconnection, Al, is formed by sputtering or chemical vapor

deposition (CVD) techniques. Al forms an Ohmic contact to the low doped p-type Si thermosensing layer, without the necessity of an additional high doped layer of p-type Si. The use of a mask to pattern and transfer the interconnection layer is required in this fabrication step (Figure 5.1f).

In a subsequent step, a top Si_3N_4 thin dielectric layer for passivation is deposited on top of the upper level structure, by low pressure chemical vapor deposition (LPCVD) or plasma enhanced chemical vapor deposition (PECVD) techniques (Figure 5.1g).

Next, the upper structure to form the arms and the suspended final upper structure of the bolometer is patterned and etched. The patterned structure may be etched by ion milling or reactive-ion enhanced (RIE) etching techniques to achieve the anisotropic etch required to achieve the suspended square-shaped microstructure. The use of a mask to pattern the upper structure to form the arms and the suspended final upper structure of the bolometer is required in this fabrication step (Figure 5.1h).

After the suspended micro-bridge is patterned and etched, the wafer (substrate) is diced to form individual microbolometer devices or microbolometer array. The individual microbolometer device or microbolometer array is processed by removing the sacrificial layer, forming the cavity by removing the sacrificial layer by plasma O_2/CF_4 etching process, or chemical wet etch (Figure 5.1i).

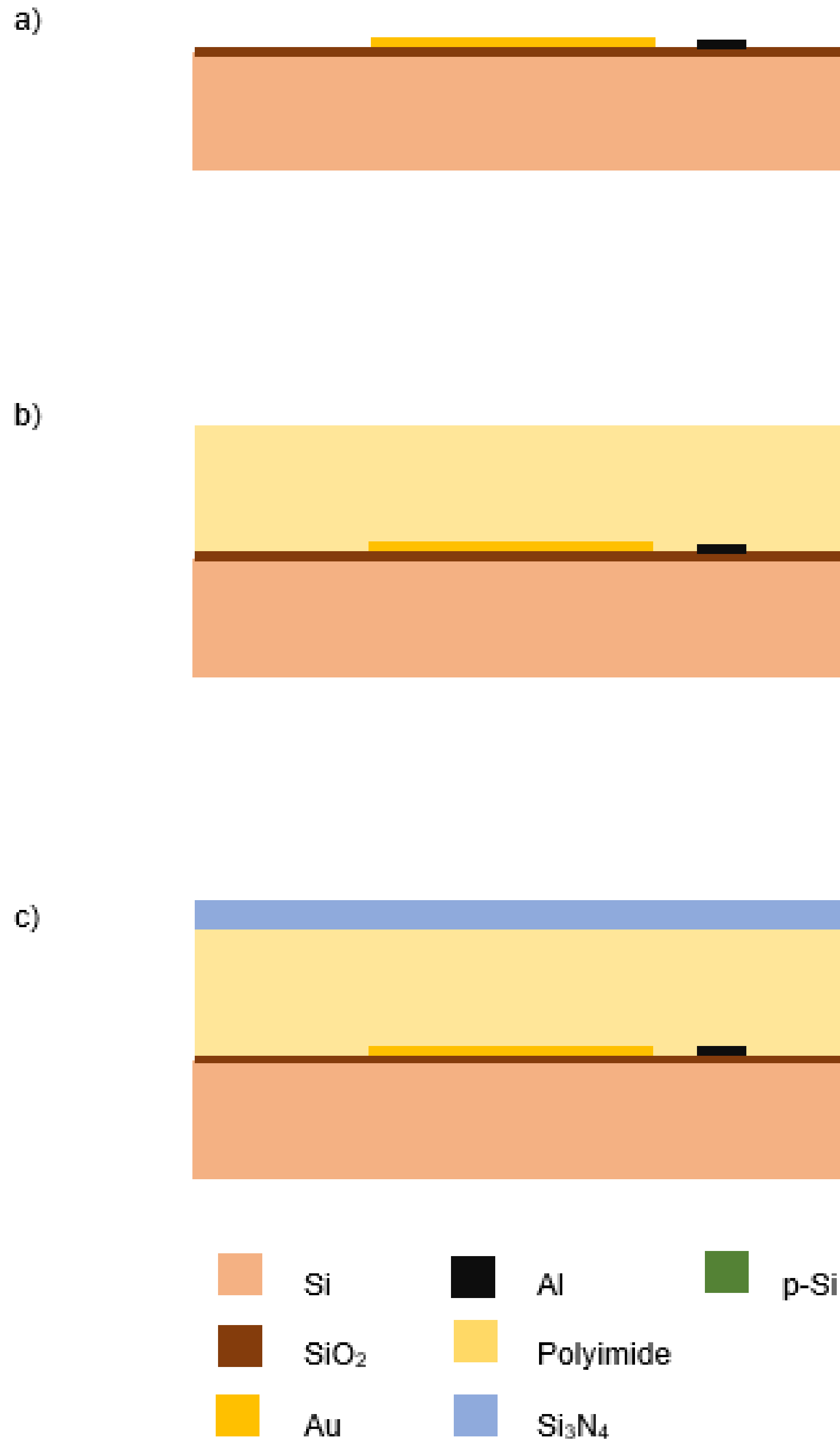

Figure 5.1 Fabrication process flow of two-level microbolometer (cross-section view). (Continued)

d)

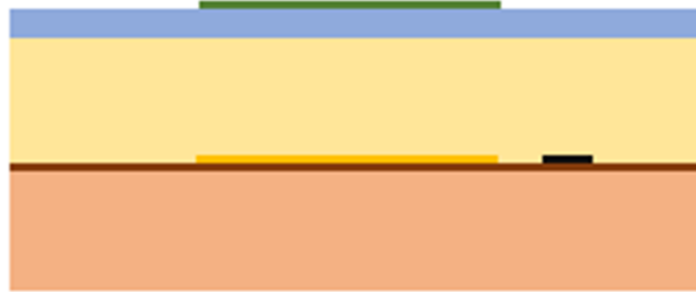

e)

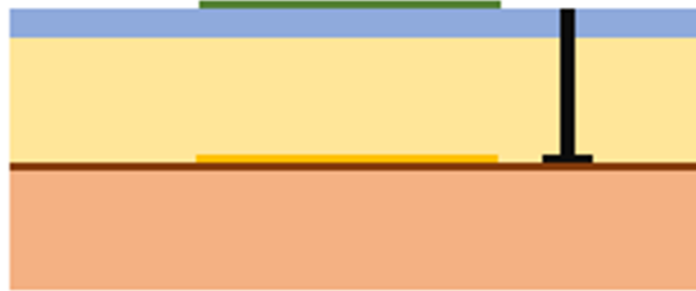

f)

Figure 5.1 Fabrication process flow of two-level microbolometer (cross-section view). (Continued)

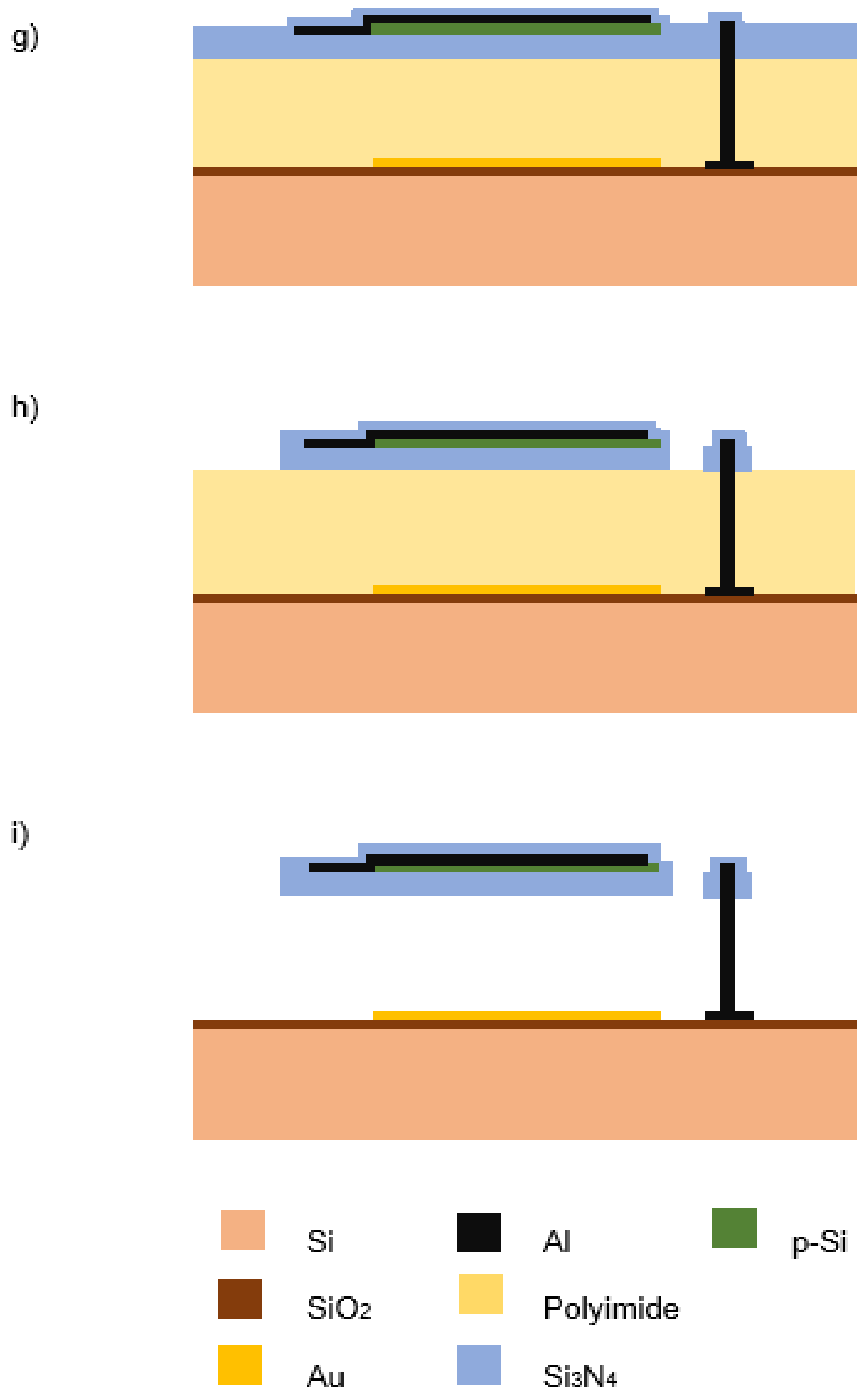

Figure 5.1 (Continued) Fabrication process flow of two-level microbolometer (cross-section view).

CHAPTER 6

CONCLUSIONS AND FUTURE WORK

6.1 Conclusions

In this study, p-Si as a thermosensing active element, in combination with a Si_3N_4 layer as IR absorber material, has been proposed for uncooled IR microbolometers. The maturity of the silicon processing technology makes p-type silicon a viable material to be considered as a thermosensing element with easy integration and compatibility with standard CMOS fabrication processes.

A simulated evolution of absorptance, transmittance and reflectance as function of thin film thickness, of various common dielectric materials has been presented in the above study. Results show that the optical properties of the dielectric materials considered exhibit thickness dependence throughout the spectral wavelength range (1.5-14.2 μm), and corroborates the high absorptance of Si_3N_4 in the spectral range of 8-14 μm. This study provides theoretical information of radiative properties of common dielectrics to be considered and to facilitate the design and fabrication of IR band-pass filters and lenses with applications in the infrared spectrum range of 1.5-14.2 μm.

This study provides information on the radiative properties of common dielectrics that can be considered to facilitate the design and fabrication of IR optical band-pass filters and lenses with applications in the infrared spectral range of 1.5-14.2 μm. The knowledge of the radiative properties of dielectric materials, in the range of NWIR (near-wave IR) to FWIR (far-wave IR), gives the ability to

choose an appropriate infrared absorber material for pyrometers, real time thermal imagers and other such instruments with capability to measure, map and control the manufacturing process temperature.

A two-level suspended, thermally isolated, microbolometer square-shaped multilayer structure (Si_3N_4/p-Si/Si_3N_4/Vacuum/Au/Si) is proposed in this research. Low doped p-silicon is presented as an alternative in order to reduce the standard high element (pixel) resistance, noise and fabrication costs. Its radiative properties are modeled and optimized in the wavelength spectral range of 8-14 μm (atmospheric transmission window) at room temperature, utilizing a matrix method (Multi-Rad simulation package) of representing the optical properties. The proposed two-level multilayer structure is optimized as a function of thin film multilayer and resonance cavity thickness, and exhibits a total infrared absorptance of more than 80% over the spectral range considered.

Results show that the combination of a resonant cavity with a reflective gold layer results in the enhancement of the IR radiation absorptance with a negligible IR radiation transmittance. Total values of radiative properties, as a function of the wavelength range and radiative properties for the specific wavelength range, have been simulated and calculated.

The performance of the proposed microbolometer is predicted with the numerical calculations of figures of merit as function of applied bias voltage, modulation frequency of the radiation source (blackbody) and focal number of the optical system. Two microbolometer structures are proposed and compared

obtaining significant improvements in the figures of merit for the modified microbolometer structure.

Even though the low doped p-Si thermosensing layer has low TCR, the normalized detectivity D^* achieved values of 10^8 are comparable with the state-of–the–art commercial devices.

The $NETD$ values lower than 50 mK at $f/_{\#}$=1 and the low thermal time constant τ_e of 4.176 ms show that the modified microbolometer structure is suitable for imaging systems with a video frame rate of 10-80 Hz.

The proposed microfabrication process is based on standard lithography microfabrication techniques. The monolithic fabrication approach is a cost-effective process due to the well-established post CMOS and can reduce the cost of the microbolometer fabrication.

The results obtained are critical in the design and fabrication of uncooled two-level microbolometer structures. In summary, the simulated results of the radiative properties and numerical calculations of figures of merit suggest the possibility to consider low doped p-type Si and the proposed two-level multilayer structure in the design and fabrication of uncooled infrared imaging arrays with a reasonable performance and low cost.

6.2 Future Work

This study shows that it is possible to implement low doped p-type Si as an alternative to the traditional thermosensing materials in the fabrication of uncooled infrared sensors and uncooled infrared imaging systems.

The high IR radiation absorptance (8-14 μm) and the results of numerical calculations of the performance of the proposed microbolometer two-level structure allows to continue with the process of fabrication and performance measurements of the proposed microbolometer, and to compare them with the performance of standard uncooled microbolometers that are commercially available. Efforts towards prototyping and technology transfer are in progress in collaboration with the ASRC (nanofabrication lab) at the City University of New York (CUNY).

REFERENCES

1. R. D. Hudson, Jr., Infrared System Engineering, John Wiley & Sons Inc., ISBN: 471-41850 (1969).
2. G. H. Rieke, Detection of Light, Cambridge University Press, 2nd edition, United Kingdom, ISBN 0-521-01710-6 (2003).
3. E. Hecht, Optics, Addison Wesley Longman, Inc., 3th edition, ISBN: 0-201-83887-7 (1998).
4. S. L. Gupta, S. Gupta, Unified Physics: Thermodynamics and Physics, Jai Prakash Nath & CO., 24th edition, Volume 2, (2002).
5. R. Siegel, J. Howell, Thermal Radiation Heat, Hemisphere Publishing Corporation, 2th edition, ISBN: 0-07-057316-6 (1972).
6. F. W. Sears, Mechanics, Wave Motion and Heat, Addison-Wesley Publishing Company, Inc., ISBN: 978-0201069051 (1950).
7. E. L. Dereniak, G. D. Boreman, Infrared Detectors and Systems, John Wiley & Sons, Inc., ISBN 0-471-12209-2 (1996).
8. C. Lamsal, N. R. Ravindra, (2014). Simulation of Spectral Emissivity of Vanadium Oxides (VO_x)-Based Microbolometer Structures, *Emerging Materials Research*, 3, 194-202.
9. P. W. Kruse, The Photon Detection Process in Optical and Infrared Detectors, Springer-Verlang, New York Heidelberg Berlin, 2th edition, ISBN: 0-387-10176-4 (1980).
10. A. Rogalski, (2002). Infrared Detectors: An Overview, *Infrared Physics & Technology*, 43, 187–210.
11. A. Rogalski, Infrared Photon Detectors, SPIE The International Society of Optical Engineering, SPIE Optical Engineering Press, ISBN: 978-1420076714 (1995).
12. R. B. Darling, S. Inawaga, (2009). Structure, Properties, and MEMS and Microelectronic Applications of Vanadium Oxides, *Sadhana*, 34, 531-542.
13. G. Hyseni, et al., (2010). Infrared Thermal Detectors Parameters: Semiconductor Bolometers Versus Pyroelectrics, *WSEAS Transactions on Circuits and Systems*, 9, 238-241.

14. R. K. Bhan, et al., (2009). Uncooled Infrared Microbolometer Arrays and their Characterization Techniques, *Defense Science Journal*, 59, 580-589.

15. A. Kosarev, et al., (2014). Thin Film Uncooled Microbolometers Based on Plasma Deposited Materials, *Canadian Journal of Physics*, 92, 570–575.

16. J. W. Nilsson, Electric Circuits, Addison-Wesley Publishing Company, ISBN:0-201-06238-0 (1983).

17. A. Rogalski, Infrared Detectors, CRC Press, 2th edition, ISBN 978-1-4200-7671-4 (2011).

18. J. C. Doll, B. L. Pruitt, Piezoresistor Design and Applications, Springer, ISBN: 978-1-4614-8516-2 (2013).

19. W. Kruse, et al., Elements of Infrared Technology: Generation, Transmission and Detection, Wiley, New York, ISBN: 0471508861 (1962).

20. L. K. J. Vandamme, G. Trefan, (2002). 1/f Noise in Homogeneous and Inhomogeneus Media. *IEE Proceedings- Circuits Devices and Systems*, 149, 3-12.

21. F. N. Hooge, (1994). 1/f Noise Sources, *IEEE Transactions on Electron Devices*, 41, 1926-1935.

22. F. N. Hooge, (1972). Discussion of Recent Experiments on 1/f Noise. *Physica*, 60, 130-144.

23. J. Baars, M. Schulz, (1995). Performance Characteristics, Measurements Procedures, and Figures of Merit for Infrared Planes Arrays, *Proceedings of SPIE*, 2470, 141-155.

24. D. J. Griffiths, Introduction to Electrodynamics, Prentice Hall, 3th edition, ISBN: 0-13-805326-X (1999).

25. J. D. Jackson, Classical Electrodynamics, John Wiley & Sons, Inc., 2nd edition, ISBN: 0-471-43132-X (1975).

26. R. E. Hummel, Electronic Properties of Materials, Springer-Verlag, 2nd edition, ISBN: 3-540-54839-4 (1992).

27. J. P. Hebb, K. F. Jenson, (1997). User's Manual Multi-Rad Version 1.0, Massachusetts Institute of Technology Cambridge MA.

28. M. Born, E. Wolf, Principles of Optics, The McMillan Company, 2th edition, (1964).

29. P. Yeh, Optical Waves in Layered Media, Wiley, New York, ISBN: 978-0471731924 (1988).

30. J. R. Howell, et al., Thermal Radiation Heat Transfer, CRC Press, 5th edition, ISBN: 978-1439805336 (2011).

31. J. P. Hebb, K. F. Jensen, (1996). The Effect of Multilayer Patterns on Temperature Uniformity During Rapid Thermal Processing, *Journal of Electrochemical Society.* 143, 1142-1151.

32. N. M. Ravindra, et al., (2003). Modeling and Simulation of Emissivity of Silicon-Related Materials and Structures. *Journal of Electronic Materials*, 32, 1052-1058.

33. A. H. Pfund, (1933). The Optical Properties of Metallic and Crystalline Powders, *Journal of Optical Society of America*, 23, 375–378.

34. L. Harris, et al., (1938). The Preparation and Optical Properties of Gold Blacks, *Journal of Optical Society of America*, 38, 582–589.

35. W. Lang, et al., (1992). Absorbing Layers for Thermal Infrared Detectors, *Sensors and Actuators A: Physical*, 34, 243-248.

36. F. J. J. Clarke, J. A. Larkin, (1985). Measurement of Total Reflectance, Transmittance and Emissivity Over the Thermal IR Spectrum, *Infrared Physics*, 25, 359-367.

37. F. J. J. Clarke, J. A. Larkin, (1986). Low Reflectance Coatings: Platinum Black for Infrared Technology, *Platinum Metals Revision.*, 30, 21-22.

38. J. Goldsmith, et al., (2014). Black Aluminum: a Novel Anti-Reflective Absorbing Coating, *NAECON - IEEE National Aerospace and Electronics Conference*, 69 – 70.

39. A. Y. Vorobyev, C. Guo, (2008). Colorizing Metals with Femtosecond Laser Pulses, *Applied Physics Letters*, 92, 1-3.

40. A. Y. Vorobyev, C. Guo, (2009). Femtosecond Laser Blackening of Metals, *52nd IEEE International Midwest Symposium on Circuits and Systems*, 905-908.

41. P. G. Maloney, et al., (2010). Emissivity of Microstructure Silicon, *Applied Optics*, 49, 1065-1068.

42. S. R. Marthi, et al., (2015). Optical Properties of Black Silicon: An Analysis, *JOM: Journal of the Minerals, Metals & Minerals Society*, 67, 2154-2159.

43. T. P. Pasanin, et al., (2018). Impact of Standard Cleaning on Electrical and Optical Properties of Phosphorous-Doped Black Silicon, *IEEE Journal of Photovoltaics,* 8, 697-702.

44. N. M. Ravindra, et al., (2015). Modeling of Optical Properties of Black Silicon/Crystalline Silicon, *Journal of Scientific and Industrial Metrology*, 1,1-7.

45. X. Liu, et al., (2014). Black silicon: Fabrication Methods, Properties and Solar Energy Applications, *Energy & Environmental Science*, 10, 1-95.

46. R. R. Neli, et al., (2006). Development of Process for Far Infrared Sensor Fabrication, *Sensors and Actuators A*, 132, 400–406.

47. R. R. Neli, et al., (2014). Characterization of Fast-Response and Low Noise Poly Si Uncooled Far Infrared Sensor, *2014 IEEE 5th Latin American Symposium on Circuits and Systems*, 1-4.

48. C. N. Chen, W. C. Huang, (2011). A CMOS-MEMS Thermopile with Low Thermal Conductance and a Near-Perfect Emissivity in the 8–14-μm Wavelength Range, *IEEE Electron Device Letters*, 32, 96-98.

49. N. Nelms, J. Dowson, (2005). Goldblack Coating for Thermal Infrared Detectors, *Sensors and Actuators A*, 120, 403–407.

50. S. Ilias, et al., (2010). Deposition and Characterization of Gold Black Coatings for Thermal Infrared Detectors, *Proceedings of SPIE*, 7750, 77501J-10.

51. Y. Fang, et al., (2012). Preparation and Characterization of Ultra-Low Density Porous Gold Foams, *Materials Letters*, 67, 46–48.

52. F. Forsberg, et al., (2013). Very Large Scale Heterogeneous Integration (VLSHI) and Wafer-Level Vacuum Packaging for Infrared Bolometer Focal Plane Arrays, *Infrared Physics & Technology*, 60, 251-259.

53. B. E. Cole, et al., (1998). Monolithic Two-Dimensional Arrays of Micromachined Microstructures for Infrared Applications, *Proceedings of the IEEE*, 86, 1679-1686.

54. A. Rogalski, (2009). Infrared Detectors for the Future, *Acta Physica Polonica A*, 116, 389-406.

55. A. Rogalski, (2011). Recent Progress in Infrared Detector Technologies, *Infrared Physics & Technology*, 54, 136–154.

56. M.-S. Han, et al., (2015). Vanadium Oxide Microbolometer Using ZnO Sandwich Layer, *Applied Science and Convergence Technology,* 24, 178-183.

57. P. W. Kruse, D. D. Skatrud, Uncooled Infrared Imaging Arrays and Systems, Semiconductors and Semimetals, Academic Press, ISBN: 978-0127521558 (1997).

58. C. Chen, et al., (2001). Micromachined Uncooled IR Bolometer Linear Array Using VO_2 Thin Films, *International Journal of Infrared and Millimeter Waves*, 22, 53-58.

59. C. Chang-Hong, et al., (2001). Infrared Responsivity of Uncooled VO_2-Based Thin Films Bolometer, *Acta physica Polonica*, 50, 450-452.

60. C. Posch, et al., (2009). A Microbolometer Asynchronous Dynamic Vision Sensor for LWIR, *IEEE Sensors Journals*, 9, 654-664.

61. P. Wang, et al., (2015). High Sensitivity 17 µm Pixel Pitch 640 × 512 Uncooled Infrared Focal Plane Arrays Based on Amorphous Vanadium Oxide Thin Films, *IEEE Electron Device Letters*, 36, 923-925.

62. S. Chen, et al., (2009). Characterization of Nanostructured VO_2 Thin Films Grown by Magnetron Controlled Sputtering Deposition and Post Annealing Method, *Optical Express*,17, 24153-24161.

63. S. Moon, (2004). Novel Infrared Absorbing Material Coupled Uncooled Microbolometer, *Proceedings of IEEE*, 2, 658-660.

64. N. H. Azhan, K. Okimura, (2017). Role of Strain and Oxygen Vacancies in Modifying the Transition Temperature of VO_2 Films Deposited via Rf Biased Sputtering, *International Conference on Engineering Technology and Technopreneurship (ICE2T)*, 1-5.

65. S. Chen, et al., (2007). Fabrication and Performance of Microbolometer Arrays Based on Nanostructured Vanadium Oxide Thin Films, *Smart Materials and Structures*, 16, 696-700.

66. F. Guinnetona, et al., (2001). Comparative Study Between Nanocrystalline Powder and Thin Film of Vanadium Dioxide VO_2: Electrical and Infrared Properties, *Journal of Physics and Chemistry of Solids*, 62, 1229-1238.

67. R. T. R. Kumar, et al., (2003). Study of a Pulsed Laser Deposited Vanadium Oxide Based Microbolometer Array, *Smart Materials and Structures*, 12, 188-192.

68. G. Li, et al., (2008). Low Temperature Deposited Nano-Structured Vanadium Oxide Thin Films for Uncooled Infrared Detectors, *2nd IEEE International Nanoelectronics Conference (INEC)*, 921-923.

69. S. V. Grayli, et al., (2015). Room Temperature Deposition of Highly Sensitive Vanadium Oxide Films for Infrared Light Sensing Applications, *IEEE Sensors*, 1-4.

70. M. Almasri, et al., (2006). Amorphous Silicon Two-Color Microbolometer for Uncooled IR Detection, *IEEE Sensors Journal*, 6, 239-300.

71. X. Liu, et al., (2006). A Novel Uncooled a-Si Microbolometer for Infrared Detection, *8th International Conference on Solid-State and Integrated Circuit Technology Proceedings*, 626 – 628.

72. F. Simoens, et al., (2011). Active Imaging with THz Fully-Customized Uncooled Amorphous-Silicon Microbolometer Focal Plane Arrays, *International Conference on Infrared, Millimeter, and Terahertz Waves*, 1–2.

73. A. Heredia, et al., (2003). Low Temperature Electrical Properties of a Boron-Doped Amorphous Silicon Bolometer, *Proceedings of the Electrochemical Society*, Abs.881.

74. J.-H. Su, et al., (2016). Temperature Coefficient of Resistance Related to Amorphous Silicon/Metal Contact Design of Microbolometers, *3rd International Conference on Devices, Circuits and Systems,* 63 – 67.

75. V. Y. Zerov, et al., (2004). Calculational Modeling of the Main Characteristics of an Uncooled Linear Microbolometer Array, *Journal of Optical Technology*, 7, 153-157.

76. M. Boninsegni, et al., (1989). Low-Temperature Bolometer Array, *Review of Scientific Instruments*, 60, 661-665.

77. S. Eminoglu, et al., (2003). Low- Cost Uncooled Infrared Detectors in CMOS Process, *Sensors and Actuators*, A 109, 102–113.

78. D. S. Tezcan, et al., (2003). A Low-Cost Uncooled Infrared Microbolometer Detector in Standard CMOS Technology*, IEEE Transactions on Electron Devices,* 50, 494-502.

79. D. S. Tezcan, et al., (1999). An Uncooled Microbolometer Infrared Detector in Any Standard CMOS technology, *The 10th international Conference on solid-State sensors & actuators* (Transducer'99), 610-613.

80. S. V. Grayli, et al., (2015). Room Temperature Deposition of Highly Sensitive Vanadium Oxide Films for Infrared Light sensing applications, *Sensors*, 1-5.

81. M. Kohin, N. Buttler, (2004). Performance Limits of Uncooled VOx Microbolometer Focal Plane Arrays, *Proceedings of SPIE*, 5406, 447-453.

82. P. W. Kruse, (2004). Can the 300 K Radiating Background Noise Limit be Attained by Uncooled Thermal Imagers? *Proceedings of SPIE*, 5406, 437-446.

83. F. Niklaus, et al., (2007). Uncooled Infrared Bolometer Arrays Operating in a Low to Medium Vacuum Atmosphere: Performance Model and Tradeoffs, *Proceedings of SPIE*, 6542, 1M.1-1M.12.

84. F. Niklaus, et al., (2007). Performance Model for Uncooled Infrared Bolometer Arrays and Performance Predictions of Bolometers Operating at Atmospheric Pressure, *Infrared Physics and Technolog*y, 51, 168-177.

85. N. W. Aschroft, N. D. Mermin, Solid State Physics. Saunders College Publishing, ISBN: 0-03-083993-9 (1976).

86. W. F. Smith, Foundations of Materials Science and Engineering. WCB/McGraw-Hill, 2th edition, ISBN: 0-07-059202-0 (1993).

87. B. S. Mitchell, An introduction to Materials Engineering and Science for Chemical and Materials Engineer, John Wiley & Sons, ISBN: 0-471-43623-2 (2004).

88. W. M. Bullis, et al., (1968). Temperature Coefficient of Resistivity of Silicon and Germanium Near Room Temperature, *Solid State Electronics*,11, 639-646.

89. P. Norton, J. Brandt, (1978). Temperature Coefficient of Resistance for p- and n-Type Silicon, *Solid-State Electronic*, 21, 969-974.

90. N. Maluf, An Introduction to Microelectromechanical Systems Engineering, Artech House, Inc., ISBN: 978-1580535908 (2004).

91. K. Jhansirani, et al., (2016). Deposition of Silicon Nitride Films Using Chemical Vapor Deposition for Photovoltaic Applications, *Results in Physics*, 6, 1059–1063.

92. S. Franssila, Introduction to Microfabrication, John Wiley & Sons, Ltd., ISBN: 9780470749838 (2010).

93. P. J. Van Zwol, et al., (2015). Emissivity of Freestanding Membranes with Thin Metal Coatings, *Journal of Applied Physics*, 118, 1-5.

94. J. Kischkat, et al., (2012). Mid-infrared Optical Properties of Thin Films of Aluminum Oxide, Titanium Dioxide, Silicon Dioxide, Aluminum Nitride, and Silicon Nitride, *Applied Optics*, 51, 6789-6798L.

95. S. F. Jutzi, et al., (2009). Far-Infrared Sensor with LPCVD-Deposited Low-Stress Si-Rich Nitride Absorber Membrane -Part 1. Optical Absorptivity, *Sensors and Actuators A: Physical*, 152, 119–125.

96. D. K. Schroder, D. L. Meier, (1984). Solar Cell Contact Resistance-A Review, *IEEE Transactions on Electron Devices*, 31, 637-647.

97. J. Tao, et al., (1993). Electromigration Reliability of Tungsten and Aluminum Vias and Improvements Under AC Current Stress*, IEEE Transactions on Electron Devices*, 40, 1398-1405.

98. Refractive index Database, https://refractiveindex.info/?shelf=main&book=Si&page=Chandler Horowitz, accessed on 12th February 2017.

99. Refractive Index Database, https://refractiveindex.info/?shelf=main&book=Si3N4&page=Kischkat, accessed on 12th February 2017.

100. Refractive Index Database, https://refractiveindex.info/?shelf=main&book=Al&page=Rakic,accessed on 12th February 2017.

101. Refractive Index Database, https://refractiveindex.info/?shelf=main&book=Au&page=Olmon-sc, accessed on 12th February 2017.

102. M. Alhussein, S. I. Haider, (2016). Simulation and Analysis of Uncooled Microbolometer for Serial Readout Architecture, Hindawi Publishing Corporation, *Journal of Sensors*, Volume 2016, 1-13.

103. S. Gupta, et al., (2013). Design Optimization of Pixel Structure for α-Si Based Uncooled Infrared Detector, *Defence Science Journal*, 63, 581-588.

104. D. Murphy, et al., (2004). Performance Improvements for VOx Microbolometer FPAs, *Proceedings of SPIE*, 5406, 531-540.

105. M. Moreno, et al., (2015). Microbolometers Based on Amorphous Silicon–Germanium Films with Embedded Nanocrystals, *IEEE Transactions on Electron Devices*, 62, 2120-2127.

106. F. Sizov, (2012). IR Region Challenges: Photon or Thermal Detectors? Outlook and Means, *Semiconductor Physics, Quantum Electronics & Optoelectronics*, 15,183-199.

107. F. Niklaus, (2007). MEMS-Based Uncooled Infrared Bolometer Arrays – A Review, *Proceedings of SPIE*, 6836, 68360D-(1-15).

108. Q. Cheng, et al., (2011). Design of Dual-Band Uncooled Infrared Microbolometer, *IEEE Sensors Journal*, 11, 167-175.

109. A. D. Rakić. (1995). Algorithm for the Determination of Intrinsic Optical Constants of Metal Films: Application to Aluminum, *Applied Optics*, 34, 4755-4767.

110. R. L. Olmon, et al., (2012). Optical Dielectric Function of Gold, *Physics Review B*, 86.

111. N. Shen, et al., (2015). An Uncooled Infrared Microbolometer Array for Low-Cost Applications, *IEEE Photonics Technology Letters*, 27, 1247-1249.

112. G. T. A. Kovacs, Micromachined Transducer Sourcebook, McGraw-Hill, ISBN:0-07-290722-3 (1998).

113. E. Mottin, et al., (2003). Uncooled Amorphous Silicon Technology Enhancement for 25 µm Pixel Pitch Achievement, *Proceedings of SPIE*, 4820, 200-207.

114. B. Backer, et al., (2003). Advances in Uncooled Technology at BAE Systems, *Proceedings of SPIE*, 5074, 548-556.

115. M. Joodaki, et al., (2002). New Generation Quasi-Monolithic Integration Technology (QMIT), *Electronic Components and Technology Conference*, 641-645.

116. J. J. Yon, et al., (2003). Infrared Microbolometer Sensors and their Application in Automotive Safety, *Proceedings of AMAA*, 1-15.

117. P. Eriksson, et al., (1997). Thermal Characterization of Surface-Micromachined Silicon Nitride Membranes for Thermal Infrared Detectors, *Journal of Microelectromechanical Systems*, 6, 55-61.